Measurement of $Z/\gamma^* + b-$jet Production Cross section in $p\bar{p}$ collisions at $\sqrt{s} = 1.96$ TeV with the CDF detector

Lorenzo Ortolan
Institut de Física d'Altes Energies
Universitat Autònoma de Barcelona
Departament de Física
Edifici Cn, Campus UAB
E-08193 Bellaterra (Barcelona)

July 2012

supervised by
Dr. Verónica Sorin
(IFAE)

Tutor:
Prof. Mario Martínez Pérez
(ICREA/IFAE and UAB)

Contents

1 Introduction

Processes at hadron colliders, such as the production of jets, are described by the Quantum Chromodynamics theory (QCD). Precise descriptions of processes involving jets in association with a vector boson have nowadays large relevance as they represent irreducible background to other Standard Model (SM) processes and searches for new physics.
The experimental study and understanding of the $b-$jet production in association with a Z boson are crucial for many reasons. For one side, it is the most important background for a light Higgs boson[1] decaying into a bottom-antibottom quark pair and produced in the ZH mode. This is one of the most promising channels for the Higgs search at Tevatron in particular since the latest results [2] have excluded the high mass region ($M_H \geq$127 GeV/c^2). For another side the signature of $b-$jets and a Z boson is also background to new physics searches, such as supersymmetry, where a large coupling of the Higgs boson to bottom quarks is allowed [3].

The production cross section measurement of $b-$jets in events with a Z boson has already been performed at hadron colliders, at the Tevatron by CDF [4] and D0 experiments [5] and is now pursued at the LHC by ATLAS [6] and CMS [7]. In particular the CDF measurement was performed with only 2 fb^{-1} and was limited by the statistical uncertainty.
This PhD thesis presents a new measurement of the $Z/\gamma^* + b-$jet production cross section using the complete dataset collected by CDF during the Run II.
Z/γ^* bosons are selected in the electron and muon decay modes and are required to have $66 \leq M_Z \leq 116$ GeV/c^2 while jets, reconstructed with the MidPoint algorithm, have to be central ($|Y| \leq 1.5$) with $p_T \geq 20$ GeV/c . The per jet cross section is measured with respect to the Z/γ^* inclusive and the Z/γ^*+jets cross sections. Results are compared to leading order (LO) event generator plus parton shower and next-to-leading order (NLO) predictions corrected for non perturbative effects such as hadronization and underlying event. Differential distributions as a function of jet transverse moment and jet rapidity are also presented together with the comparison to NLO pQCD predictions for different renormalization and factorization scales and various PDF sets.

Chapter 2 and Chapter 3 are dedicated to explain the main features of the theory of Quantum Chromodynamics, to provide a description of the predictive Monte Carlo tools used in experimental context to simulate signal and background and to review the challenges of the calculation of the $Z + b-$jet production processes. The Tevatron collider and the CDF experiment are described in Chapter 4. The procedure followed at CDF for the reconstruction of physics objects is treated with particular attention to the $b-$jets identification technique in Chapter 5. The analysis strategy for the integrated cross section is well discussed in Chapter 6, while the methodology for the differential cross section measurements as a function of jet transverse momentum and jet rapidity are presented in Chapter 7. Finally, results are reported in Chapter 8 including the comparison to different theoretical predictions. Chapter

9 is devoted to the summary and the conclusions.

2 QCD Theory

In this chapter, a general description of the fundamentals of the QCD theory is given together with a description of Monte Carlo tools, extensively used at hadron colliders. An important QCD signature is the production of collimated jets of hadrons and since the aim of this thesis is a jet production cross section also the theoretical and experimental issues concerning the definition of a jet are discussed largely.

2.1 The QCD Lagrangian

Quantum ChromoDynamics (QCD) [8] is the Standard Model (SM) theory that governs the strong interaction, which is one of the four fundamental forces in Nature. The strong interaction is responsible for binding together quarks and gluons to form hadrons, among which the proton and the neutron are the most well-known examples.
QCD is a non abelian gauge theory based on the SU(3) symmetry group. Hadrons are made of quarks, which carry color charge and comes in three varieties. Gluons are the bosons that mediate the strong interaction. They carry a color and anti-color charge, being 8 the possible different combinations. Since gluons carry color charge themselves, they couple to each other. Two important features of QCD are asymptotic freedom and confinement. Asymptotic freedom means that strong interactions become large at low energy and smaller at high energy. Color confinement implies that gluons and quarks cannot be observed as free particles at large distances and they are confined in bound states (hadrons).
In quantum field theory QCD is expressed by the Lagrangian density:

$$L = \bar{\psi}_q^i (i\gamma^\mu)(D_\mu)_{ij}\psi_q^j - m_q \bar{\psi}_q^i \psi_q^j - \frac{1}{4} F_{\mu\nu}^a F^{a\mu\nu} \tag{2.1}$$

where ψ_q^i represents a quark field with color index i, γ^μ is a Dirac matrix with μ being a Lorentz vector index, m_q the mass of the quark, $F_{\mu\nu}^a$ is the gluon field strength tensor for a gluon with color index a (in the adjoint representation, $a \in [1, ..., 8]$).
D_μ is the covariant derivative in QCD

$$(D_\mu)_{ij} = \delta_{ij}\partial_\mu - i g_s t_{ij}^a A_\mu^a \tag{2.2}$$

with g_s the strong coupling ($g_s^2 = 4\pi\alpha_s$), A_μ^a is the gluon field with color index a and t_{ij}^a are the generators of the $SU(3)$ group[1].
It is worth noting that the gluon field acts on quark color, taking away one color and replacing it with another, as it is shown in color flow diagram in Figure 2.1.

Moreover $F_{\mu\nu}^a$ is defined as:

[1]They are proportional to the hermitian and traceless Gell-Mann matrices ($t_{ij}^a = \frac{1}{2}\lambda_{ij}^a$)

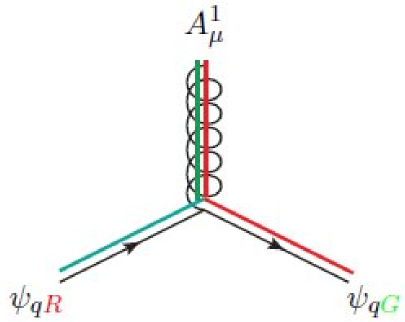

Figure 2.1: Color flow of a qqg vertex in QCD.

$$F^a_{\mu\nu} = [\partial_\mu A^a_\nu - \partial_\nu A^a_\mu - g f^{abc} A^b_\mu A^c_\nu] \tag{2.3}$$

where the third term, due to $SU(3)$ being non-abelian, is responsible for the self interaction of gluons.

2.1.1 Lattice QCD and perturbative approximation

There are two main approaches used to solve QCD: lattice QCD [9] and perturbative QCD [10].
Lattice QCD is formulated on a grid of points in discrete space time, introducing a cut-off at the order of $1/a$, where a is the lattice spacing, which regularizes the theory. As a result lattice QCD is mathematically well-defined. Fields representing quarks are defined at lattice sites while gluons fields are defined on the link connecting close sites. The observables are determined using numerical simulation done with Monte Carlo algorithms.
This had a great success for example in predicting the hadron mass spectrum but it presents an inconvenience: the huge computational time needed to extract the solution, in particular on complex high particle multiplicity events such as those produced at high energy hadron colliders.
Perturbative QCD (pQCD) is a widely used method valid for high energy scales where the strong coupling constant is small. It is based on an order by order expansion in the coupling constant α_s. For example in this regime a cross section of a given physics process is expressed by

$$\sigma = \sigma_0 + \sigma_1 \alpha_s + \sigma_2 \alpha_s^2 + .. \tag{2.4}$$

where the σ_i are the cross sections at different perturbative orders. They are evaluated with the help of Feynman diagrams (Figure 2.2) where each QCD vertex contributes as α_s. One might calculate the first terms only since the others should be small.

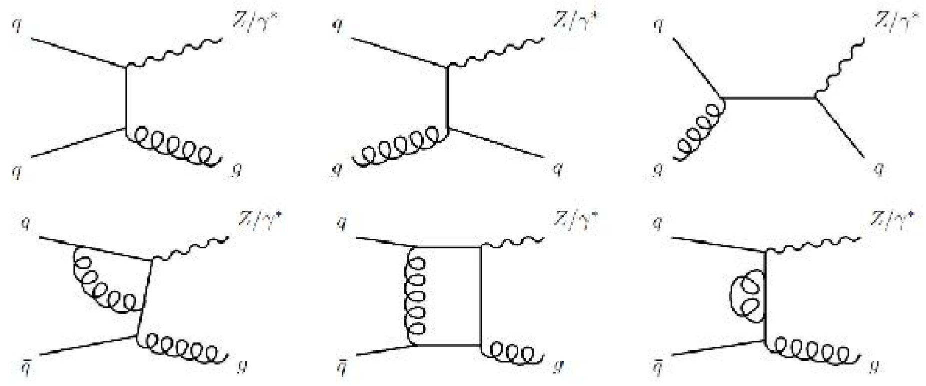

Figure 2.2: Feynman diagrams for Z+jet process.

2.1.2 Renormalization and running coupling constant

Let us consider a perturbative expansion of the physical observable, σ, at one determined energy scale Q. Leading order usually consists of tree (LO) diagrams, but higher order contributions involved loop diagrams and calculations have to handle the ultraviolet divergences that appear as consequence. To handle this divergence a dimensional regularization procedure is done. This introduces an arbitrary renormalization scale μ that represents the point at which the subtractions are performed to remove the ultraviolet divergence. Since μ is an arbitrary parameter the physical observable should not depend on its value. The dependence on μ is absorbed in the renormalized coupling constant $\alpha_s(\mu)$. This may be expressed by:

$$\frac{\partial\alpha_s(Q^2)}{\partial t} = \beta(\alpha_s(Q^2)), \qquad \frac{\partial\alpha_s(Q^2)}{\partial\alpha_s} = \frac{\beta(\alpha_s(Q^2))}{\beta(\alpha_s)}$$

with $t = \ln\frac{Q^2}{\mu^2}$ and $\beta(\alpha_s) = \mu^2\frac{\partial\alpha_s}{\partial\mu^2}$. The new function, $\alpha_s(Q^2)$, is called running coupling. Using the renormalization group equation, α_s may be expressed by the following formula:

$$t\frac{\partial\alpha_s}{\partial t} = \beta(\alpha_s(Q^2)) \qquad \beta(\alpha_s) = -b\alpha_s^2(1 + b_1\alpha_s + ...)$$

where

$$b = \frac{11C_A - 2n_f}{12\pi} \quad b_1 = \frac{153 - 19n_f}{24\pi^2}$$

n_f is the number of active light flavors and C_A is the color factor $C_A = 3$.
β is the derivative of α_s with respect to the energy scale, thus when β is negative, α becomes small for large energy scales. This is the meaning of asymptotic freedom [11], the fact that the coupling becomes weaker at high momentum scales. In this region quarks and gluons are treated as free particles which do not interact, and the perturbative expansion of QCD is valid. On the other side, when the scale is small the interaction becomes strong, this leads to confinement of quarks and gluons, they are constrained to form colorless clusters called hadrons.
If $\alpha_s(Q^2)$ and $\alpha_s(\mu^2)$ are in the perturbative region the higher terms of the perturbative

expansion can be neglected; thus a simple solution for $\alpha_s(Q^2)$ is:

$$\alpha_s(Q^2) = \frac{\alpha_s(\mu^2)}{1 + b\alpha_s(\mu^2)\log\frac{Q^2}{\mu^2}} = \frac{1}{b\log\frac{Q^2}{\Lambda^2}} \tag{2.5}$$

Perturbative theory expresses how the coupling constant varies as a function of the energy scale, but experimental measurements are needed to determine it.
The parameter Λ was historically introduced as a reference scale. It is a dimensional parameter defined as:

$$\log\frac{Q^2}{\Lambda^2} = -\int_{\alpha_s(Q^2)}^{\infty}\frac{\partial x}{\partial\beta(x)} \tag{2.6}$$

and it represents the scale at which the coupling would diverge and also the order of magnitude of the energy where the perturbative theory is valid, the actual value of Λ is ~ 200 MeV. Its precise value depends on the perturbative order at which it is evaluated and on the number of active flavors. For energy scales $Q \gg \Lambda$ the perturbative approximation is valid since there is $\alpha_s \ll 1$, while for energies $\sim \Lambda$ the interaction between quarks becomes very strong and the perturbative QCD is not longer applicable.
In the last years a lot of experimental measurements were performed for several processes and in different energy regions to determine the α_s. The actual results, in Figure 2.3, were obtained with important theoretical and experimental improvements, and show a really nice agreement between predictions and experimental measurements. They lead to a world average estimation at the reference scale of Z^0 boson mass of $\alpha_s(M_{Z^0}) = 0.1184 \pm 0.0007$.

2.2 A typical hadron collision and the factorization theorem

Final states of hadron collisions, such as those produced by proton-anti-proton pairs colliding at large center-of-mass energies, are characterized by a large multiplicity of hadrons associated with the evolution of the partons that have interacted. The fundamental concept that allows to obtain predictions of these physical phenomena is the factorization [13]. This means that calculations may be performed separating independent stages of the overall process, each one with its particular dynamics and solution techniques. In particular, the complex structure of the proton and the final state hadron formation can be decoupled from the elementary structure of the interaction of the partons. While the hard scattering could be described with perturbative methods, the initial and final states are evaluated using phenomenological models extracted from experimental data. The delimitation of these two phases is determined by a factorization scale, μ_f, thought as the scale that separates long and short distance physics. The main phases of a hadron collision are illustrated in Figure 2.4.

According to the factorization theorem the differential cross section as a function of a generic hadronic observable X is expressed by:

$$\frac{d\sigma}{dX} = \sum_{j,k}\int d\hat{X} f_j(x_1, Q) f_k(x_2, Q)\frac{d\hat{\sigma}_{j,k}}{d\hat{X}} F(\hat{X} \to X; Q) \tag{2.7}$$

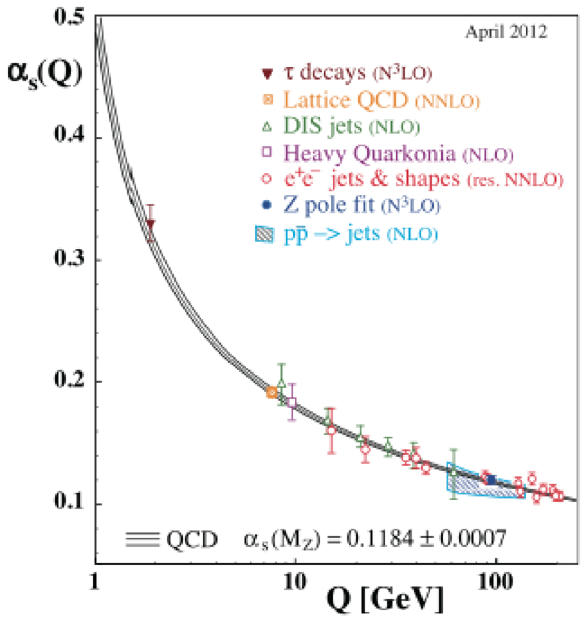

Figure 2.3: The QCD coupling measured at different scales Q and different experiments. The band is obtained by running the world average within its uncertainty. From [12].

where the sum is over the j, k parton types inside the proton, the function $f_j(x, Q)$ (PDF) parameterizes the number density of parton type j with the momentum fraction x in a proton at a scale Q; $\hat{X}$ is the parton level kinematic variable; $\hat{\sigma}_{j,k}$ is the parton cross section and $F(\hat{X} \to X; Q)$ is the transition function that parameterizes the hadronization.

2.2.1 The Initial State: PDFs and their evolution

Over the last years the knowledge of PDFs and the proton structure has been developed with the help of deep inelastic scattering experiments (DIS) [14]. The DIS, represented schematically in Figure 2.5, is a lepton-proton scattering in which the photon exchanged between lepton and the photon has a large virtuality Q.

The idea is that by measuring all the kinematical variables of the outgoing lepton one can study the structure of the proton in terms of the probe characteristics. First results from DIS experiments led to the Quark Parton Model to describe the structure of the proton. This is characterized by a proton formed by point-like partons that carry a fraction of the proton momentum. In this naive model the PDFs do not depend on the scale where they are evaluated. Therefore, they only depend on the momentum fraction carried. This is known as Bjorken scaling [15].
This naive parton model had a great success though it was not able to account for some

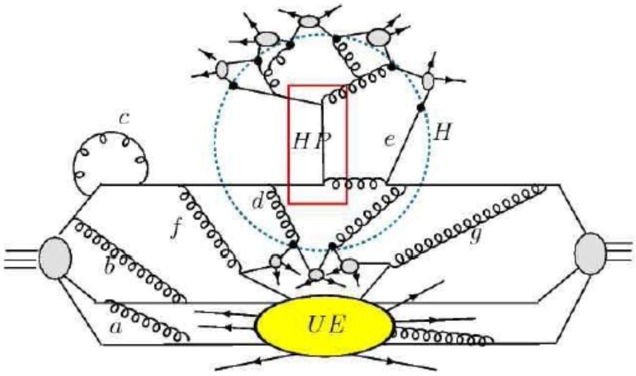

Figure 2.4: The three main phases of a hadron collision: at the beginning the proton (anti-proton) is made of quarks with a continuous exchange of gluons at high virtuality (well-described by PDF) and in the collision one from each proton interacts in a hard-scattering process (HP) forming other partons at high momentum transfer. These start to radiate gluons until they reach low energy scale, where the strong interaction becomes very strong and constrains the quarks to form colorless clusters, (hadrons). Nearby partons merge into colorless clusters that then decay phenomelogically into physical hadrons. Partons that are not involved in the hard scatter could interact later and are called Underlying event (UE).

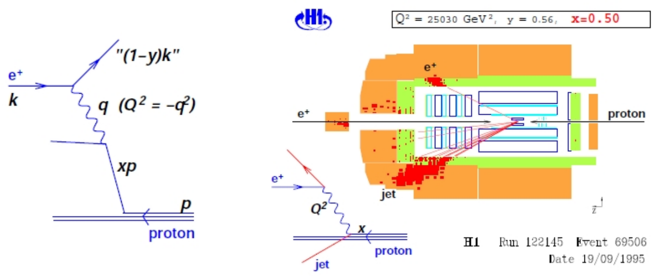

Figure 2.5: Deep Inelastic Scattering scheme and HERA experimental layout. Figure taken from [12].

experimental results. In QCD, the radiation of gluons from quarks means a violation of the scaling. In fact, as the probing scale is increased, the observed parton is resolved into several, softly interacting particles (Figure 2.6): the increase in number of constituent partons turns in a decrease of the momentum carried by each of them. This implies an increase in the parton densities at low momentum fraction values, and a decrease of the densities at high momentum fractions. Such scale dependence, was experimentally observed, where approximately half of the proton momentum was not carried by the charged particles that participated in the electroweak process (Figure 2.7), indicating a success of QCD.

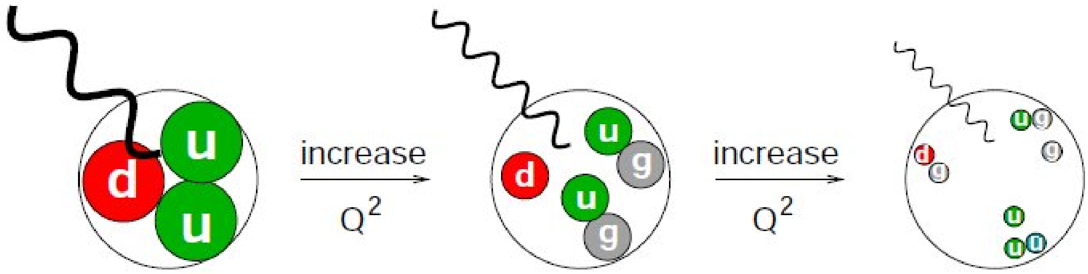

Figure 2.6: With ever shorter wavelength photon probes one resolves more and more structure inside the proton.

Even though perturbative QCD does not predict the form of the PDFs it can describe their evolution with the variation of the scale. This is done through the DGLAP, Dokshitzer-Gribov-Lipatov-Altarelli-Parisi, equations [16].

The equations are given for the quark field by

$$t\frac{dq(x,t)}{dt} = \frac{\alpha_s(t)}{2\pi}\int_x^1 \frac{dy}{y}\left[q(y,t)P_{qq}(\frac{x}{y},\alpha_s(t)) + g(y,t)P_{qg}(\frac{x}{y},\alpha_s(t))\right] \tag{2.8}$$

and for the gluon:

$$t\frac{dg(x,t)}{dt} = \frac{\alpha_s(t)}{2\pi}\int_x^1 \frac{dy}{y}[g(y,t)P_{gg}(\frac{x}{y},\alpha_s(t)) + \sum_{q,\bar{q}} q(y,t)P_{gq}(\frac{x}{y},\alpha_s(t))]$$

where $t = \log Q^2$ and P_{qq}, P_{qg}, P_{gq} the splitting functions for gluon radiations ($q \to qg$), gluon splittings ($g \to gg$) and quark pair productions ($g \to q\bar{q}$). They can be calculated at leading order:

$$P_{qq} = \frac{4}{3}\frac{1+x^2}{1-x}$$

$$P_{gg} = 2C_A[\frac{1-x}{x} + \frac{x}{1-x} + x(1-x)]$$

$$P_{qg} = \frac{1}{2}[x^2 + (1-x)^2]$$

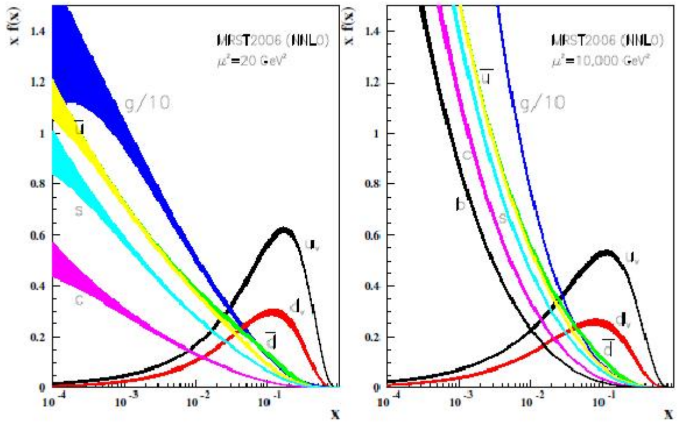

Figure 2.7: Example of proton PDFs measured at $Q^2 = 20\ GeV^2$ and at $Q^2 = 10000\ GeV^2$ in a DIS experiment. The contribution coming from gluon increase with Q^2. Image from [12]

Figure 2.8 shows the measured structure function F_2 as function of x and Q^2 and the evolution predicted by the DGLAP equations.

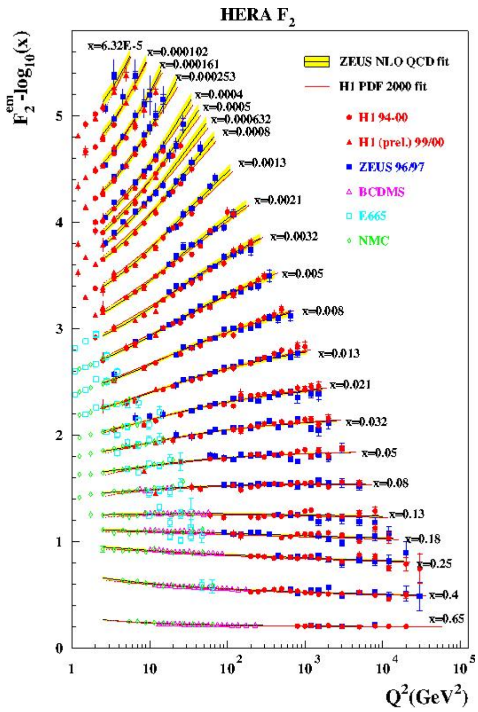

Figure 2.8: Experimental results for F_2 as a function of Q^2 for many different x values, compared to the results of a global fit by the ZEUS collaboration. From [12].

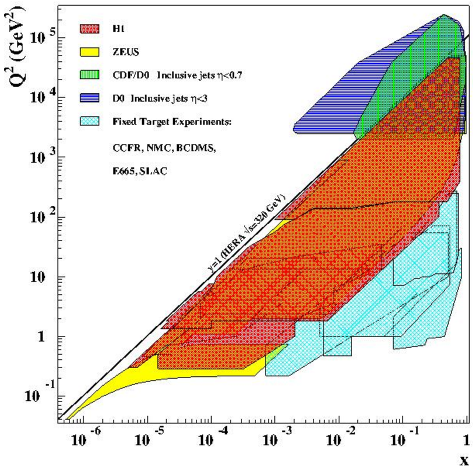

Figure 2.9: Kinematic regions and data sets typically used in PDF fits [12].

In literature and on the common LHAPDF interface [2] different PDF distributions/releases are available. The most commonly used at LHC and Tevatron are CTEQ[3] [17], MSTW[4] [18] and the recent NNPDF[5] [19]. All of these are obtained through global fits to experimental data. Data from different kinematic range (Figure 2.9) are obtained from different experiments such as deep inelastic scattering, Drell-Yan and jet data from Tevatron and fixed target experiments. These three PDF releases differ from each other in many aspects: the input data, the value of α_s, the treatments of heavy quarks, the value of heavy quark masses, the parameterization of PDFs, the implementation of them and the way to treat and to include the experimental uncertainties. Some of these features are summarized in the table 2.1 and the differences for the gluon PDF are shown in Figure 2.10.

	CTEQ	MSTW	NNPDF
parameters	20	20	259
$\alpha_s(M_Z)$	0.118	0.120	0.119

Table 2.1: Comparison between the main important PDF distribution

PDFs are affected by an uncertainty due to the need to combine large number of datasets from different experiments and different theoretical inputs. A way to estimate this uncertainty is based on the Hessian formalism [20]. The extraction of PDFs is based on global fits to data, done through a minimization of an effective global χ^2 in the space of the free parameters. The method to calculate the uncertainties consists in considering the variation of the χ^2 around the minimum neighborhood. The tolerance, T, is an arbitrary parameter in general equal to 10 or 15, tuned in relation to the quality of the agreement with experimental data.

[2] $http://projects.hepforge.org/lhapdf/$
[3] Coordinate Theoretical-Experimental project on Qcd
[4] Martine-Stirling-Thorne-Watt
[5] Neural Network PDF

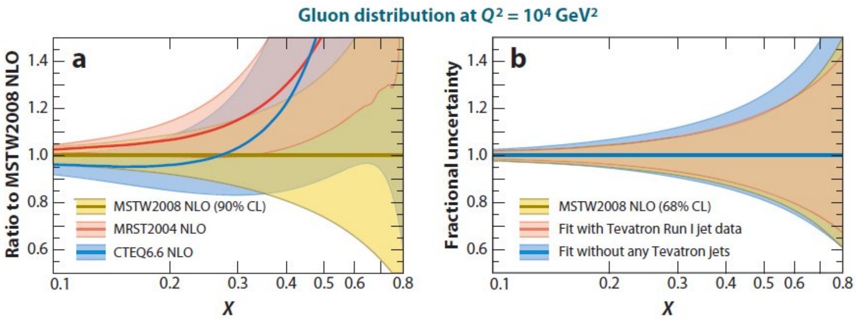

Figure 2.10: PDF gluon distributions comparison between different distributions.

Expanding quadratically one obtains:

$$\Delta\chi^2 = \chi^2 - \chi_0^2 \sim \frac{1}{2}\sum_i\sum_j H_{ij}(a_i - a_i^0)(a_j - a_j^0) \tag{2.9}$$

where a_i are the different free PDF parameters and H_{ij} is the Hessian matrix. The Hessian matrix has a complete set of orthonormal eigenvectors and the displacements from the minimum are conveniently expressed in terms of those. Therefore for each eigenvector, the displacements around the minimum in the direction along the vector, a_i^+ and a_i^- for the i-th eigenvector, can be found, which would represent the up and down uncertainty of the parameter a_i^0.

The uncertainties in the pQCD cross section prediction due to the PDFs are determined in the following way:

$$\delta\sigma^+ = \sqrt{\sum_i (\max(\sigma(a_i^+) - \sigma(a_0), \sigma(a_i^-) - \sigma(a_0), 0))^2}$$

$$\delta\sigma^- = \sqrt{\sum_i (\min(\sigma(a_i^+) - \sigma(a_0), \sigma(a_i^-) - \sigma(a_0), 0))^2}$$

where $\sigma(a)$ is the prediction of the cross section determined using the PDFs with the parameters in vector a.

2.2.2 The hard scattering and its evolution

When hadrons collide, there is a large probability that they will break up and resulting hadrons will continue with very low transverse momenta with respect to the beam direction, however sometimes hard interactions occur, where large transverse momenta particles are produced. This hard interaction can be evaluated with Matrix Element (ME) methods and perturbative QCD using Feynman rules. The evolution of the final state partons can be described by parton showers. A parton shower represents an approximate perturbative treatment of QCD dynamic up to scales of ~ 1 GeV (cut-off). At this scale the coupling

becomes quite strong and hadronization begins to play an important role, clustering partons in a colorless bunch.
Parton showers identify and sum the logarithmic enhancements due to soft and collinear configurations. Soft means that the emitted gluon occurs with very low energy and collinear when a quark or gluon splits into two almost collinear partons. Because of the enhancements due to soft emissions (or small angles), they are only an approximation of the hard gluon emission component (large angles). This model is used in MC generators for initial and final state radiation. They can be combined with phenomenological models of hadronization which take over for energies below the cut-off scale.

Two important aspects of the gluon emission after hard scattering are the angular and color ordering. The angular ordering consists in the continuous reduction of the angle of gluon radiation, so the gluon emission results, in its evolution, more and more collinear with the quark. On the other hand, color ordering forces the $q\bar{q}$ pairs that are in the color singlet to be close in phase space achieving a sort of confinement. Both processes have interesting consequences for the hadronization because they prepare the confinement and the clustering in colorless hadrons.

The fact that color always flows directly from the emitting parton to the emitted one and the softening of the radiation emitted at later stages ensure that partons form a color-singlet cluster close in the phase space. As a consequence, hadronization occurs locally and only partons nearby are involved. This was formulated as Local Parton Hadron Duality [21] which states that the transition from partons to hadrons is local in the phase space. Therefore, the hadrons direction and their kinematic are closely related to the original partons.

2.2.3 The hadronization

The perturbative theory is valid until the partons reach energies of ~ 1 GeV (infrared cut-off). That is the energy where the strong coupling constant becomes quite strong and non-perturbative effects become important. The most important of them is the hadronization, which converts partons into the observed hadrons. There are two important concepts in hadronization: the local parton to hadron duality and the low scale effective α_s that permits to extend the use of perturbative QCD also to low scales. These two principles are used in the models implemented in MC event generators, the string model (Lund) [22] implemented in Pythia and the cluster model [23] implemented in Herwig.

The cluster model

In this model, perturbative QCD uses parton evolution until low energy (beyond the infrared cutoff) is reached and it is based on its preconfinement properties due to angular and color ordering. At this point the gluons are forced to decay in a $q\bar{q}$ pair and all quarks are clustered in color singlet with a mass of a few GeV. These clusters characterized by mass and flavor quantum numbers are treated as resonances that decay into two hadrons proportionally to their phase space. Heavy clusters could decay into smaller clusters, that afterwards decay into hadrons. This is a simple model that successfully describes the characteristics of hadron distributions in jet fragmentation but it forces perturbative QCD beyond its limits of validity.

The string and Lund Model

In this model the QCD potential between two quarks at low scales is parameterized by field lines seen to be compressed to a tube-like region by self interactions among soft gluons. The potential (Figure 2.11) is given by:

$$V(r) = \frac{4\pi}{3r} + kr \tag{2.10}$$

where r is the distance between the two quarks, and k is the constant of the QCD potential ($k \approx 1GeV/fb$ from hadron spectroscopy). The first term represents the Coulomb potential that has effects only at low distances, so it is only fundamental in the internal organization inside hadrons and not in their formation.

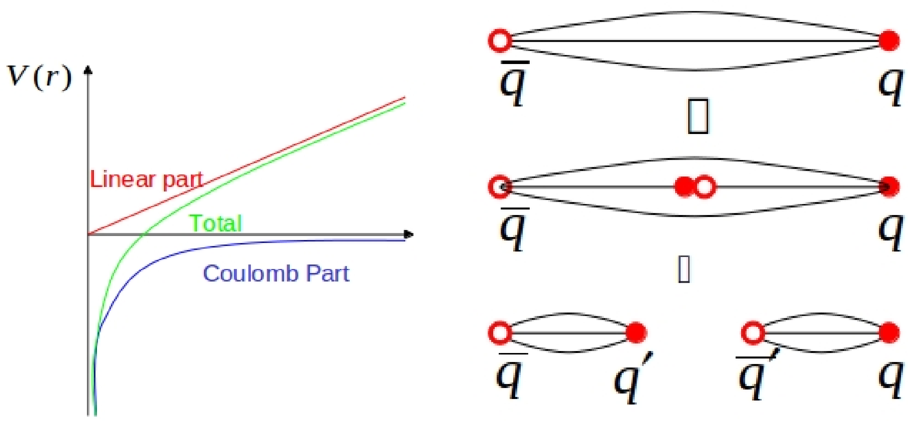

Figure 2.11: QCD potential and string model scheme.

In this context string represents the field line connecting two quarks and the force field is linearly increasing with the distance according to the QCD potential. The hadronization dynamics is described by the dynamics of the string. Therefore as the two original quarks separate from each other the potential energy grows linearly until it reaches a level beyond which the string breaks forming another $q^{'}\bar{q}^{'}$. Thus two new strings are obtained, both with determined energy, mass and quantum numbers. If the invariant mass of the $q\bar{q}^{'}$ or $q^{'}\bar{q}$ pairs is sufficient the strings can break again, otherwise the process stops.
In particular in the Lund string model (Figure 2.12) is assumed that the process continues until all hadrons are on-shell. The hadrons produced retain a fragment of the original quark momentum.
The string model is collinear and infrared safe, i.e. the emissions of a collinear and/or soft gluon does not affect the fragmentation of a string as approaching the small angle/energy

limit, but it is not able to take into account for collective phenomena that could eventually happen in the high-energy hadronic collisions since it considers only independent strings.

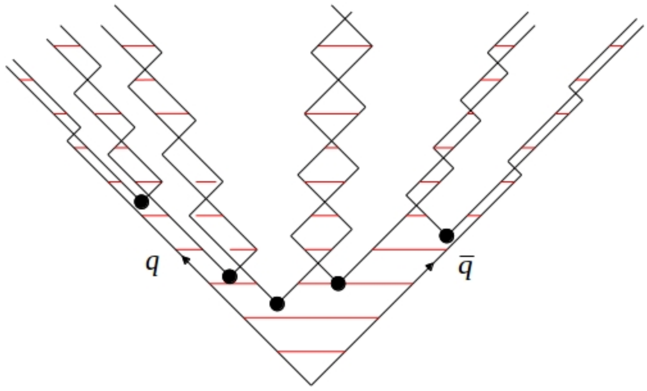

Figure 2.12: Lund Model

2.2.4 Underlying event

Another phenomenon that needs to be considered in hadron colliders is the underlying event (UE). This is originated by secondary interactions between beam remnants and between partons that do not participate in the hard interaction (MPI). These processes make difficult the task of identifying the particles from the hard scattering. UE models are tested against sensitive observables such as jet shapes and event profile.

2.2.5 Multiple Interactions

In a hadron collider, hadrons collide in bunches, therefore usually more than one collision occur in the same bunch crossing. This is known as pileup and its frequency is proportional to the luminosity.

2.3 Jet definition

As the fundamental QCD signature is jet production, having a proper jet definition is crucial to understand the relation between theory and experiment and the long distance degrees of freedom observed in the detector to the short distance colored partons (see Figure 2.13 for an illustration of jet at theoretical and experimental levels).

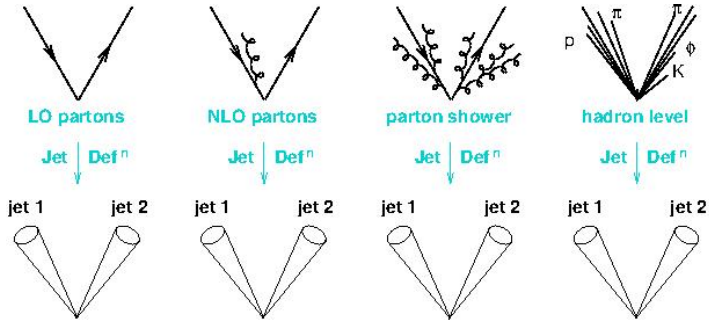

Figure 2.13: Jets at different orders of perturbation theory and at a different points in the analysis.

2.3.1 Jet Algorithms

The jet definition comprises a set of rules that determine how to group particles into a jet and how to calculate the resulting four-momentum. Jet algorithms set the procedure to group the particles to have a stable jet, and the jet recombination defines how the jet four-momentum is evaluated combining the particles four-momenta.
Along the different decades and through the different experiments a large combination between jet algorithm and jet recombination was used giving a large spectrum of jet definitions. Fundamental properties that a jet definition should follow the layout elaborated during the year 1990 which are known as Snowmass accord [24] :

- simple to implement in experimental analysis;
- simple to implement in the theoretical calculation;
- defined at any order of perturbation theory;
- yields finite cross sections at any order of perturbative theory;
- yields a cross section that is relatively insensitive to hadronization.

In particular from a theoretical point of view the ideal jet algorithm should be infrared safe, collinear safe and invariant under boost transformations.
The infrared and collinear safety are two important concepts which concern the singularity present in Feynman diagrams when a parton emits a soft gluon and an outgoing parton splits into two collinear partons. Being infrared safe means that no infrared singularities appear in the perturbative calculations and that it is insensitive to the soft radiation in the event. This implies that an emission of a soft gluon does not change the number of jets reconstructed in the event.
On the other hand, to be collinear safe means that collinear singularities do not appear in the perturbative calculation and that jets are insensitive to collinear radiation in the events. This guarantees that the jets found in the event when splitting a particle with two collinear particles do not change (Figure 2.14).
From the experimental point of view, it is crucial that jet algorithm should be detector independent, should not amplify the effects of resolution smearing and should be implemented

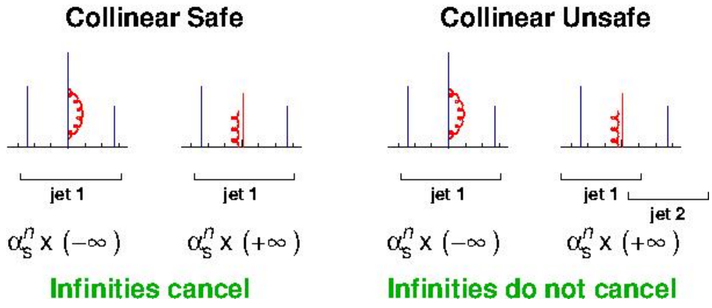

Figure 2.14: Illustration of collinear safety and collinear unsafety in a iterative cone algorithm, together with the implication for perturbative QCD calculation. Partons are drawn with vertical lines. Their height is proportional to their transverse energy, and the horizontal axis indicates the rapidity. Plot from [26]

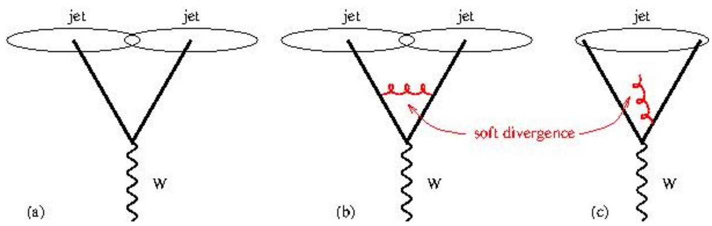

Figure 2.15: Illustration of Infrared unsafety for iterative cone algorithm in events with a W and two partons. The addition of a soft gluon converts the event from having two jets to just one jet. Scheme taken from [26]

with a minimum of computer time.
There are two categories that group all the different kinds of jets: the cone algorithm that group the particles inside a stable cone and a clustering algorithm that works by grouping together nearby objects by pair-wise. In the following sections the advantages and the disadvantages of the different types are treated in detail.

2.3.2 Cone Algorithm

Cone algorithms [25], based on the first jet definition done by Sterman and Weinberg, form jets by associating together particles whose trajectories end up within a circle of specific radius R in $\eta \times \phi$ space. Starting with a trial geometric center for a cone in $\eta \times \phi$ space, the energy weighted centroid is calculated including contributions from all particles within the cone. This new point is used as the center for a new trial cone. As this calculation is iterated the cone center is followed until a stable solution is found, i.e. until the centroid of the energy depositions within the cone is aligned with the geometric axis of the cone. A problem may arise with this definition when particles are shared by two cones. A split-merge procedure is usually run in this case, which would merge the pair of cones if more than a fraction f of the softer transverse momentum cone is shared with the harder one. Otherwise, shared particles are assigned to the closer cone.

At CDF a first jet cone algorithm (JetClu07) was developed. It used the centers of seed particle that passed a minimum energy cut as the starting points to look for the stable cone . In this way, there is no need to look everywhere and it is more efficient computationally, but the introduction of the seed has as a consequence: the jets are collinear and infrared unsafe, as it is illustrated in the example in Figures 2.14 and 2.15.
In order to avoid the seeds that generate these problems, the Seedless-Cone algorithm which is infrared and collinear safe, was introduced. The only problem concerning this algorithm is its expensive computation. An alternative algorithm was the Midpoint. This is a seed cone algorithm that considers also the midpoint between seeds as the starting points. This is computationally faster and it is infrared-safe up to a 3+1 order, meaning 3 hard particles in a common neighborhood plus one soft one (Figure 2.16).

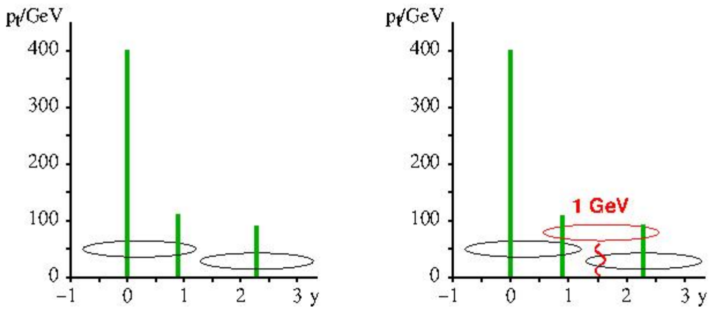

Figure 2.16: Configuration that is the source of Infrared unsafety in Midpoint algorithm with the diagram in the right showing the extra stable cone that can appear with the addition of a new soft seed. From [26]

2.3.3 Clustering Algorithm

The cluster algorithm groups nearby objects pair-wise in relation of the generic distance between two object i,j. This is given by:

$$d_{ij} = \min(p_{t,i}^{2p}, p_{t,j}^{2p}) \frac{\Delta R_{ij}^2}{R^2} \tag{2.11}$$

where $\Delta R_{ij} = (y_i - y_j)^2 + (\phi_i - \phi_j)^2$ and $p_{t,i}$ is the transverse momentum of i object and R is a parameter similar to that of R in cone algorithm.
There are three cluster algorithms that differ only based on the definition of the distance d reported before: for $p = -1$ the anti-kt algorithm, for $p = 0$ the Cambridge/Aachen algorithm and for $p = 1$ the kt one. All of these are infrared and collinear safe.
As seen in Figure 2.17 the anti-kt algorithm is more cone-like, it is infrared and collinear safe and it is not sensitive to pile up. The computer time to build it is the lowest among the algorithms in use at hadron colliders.

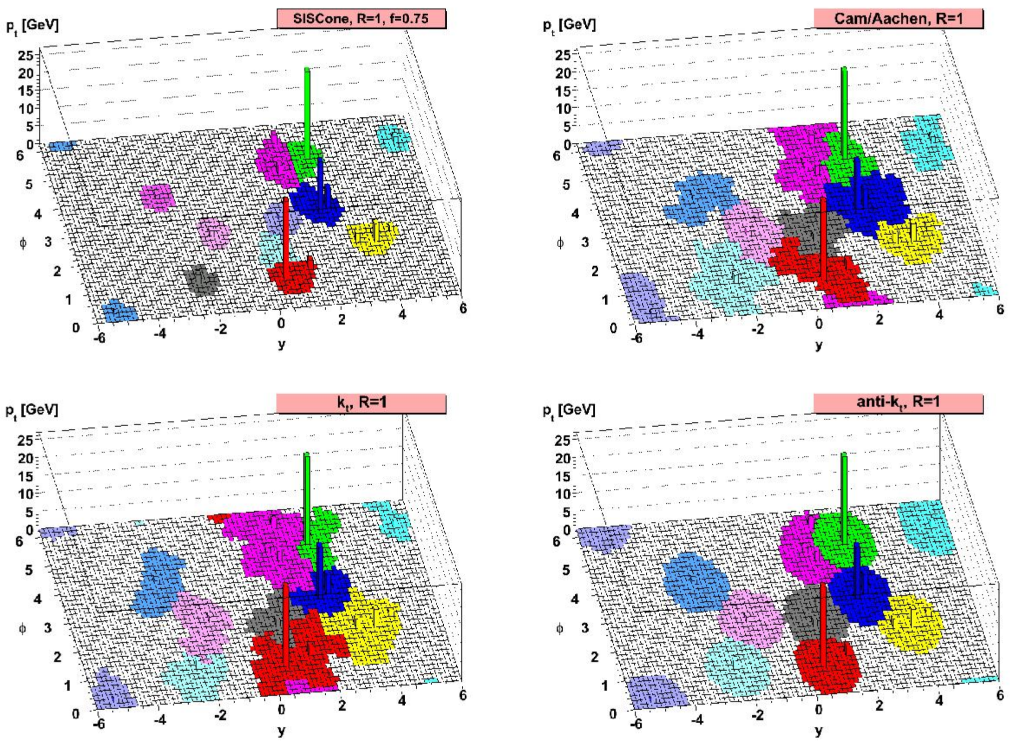

Figure 2.17: A sample parton-level event clustered with four different jet algorithm. From [12].

2.4 Predictive tools

MC event generator programs are widely used at hadron colliders. They are useful tools that can help in various experimental stages, from a detector design study to the optimization of an analysis strategy and many more in between. Given the complexity of the calculation of a physics process at hadron colliders different approaches are used to simulate events, some of them are discussed below.

2.4.1 Perturbative fixed order calculations

Processes of interest at hadron colliders involve large momentum transfers which can be described by perturbation theory. Computations can be done for example using Feynman diagrams. The simplest implementation would be to consider the diagrams corresponding to the emission of real particles. In this case, the number of emissions corresponds to the perturbative order in α_s. These tree-level generators describe final states to the lowest order, matrix elements (ME) would not include virtual loops. Leading order (LO) ME includes only the calculation of tree-level diagrams in kinematic regions in which their contributions are finite. Therefore the simplest approach is to carry out a Monte Carlo integration over phase-space points with a subroutine that determines whether a given phase space point passes cuts and it calculates the squared matrix elements and PDF factors.

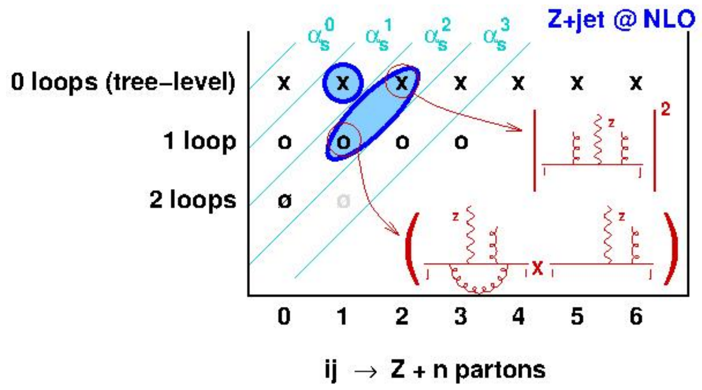

Figure 2.18: Illustration of the contributions that are known for $ij \to Z + N$ partons where i and j are arbitrary incoming partons, according to the number of outgoing partons, the number of loops are the number of powers of the coupling. An x means a squared tree-level diagram, and o represent the interference of 1-loop diagram with a tree diagram, while $\emptyset$ represents the interference of a two-loop diagram with a tree one. The entries in the shaded ellipses are those that are relevant for NLO calculation of the cross section for the production of a Z boson with a jet.

The problem with LO predictions is that despite they may render reliable distributions, the absolute normalization is in general badly described due to large contribution coming from higher order corrections. It is common to introduce a K factor when comparing results from these event generators to experimental data. This K factor is often determined as the ratio between NLO cross section predictions to the LO one.
Many MC programs are able to produce LO predictions, in particular for large multiplicities one of the most frequently used is Alpgen [27].

Alpgen

It is a tree-level ME generator and allows to calculate multi-partons (up to 10) cross sections for processes in hadronic collisions. It uses the ALPHA [28] algorithm to compute tree level scattering amplitudes for large parton multiplicities in the final state. It can be evaluated in a reasonable CPU time as the advantage of ALPHA is that its complexity increases slower than the number of Feynman diagrams when increasing the particles in the final state. Events can be processed through shower evolution and hadronization programs such as PYTHIA [29] (described below).

NLO predictions

Higher order calculations, which include loop effects, are not fully automated. They consist of more than just one matrix element with a fixed number of final state particles as they include terms with extra particles in loops and legs (Figure 2.18). This extra emission introduces infrared divergences which must cancel between the various terms. This is done technically with infrared subtraction methods. In pursue of higher accuracy many processes can be now calculated at next-to-leading-order (NLO). One must note that NLO calculations can be computing intensive. Example of NLO generators are MCFM [30] and BLACKHAT [31].

MCFM

Literally a Monte Carlo for FeMtobarn processes, it is a NLO ME event generator that provides predictions for a large range of process at hadron colliders. MCFM uses the dipole method to cancel the infrared divergence between real and virtual one loop contribution. It was developed by Campbell et al. and it has had a good success when compared with Tevatron results.

2.4.2 Parton Shower

The problem with ME generators is that they do not cover the regions where partons become soft and collinear and they stop the prediction at parton level. Parton Shower MC takes into account the soft radiation and it evaluates higher orders based on these two concepts:

- an iterative structure that allows simple expressions for $q \to qg$, $g \to gg$ and $g \to q\bar{q}$ branchings to be combined to build up complex multi-parton final states
- a Sudakov factor that offers a physical way to handle the cancellation between real and virtual divergences

The starting point is to factorize a complex $2 \to n$ process, where n represents a large number of partons in the final states, into a simple core process convoluted with shower as in Figure 2.19.

Here there could be Initial (ISR) and Final (FSR) state radiation, where the probability to emit gluons is described by the DGLAP equation. These can blow up the probability in soft and collinear regions. Thus a Sudakov form factor [33] is introduced, which expresses the probability of not emitting a gluon above a certain momentum scale and which ensures that the total probability for a parton to branch never exceeds unity.

The implementation of a cascade evolution is illustrated in Figure 2.20. Starting from a simple $q\bar{q}$ system the q and $\bar{q}$ are individually evolved downwards from the initial Q until they branch. In a branching the mother parton disappears and is replaced by two daughter partons, which in turn are evolved downwards and they may branch. Therefore the number of partons increases until the infrared cutoff scale is reached.

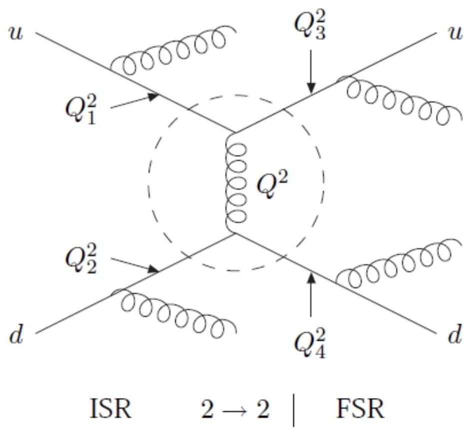

Figure 2.19: $2 \to n$ factorization PS scheme. Taken from [32]

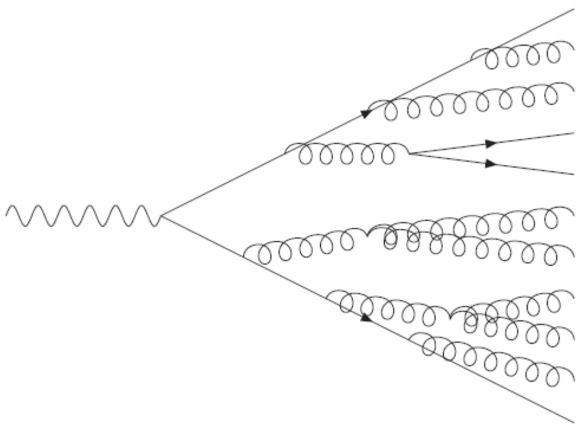

Figure 2.20: Shower Cascade. Taken from [32]

PYTHIA

Pythia 6.425 is a Monte Carlo event generator program that begins with a leading order hard process. Although it is optimized for $2 \to 1$ and $2 \to 2$ final states, there are some processes available with three or more partons in the final state. Currently there are almost 300 different processes implemented. Higher order effects are simulated by evolving the event through parton showers. Resulting partons from this process are group together and hadronized. The hadronization is modeled by the string Lund model explained previously. Also the underlying structure (underlying event) can be included. The current version differs from the previous one as it utilizes p_t-ordered parton showers instead of the virtuality-ordered one[34].

MC tuning and Perugia2011

Monte Carlo event generators are based on various phenomenological models and have several free parameters that are a priori unknown. MC programs are therefore tuned to experimental data. The problem lies on the quantity of parameters and correlations between them. The overall task is divided in parts: parton shower, hadronization and UE. In general data from LEP are used to tune flavor parameters and fragmentation (event shapes and b hadron measurements). To tune the UE distributions from CDF and D0 are used.
Tunes that have been used in this analysis are Tune A [35] , Tune DW and Perugia2011 [36]. For the latter early LHC Data are included and it uses the same value of Λ_{QCD} for all shower activity, given a coherent choice of α_s in the matching between ME generators and parton shower. Tune A and Tune DW, based on CDF Run I data , reproduces well the underlying event. The latter uses also Run II data and describes well the $P_{T,Z}$ distribution[37].

2.4.3 ME+PS

As we have seen, both matrix elements (ME) and parton showers (PS) have advantages and disadvantages. Summarizing, ME allow a systematic expansion in powers of α_s, and thereby offer a controlled approach toward higher precision. Calculations can be done with several partons in the final state, as long as only Born-level results are asked for, and it is possible to select the phase space cuts for these partons precisely to the experimental needs. Loop calculations are much more difficult, on the other hand, and the mathematically correct cancellation between real and virtual emission graphs in the soft collinear regions is not physically sensible. Therefore ME cannot be used to explore the internal structure of a jet and are difficult to match to hadronization models which are supposed to take over in very soft/collinear region.
PS, on one hand, clearly are approximate and do not come with a guaranteed level of precision. The efficiency in obtaining events in a specific region of the phase space can be quite low. On the other hand, PS are universal, so for any model it is only necessary to provide the basic hard process and then PS will turn that into reasonably realistic multi-partons topologies. The use of Sudakov form factors ensures a physically sensible behavior in the soft collinear regions and it is also here that the PS formalism is supposed to be the most reliable. It is therefore possible to obtain a good picture of the internal structure of jets and to provide a good match to hadronization models.

Since the two methods complement each other, it would be highly desiderable to combine

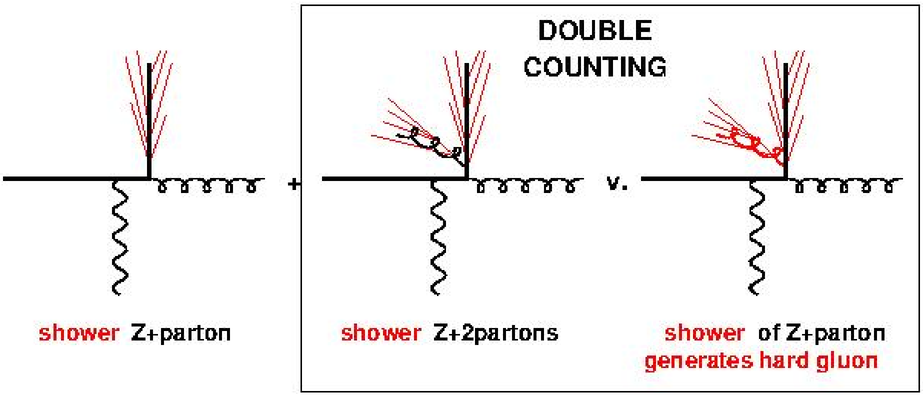

Figure 2.21: Example of double counting for MEPS MC.

them. To do this, double counting needs to be overcome (Figure 2.21). Several methods have been developed for this purpose. The most popular are the MLM [38] (Figure 2.22) and the CKKW techniques.

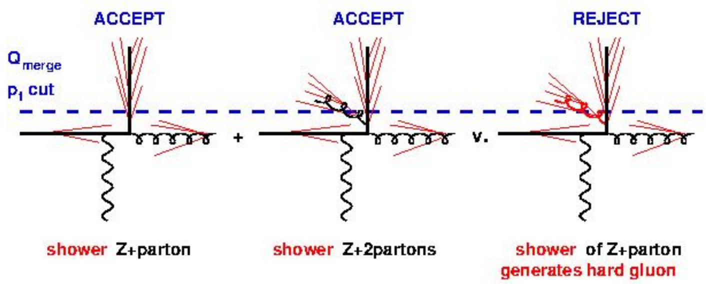

Figure 2.22: MLM mechanism.

In particular the MLM matching proceeds as follows:

- introduce a transverse momentum cutoff Q_{ME} and an angular cutoff R_{ME} for matrix elements generation
- generate tree level hard matrix where all partons must have $p_t \geq Q_{ME}$ and be separated from another parton by an angle greater than R_{ME}. The numbers of events that one generates in the different samples are proportional to their cross section with these cuts
- for each tree level event these samples are showered with a parton shower program
- apply a jet algorithm to the shower event and identify all jets with $p_T \geq Q_{merge}$ where the merging scale is taken greater then Q_{ME}
- if each jet corresponds to one of the partons and there are no extra jets above scale Q_{merge} then accept the events

- otherwise reject the event

Examples of these Monte Carlo programs are Alpgen matched to Pythia and for NLO ME plus PS MC@NLO [39] and POWHEG+Pythia [40].

3 $Z + b$ Theoretical predictions

The production of heavy flavor in association with a vector boson is a challenging topic both theoretically and experimentally. In terms of the theory, it is a lively area, constantly releasing new developments. This chapter describes the theoretical approaches for the calculation of the $Z + b-$jets production and the tools developed for such purpose.

3.1 Introduction: the 4FNS and the 5FNS scheme

Processes involving b quarks are generally described in QCD by two theoretical schemes: the five flavor scheme (5FNS) or variable scheme (VFS) and the four flavor scheme or fixed scheme (4FNS or FFS).

In the FFS or 4FNS only 4 massless-quark densities are considered in the initial state and non-zero mass b quarks are arising in final states through gluon splitting, while in a VFS or 5FNS [1] an initial state massless b quark density is introduced. This b quark density is considered to be originated from a gluon splitting $g \rightarrow b\bar{b}$ where one heavy quark remains at low p_T and it is integrated out, while the other participates in the hard scattering and emerges at high-p_T. Thus its distribution function can be evaluated perturbatively via the DGLAP equations.

The two approaches are equal at all orders in perturbative theory but may give very different results at finite order. Both schemes are implemented to perform $Z+b$ predictions in different event generators.

Below is a review of the predictions available for different processes:

- $Z + 1$ jet+X: Z plus one single jet with one or more heavy flavor quarks. The complete details of the calculation can be found in [42]. It is performed with MCFM in the 5FNS scheme. This is perfectly suitable to describe inclusive $Z + 1$ jet events with 1 $b-$tag;
- $Z + 2$ jets+X: Z plus two jets with one or more heavy flavor quark, the calculation is done with MCFM and it is described in [43]. This is suitable for $Z + 2$ jets events with 1 b-tag.
- $Z + b\bar{b}$ NLO: Z in association with a bottom-antibottom pair. The calculation of the NLO radiative corrections is done in the massless hypothesis with MCFM [44]
- $Z + b\bar{b}$ NLO in 4FNS and in non-zero mass approach [45]
- $Z + b\bar{b}$ NLO in 4FNS with $m_b > 0$ plus parton shower, $aMC@NLO$ [46].

[1] Since the scale is much larger than the mass of the b quark the VFS and 5FNS coincide, for best explanation of VFS please refer to [41].

All these three processes are different since the Feynman diagrams that contribute in the calculation are also different. In the following sections we will analyze each process, showing the LO and NLO subprocesses.

3.2 Associated production of a Z boson and a Single Heavy quark Jet

The main Leading-Order contribution for this process is $gb \to Zb$ and the tree Feynman diagrams are shown in Figure 3.1. They are of order α_s in the 5FNS scheme since the b quark is present in the initial state.

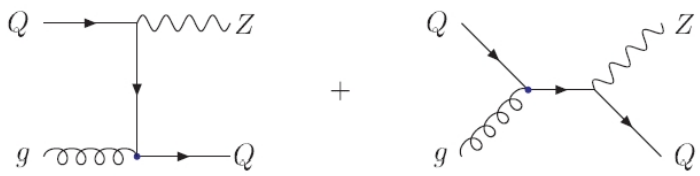

Figure 3.1: LO diagrams for $gb \to Zb$.

This process can be evaluated at NLO ($\mathrm{O}(\alpha_s^2)$) taking into account 1 loop and real corrections.

Another process that contributes to $Z + b$ is $q\bar{q} \to Zb\bar{b}$, where one or two b-jet can be detected. Only one b-jet may be detected if the two quarks are collinear and they end up in the same jet or if one b-jet falls outside the coverage of the detector. In this case it is necessary to introduce the mass of the quark to regulate the divergence arising from a gluon splitting. Due to this complexity in MCFM this process is available only at LO.

The MCFM NLO cross section for inclusive b-jet production is given by:

$$\sigma_{Z+b-jet} = \sigma_{gb\to Zb} + \sigma_{q\bar{q}\to Zb\bar{b},1tag} + C_{DC} + 2\cdot\sigma_{q\bar{q}\to Zb\bar{b},2tag} \tag{3.1}$$

where $\sigma_{gb\to Zb}$ is calculated at NLO, C_{DC} is a correction for double-counting [30] and $\sigma_{q\bar{q}\to Zb\bar{b}}$ are estimated at LO in the $b-$mass hypothesis. The calculation is therefore done at ($\mathrm{O}(\alpha_s^2)$), though the remaining LO component makes the prediction quite sensitive to the scale variations.

In Alpgen this cross section is calculated considering only the tree level diagrams and in the b-quark mass hypothesis (4FNS or Massive ME). The complete sample is generated through the different multiplicity sub-samples: $Z + b\bar{b}$, $Z + b\bar{b} + 1jet$ up to almost three light jets in the final state. The inclusive $Z + b$ final state is treated as $gg \to Zb\bar{b}$, summing over the phase space of the $\bar{b}$ quark.

3.3 Z+ 2 jets with one b-quark jet

The $Z + 2$ jet with one or more b jets is an extension of the previous one. The processes that contribute at LO are :

- $bg \to Zbg$ and $bq \to Zbq$
- $gg \to Zb\bar{b}$ and $q\bar{q} \to Zb\bar{b}$ (Figure 3.2)

Figure 3.2: Diagrams contributing to the associated production of a Z boson and two high-p_T jets.

The NLO prediction can be obtained with MCFM. The process involved in the calculation are:

- $q\bar{q} \to Zb\bar{b}$ at tree level and one loop;
- $gg \to Zb\bar{b}$ at tree level and one loop
- $bq \to Zbq$ at tree and one loop;
- $bg \to Zbg$ at tree level and 1 loop;
- $q\bar{q} \to Zb\bar{b}g$ at tree level and in non-zero mass hypothesis;
- $gg \to Zb\bar{b}g$ at tree level;
- $bg \to Zbgg$ at tree level;
- $bq \to Zbgg$ at tree level;
- $gq \to Zb\bar{b}q$ at tree level and in non-zero mass hypothesis;
- $bg \to Zb\bar{q}q$ at tree level;

All these processes are evaluated in the massless hypothesis except those where two b quarks end up in the same jet.

3.4 Z + two high p_T b-quark jets

The principal contribution of $Z+$ two $b-$jets final state is coming from $gg \rightarrow Zb\bar{b}$ and from $q\bar{q} \rightarrow Zb\bar{b}$. Some diagrams including real corrections are found in Figure 3.3.

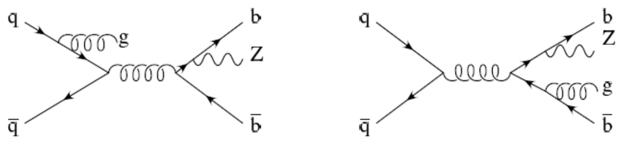

Figure 3.3: Diagrams contributing to $q\bar{q} \rightarrow Zb\bar{b}$.

It is particularly challenging to predict the cross section for Z with two high p_T b-tag jets. In the massless approach, the prediction can be obtained with MCFM, ignoring the low p_T phase space. Another is presented in Febres Cordero et al. [45]. This prediction is based on the 4FNS scheme with non-zero mass hypothesis. Finally, it is interesting the approach of *aMC@NLO* that includes the NLO correction, bottom quark mass effects, spin correlation, showering and hadronization. Taking into account the b mass, it is possible to estimate the cases in which one of two b is not observed and can have small transverse momenta.

4 The Experimental Enviroment

The events analyzed in this thesis were produced as a result of proton - antiproton collisions at a center-of-mass energy of 1.96 TeV at CDF (Collider Detector at Fermilab), one of the two general purpose detectors within the Tevatron ring.
In this chapter, the CDF II detector and the Tevatron accelerator chain will be described in detail.

4.1 The Fermilab Tevatron collider

Tevatron [47] is an underground circular proton-synchrotron with 1 km of radius. It is the last stage of the accelerator system (Figure 4.1) located at Fermi National Accelerator laboratory (Fermilab) in Chicago (IL, USA). Before the LHC start-up, Tevatron was the most powerful hadron collider in the world. It is a proton-antiproton collider where bunches of protons, circulating clockwise and spaced by 396 ns, collide against a similar beam of antiprotons accelerated in the opposite direction, both at energies of 980 GeV.

The Tevatron performance, as a collider, is evaluated in terms of two parameters: the available center-of-mass energy $\sqrt{s}$, and the instantaneous luminosity, $\mathscr{L}$. The first defines the accessible phase-space for the production of particles in the final states, while the latter is

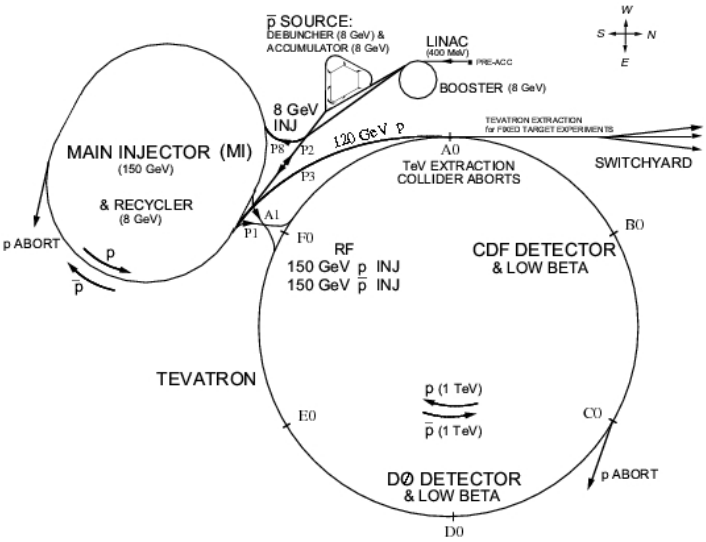

Figure 4.1: Illustration of the complete accelerator chain at Fermilab.

the coefficient of proportionality between the rate of a given process $\frac{dN}{dt}$ and its cross section σ, as expressed by the following formula:

$$\frac{dN}{dt}[events\ s^{-1}] = \mathscr{L}[cm^{-2}s^{-1}] \times \sigma[cm^2]$$

The time-integral is therefore a measured of the expected number of events N(T) produced in a finite time T:

$$N(T) = \int_0^T \mathscr{L}\sigma dt$$

Assuming an ideal head-on $p\bar{p}$ collision with no crossing angle between the beams, the instantaneous luminosity is defined as:

$$\mathscr{L} = 10^{-5}\frac{N_p N_{\bar{p}} B f \beta\gamma}{2\pi\beta^* \sqrt{(\epsilon_p + \epsilon_{\bar{p}})_x(\epsilon_p + \epsilon_{\bar{p}})_y}} F(\sigma/\beta^*)$$

where N_p ($N_{\bar{p}}$) is the average number of protons (antiprotons), B is the number of circulating bunches, f is the revolution frequency, $\beta\gamma$ is the Lorentz relativistic factor and $F(\sigma_z/\beta^*)$ is an empiric hourglass factor, which is a function of the ratio between the longitudinal r.m.s. width of the bunch (σ_z) and the beta function calculated at the interaction point (β^*), and the 95 % normalized emittance of the beams ($\epsilon_p \sim 18\pi$ mm mrad and $\epsilon_{\bar{p}} \sim 13\pi$ mm mrad after injection)[1].
The main parameters of Tevatron accelerator are summarized in the Table 4.1.

Parameter	value
energy of center-of-mass ($\sqrt{s}$)	1.96 TeV
number of bunches (B)	36
space between bunches	396 ns
width of the bunch (σ_z)	60 cm
bunch average number of protons (N_p)	3×10^{11}
bunch average number of antiprotons ($N_{\bar{p}}$)	3×10^{10}
beta function (β^*)	31 cm
luminosity peak	$4.08 \times 10^{32}\ cm^{-2}s^{-1}$

Table 4.1: Summary of the main Tevatron characteristics.

The limiting factor for the luminosity is the capability to create a monochromatic beam of antiprotons that can be transmitted efficiently without dispersions into the entire accelerator

[1]The hourglass factor is a parameterization of the longitudinal profile of the beams in the collision region, which assumes the shape of an horizontal hourglass centered in the interaction region. The beta function is a parameter convenient for solving the equation of motion of a particle through an arbitrary beam transport system. The emittance ϵ measures the phase-space occupied by the particles of the beam. Three independent two dimensional emittances are defined. The quantity $\sqrt{\beta\epsilon}$ is proportional to the r.m.s. width of the beam in the corresponding phase plane.

chain.
In the following paragraph the proton/antiproton production and the several acceleration steps to reach the energy of 980 GeV are explained.

4.1.1 Proton and Antiproton production

The proton production begins with hydrogen ionization: hot hydrogen gas is passed through a magnetron, which extracts a 50-55 mA current of 15-22 keV H^- ions, subsequently accelerated to 750 keV by a Cockroft-Walton accelerator. The hydrogen ions beam, segmented into bunches, is then injected into a 150 m long Linac where hydrogen ions increase their energy up to 401.5 MeV before the injection into the Booster.
The Booster is an alternating gradient synchrotron with an orbit of 85.5 m that accelerates protons to 8 GeV in 33 ms. At injection, a thin carbon foil is used to strip the electrons from the H^- ions to obtain protons. Injecting H^- ions rather than protons into the Booster allows the injection to proceed over multiple revolutions of the beam around the Booster ring. If protons were used instead, the magnetic field used to inject new protons into orbit in the Booster would also deflect the already revolving protons out of orbit.
Here proton and antiproton production processes become different. Two basic modes are characteristic during the collider operations: antiproton accumulation and injection into the main ring.
In the antiproton production, one set of 84 proton bunches is extracted from the Booster at 8 GeV and injected into the Main Injector every 2.2 s. The Main Injector, a circular synchrotron, accelerates the protons up to 120 GeV. These are extracted and directed to impact against a rotating 7 cm thick target.

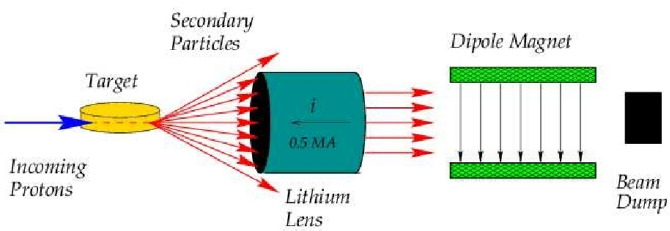

Figure 4.2: Antiproton production.

The particles produced in the interaction are spatially wide spread. They are collected and focused with a cylindrical lithium lens (Figure 4.2). 8 GeV/c negatively charged secondary particles are selected in momentum by a 1.5 T pulsed dipole magnet. The antiprotons created are delivered to the Debuncher storage ring, a triangular synchrotron that transforms the antiproton pulses in a continuous beam of monochromatic antiprotons. Stochastic cooling [48], electron cooling [49] and bunch rotation are applied during many cycles to collimate the beam. From the Debuncher antiprotons are transferred with 60 -70 % efficiency into the

Accumulator where they are stacked and cooled with a variety of systems until the maximum antiproton intensity is reached. Then they are sent to Recycler that is stored in the same ring as the Main Injector and that is useful to maintain the antiproton momenta at 8 GeV, "stacking" the antiprotons that afterwards can be injected into the Tevatron.

4.1.2 Injection and collisions

Every 10-20 h, antiproton accumulation is stopped in preparation for injection. A set of seven proton bunches is extracted from the Booster, injected into the Main Injector accelerated to 150 GeV, coalesced into a single bunch of 300 $\times 10^9$ protons and then injected into the Tevatron. This process is repeated every 12.5 s, until 36 proton bunches, separated by 396 ns, are loaded into the Tevatron central orbit. Then four sets of 7-11 $\bar{p}$ bunches are extracted from the Recycler to the Main Injector, accelerated to 150 GeV, coalesced into four $\sim 30 \times 10^9$ $\bar{p}$ bunches separated by 396 ns, and then injected into the Tevatron. Protons and antiprotons circulate in the same beam-pipe, sharing magnet and vacuum system. The injection process is repeated nine times until 36 antiproton bunches circulate in the Tevatron.
Sweeping the Tevatron RF by $\sim 1kHz$, the beam is then accelerated in about a minute from 150 to 980 GeV. Once the final energy is reached the two counter-rotating particles beams pass through each other colliding at the two instrumented interaction-points located along two straight sections of the Tevatron: D0 and B0, where the D0 and CDF II detectors respectively are situated. This stable situation of 980 GeV proton-antiproton collisions is called a store.

4.1.3 Tevatron performance

Since the beginning of Run II (2001) the Tevatron performance has been steadily increasing until its end of the activity (September 2011) when more than 10 fb^{-1} of data have been collected for each experiment. The plot in Figure 4.3 shows the integrated luminosity since the beginning of Run II.

4.2 The CDFII Detector

The CDFII detector [50] is a large multi-purpose solenoid magnetic spectrometer surrounded by 4π fast, projective calorimeters and fine-grained muon detectors. It is used to record the interactions resulting from the proton-antiproton collisions at a center-of-mass energy of 1.96 TeV. It is a detector designed to measure the energy, momentum and the identity of particles produced in Tevatron collisions combining all informations coming from the different sub-detectors. A cross sectional view of half the detector is shown in Figure 4.4.

Particles produced in the collisions (Figure 4.5) first pass through the tracking detectors where the momentum of charged particles is measured from their curvature, after that they cross the calorimeters, where the energy of electrons and hadrons are deposited. At the end a

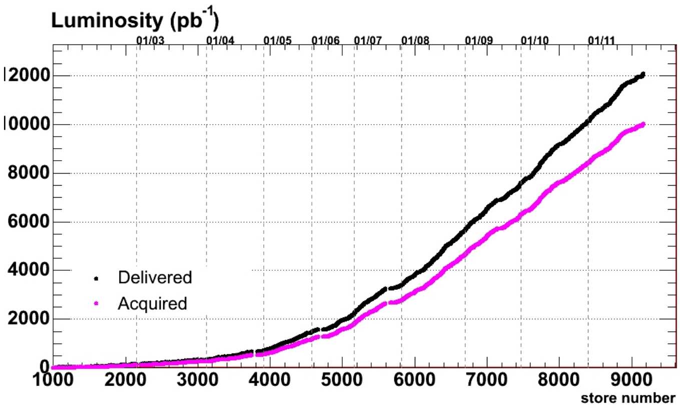

Figure 4.3: Integrated luminosity as a function of time for Run II data-taking. In black curve there is the delivered luminosity while the pink one represents the acquired luminosity, stored on tape.

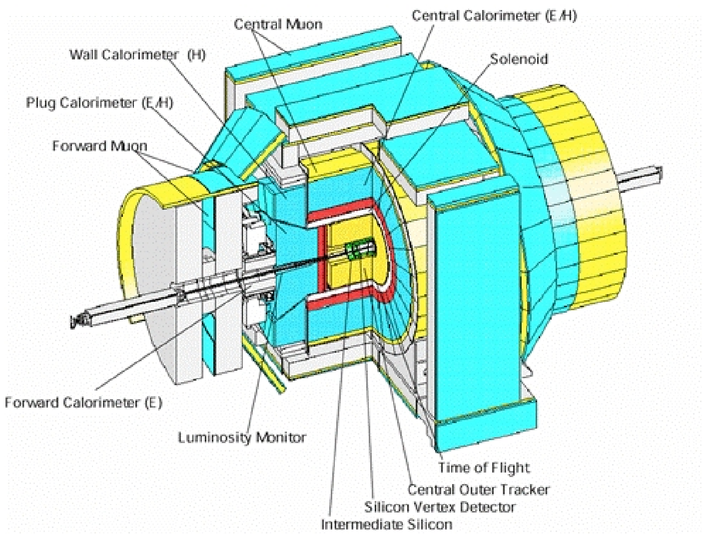

Figure 4.4: CDF II detector sketch in three dimensions.

few of these particles reach the external part where muon detectors detect the passage of any charged particles that escape from the calorimeter. The combined responses of the various detectors permit to identify the different particles.

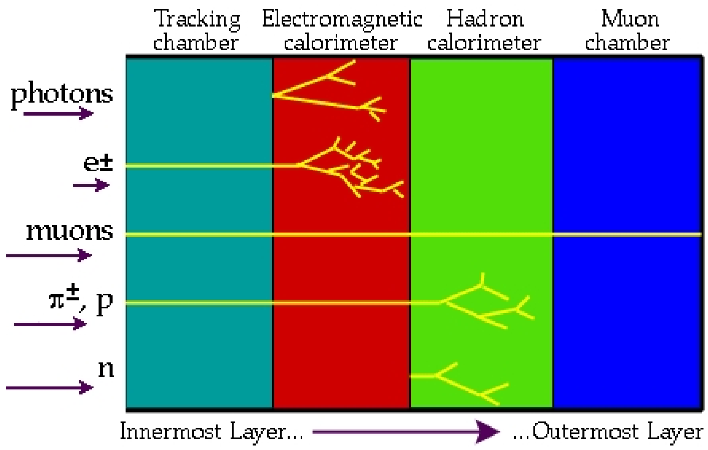

Figure 4.5: Particles identification. The passage of different kinds of particles through the CDFII sub-detectors. Combining all the informations coming from the several sub-detectors we can identify whether the particle is a photon, an electron, a jet or a muon.

The tracking systems are contained in a super-conducting solenoid of 1.5 m in radius and 4.8 in length that generates a 1.4 T magnetic field parallel to the beam axis. The calorimeter and the muon system are outside the solenoid.
The main detector characteristics are an excellent tracking performance, which provides high mass resolution and precisely reconstructed decay vertexes, good electron and muon identification capabilities combined with charged-hadron identification, and an advanced trigger system that fully exploits the high rate events.
Before explaining in detail the several sub-detectors it is worthwhile defining the coordinate system used at CDFII.

4.2.1 The CDFII Coordinate system

The CDFII detector uses a right-handed Cartesian coordinate system with the origin in the B0 interaction point and where the $+z-$axis lies along the nominal beam-line pointing toward the proton direction (east). The (x, y) plane is therefore perpendicular to either beams, with positive y-axis pointing vertically upwards and positive x-axis in the horizontal plane of the Tevatron, pointing radially outward respect to the center of the ring.
Since the colliding beams of the Tevatron are unpolarized, the resulting physical observation is invariant under rotations around the beam line axis, for this reason a cylindrical coordinate system is frequently used to describe the detector geometry. Longitudinal and transverse means respectively parallel and perpendicular to the proton beam direction.
In hadron collision environment, it is common to use a variable invariant under z Lorentz

boosts as unit of relativistic phase-space, instead of polar angle θ. This variable, called rapidity Y, is defined as:

$$Y = \frac{1}{2}\log\left[\frac{E + p\cos\theta}{E - p\cos\theta}\right] \tag{4.1}$$

where (E, p) is the energy four-vector of the particle. However the problem with the rapidity is that its measurement still requires an accurate particle identification capabilities because of the mass term entering E. For practical reasons it is preferably to substitute Y with its approximate expression $\eta = -\log[\tan(\theta/2)$, called pseudorapidity. They are equal in the ultra relativistic limit.

As the event by event longitudinal position of the actual interaction is distributed around the nominal interaction point with 30 cm r.m.s. width, it is useful to distinguish detector pseudo-rapidity, η_{det}, measured with respect to the (0,0,0) nominal interaction point, from particle pseudo-rapidity, η, which is measured with respect to the z_0 position of the real vertex where the particle originated.

4.2.2 The tracking system

The CDFII tracking system (Figure 4.6) is designed to reconstruct the three-dimensional charged particle tracks with high resolution and precision. The system consists of three silicon sub-detectors and a drift chamber (COT). It is located inside a super-conducting solenoid which generates a 1.4 T magnetic field parallel to the beam axis.

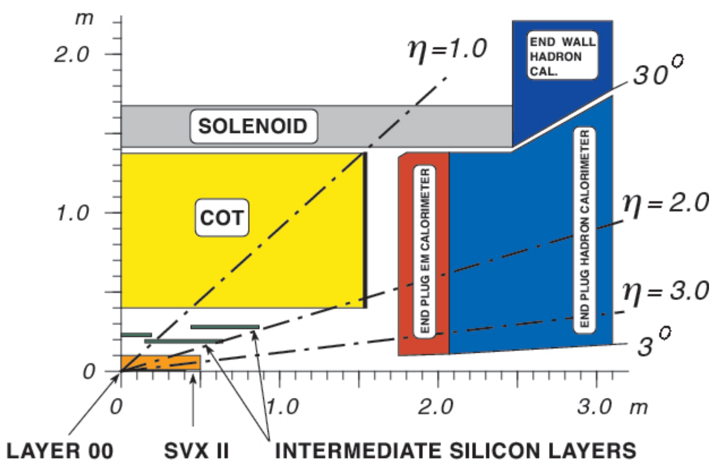

Figure 4.6: CDFII Tracking system. Longitudinal cross-sectional of the detector, showing the tracking system and the plug calorimeters.

Silicon detectors

The CDFII silicon detectors are designed to perform high precision tracking, which is very important for identifying long-lived particles, such as B hadrons. These B hadrons can travel several millimeters before decaying into many particles. The precise reconstruction of the charged particles allows the extrapolation of their trajectories to find a common decay origin (secondary vertex) that is well displaced from the location of proton-antiproton collision (primary vertex).
The CDFII silicon detectors are composed of silicon micro-strip sensors that can be divided into three sub-detectors (Figure 4.7). The core is the Silicon Vertex (SVXII), in the outer part there is the Intermediate Silicon Layers (ISL) while in the inner part there is the Layer 00. L00 is a light-weight silicon layer placed on the beam pipe. It recovers the degradation in resolution of the reconstructed vertex position due to the multiple scattering on the SVXII read-out electronics and cooling system, installed within the tracking volume.
Micro-strip allows precise measurement and is based on the p-n junction that creates localized region where electric charges are formed by the passage of charged particles. The resolution is given by the distance d between the strip and it is around $d/12$.

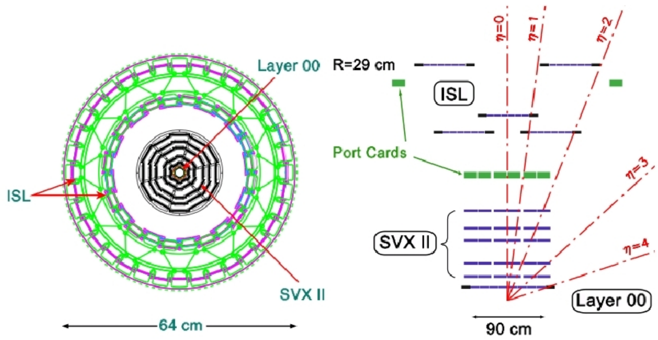

Figure 4.7: Silicon tracking sub-detectors projected in transversal and (r, z) plane.

L00

Starting from the center of the detector there is the L00[51] [52] that consists of a single castellated layer of single-sided, AC-coupled silicon sensors mounted directly on the beam pipe at radii, alternating in ϕ, of 1.35 cm or 1.62 cm from the beam. It provides full azimuthal and $|z| \leq 47\ cm$ longitudinal coverage. The strips are parallel to the beam axis allowing sampling of tracks in the (r, ϕ) plane.

Silicon Vertex detector II

The SVXII (Figure 4.8) [53] is a fine resolution silicon micro-strip vertex detector which provides five three-dimensional sampling of tracks at 2.45, 4.1, 6.5, 8.2 and 10.1 cm of radial

distance from the beam with full pseudo-rapidity coverage in the $|\eta_{det}| \leq 2$ region. It has a cylindrical geometry coaxial with the beam, and its mechanical layout is segmented in three axial sections of 32 cm, called barrels. Moreover each radial layer is divided in twelve 30° parts, called wedges.
Sensors in a single layer are arranged into independent longitudinal read-out units, called ladders. Each ladder comprises two, double-sided sensors and a multi-layer electronic board, all attached on a carbon-fiber support.
The active surface consists of double-sided, AC-coupled silicon sensors with micro-strips implanted on a 300 μm thick, high resistivity bulk. On one side, all sensors have axial strips spaced approximately 60-65 μm, for a precise reconstruction of θ coordinate. On the reverse side, the following combination of read-out pitch is used: 141 μm (90°), 125.5 μm (90°), 60 μm (1.2°), 141 μm (90°), 65 μm (−1.2°) from the innermost to the outermost layer for reconstructing the z-coordinate. The complete features of each layer are summarized in Table 4.2.

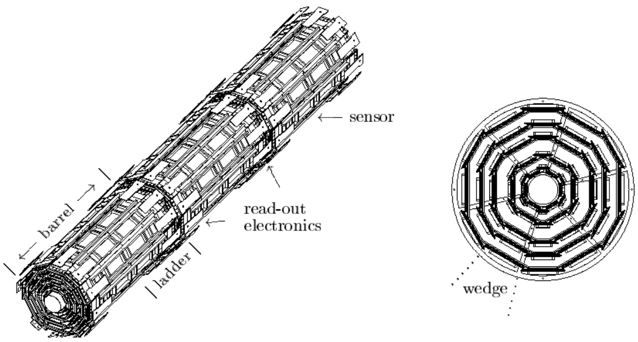

Figure 4.8: Schematic illustration of the three instrumented mechanical barrels of SVXII detector and, on the right, of the cross-section of a SVXII barrel in the (r, ϕ) plane.

Intermediate Silicon Layer

The ISL (Figure 4.9) [54] is a silicon tracker placed at intermediate radial distance between the SVXII and the drift chamber. At $|\eta_{det}| \leq 1$ a single layer of silicon sensors is mounted on a cylindrical barrel at radius of 22.6 cm. At $1 \leq |\eta| \leq 2.0$ two layers of silicon sensors are arranged into two pairs of concentric barrels (inner and outer). In the inner (outer) barrel, staggered ladders alternate at radii of 19.7 and 20.2 cm (28.6 and 29.0 cm). One pair of barrels is installed in the forward region, the other one is in the backward region. Each barrel is azimuthally divided into a 30° structure matching the SVXII segmentation. Each sensor has axial strip space by 112 μm on one side and 1.2° angled strip spaced 112-146 μm on the reverse.

Propriety	Layer 0	Layer 1	Layer 2	Layer 3	Layer 4
number of strip ϕ	256	384	640	768	896
number of strip Z	256	576	640	512	896
number of ϕ chip	2	3	5	6	7
number of Z chip	2	3	5	4	7
stereo angle	$90°$	$90°$	$1.2°$	$90°$	$-1.2°$
pitch ϕ strip (μm)	60	62	60	60	65
z pitch strip (μm)	141	125.5	60	141	65
total arm length (mm)	17.140	25.594	40.300	47.860	60.170
total long extension (mm)	74.3	74.3	74.3	74.3	74.3
active length (mm)	15.300	23.746	38.340	46.020	58.175
active longitudinal extension (mm)	72.43	72.3	72.38	72.43	73.43
number of detectors	144	144	144	144	144

Table 4.2: Characteristics of SVX II layers

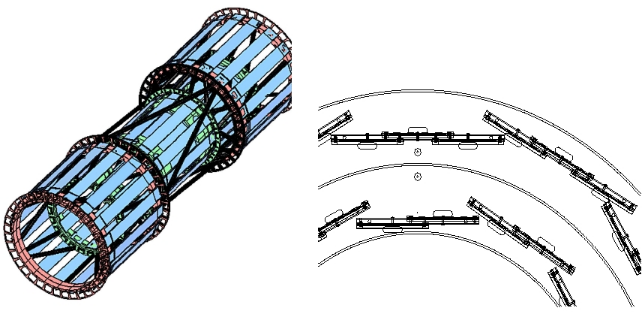

Figure 4.9: Intermediate Silicon Layer cartoon

Thanks to these three silicon sub-detectors an excellent identification of secondary vertexes is possible with a $\sim 40\ \mu m$ resolution on the impact parameter.

4.2.3 Central Outer tracker

The Central Outer Tracker (COT) [55], in Figure 4.10, is a cylindrical drift chamber located outside the silicon detectors at a radius from 40 cm to 137 cm and covers $|\eta_{det}| \leq 2$. It consists of 8 super-layers: 4 parallel to the beam-line (axial super-layers) and 4 with an angle $\pm 2°$ with respect to the z axis (stereo). Each super-layer is made of varying number of cells (for instance super-layer 1 has 169 cells and super-layer 8 has 480 cells). Each cell consists of a field sheet and a wire plane with alternating sense wires and field wires. The chamber is filled with a 50:50 mixture of Argon and Ethan gas that provides a constant electron drift velocity across the cells. As the COT is immersed in a magnetic field, the electrons drift at a Lorentz angle of 35°. Super-cells are tilted by 35° with respect to the radial direction to compensate this effect.
Charged particle passing through the COT interact and ionize the gas mixture. Positively charged ions and free electrons are created. If an electric field is applied in the gas volume, electrons will drift toward the anode. In the high field region near the anode, the electron ionizes other atoms and produces an avalanche, which creates a large signal on the wire. Electrons, so created, are collected on the anode wire giving an indication of the passage of a particle near that volume. Electrons drift faster than ions due to their lower mass. The electron drift velocity depends on the electric field gradient and on the properties of the gas molecules, which for the COT is $\sim 50 \mu m/s$. Usually signals deposited by a particle are collected in less than 200 ns.
COT is useful in measuring the momentum of the charged particles. Since the COT is placed in the 1.4 T magnetic field, charged particles travel in a helix with a radius $r = \frac{p_T}{|q|B}$ where p_T is the transverse momentum, q the particle charge and B the magnetic field. By reconstructing the track's curvature in the $r - \phi$ plane, $\mathrm{p_T}$ can be determined.
The technical properties of the tracker sub-detectors are summarized in Table 4.3.

4.2.4 Track reconstruction

The arc of the helix, in Figure 4.11, described by a q charged particle in the magnetic volume of CDFII is parameterized using the following five variables: three are transverse and the other two are longitudinal.

C - signed helix half-curvature, defined as $C = \frac{q}{2R}$, where R is the radius of the helix. This is directly related to the transverse momentum: $p_T = \frac{qB}{2|C|}$;

φ_0 - ϕ direction of the particle at the point of closest approach to the z-axis;

Layer 00	
r	from 1.35 to 1.65 cm
resolution	6 μm (axial)
number of channels	13824
SVX II	
r	from 2.4 a 10.7 cm
number of *layer*	5
read-out coordinates	r-ϕ one side for *layer*
other coordinates	r-z, r-z, r-uv, r-z, r-uv (uv=1.2°)
pitch resolution	60-65 μm $r-\phi$, 60-150 μm stereo
resolution	12 μm (axial)
total length	96.0 cm
rapidity	$\|\eta\| \leq 2.0$
number of channels	405 504
ISL	
r	from 20 to 28 cm
number of *layer*	one for $\|\eta\| \leq 1$, two for $1 \leq \|\eta\| < 2$
read-out coordinates	r-ϕ and r - uv (1.2° stereo) for all *layer*
pitch resolution	10 μm (axial), 146 μm (stereo)
resolution	16 μm (axial)
total length	174 cm
rapidity	$\|\eta\| \leq 1.9$
number of channels	268 800
COT	
r	from 44 to 132 cm
Number *super-layers*	8
Cells for *super-layer*	12
read-out Coordinates	+20°,-20°, +20°,+20°
drift distance	0.88 cm
resolution	180 μm
rapidity	$\|\eta\| \leq 2.0$
number of channels	30340

Table 4.3: Summary of the technical details of the tracker sub-detectors.

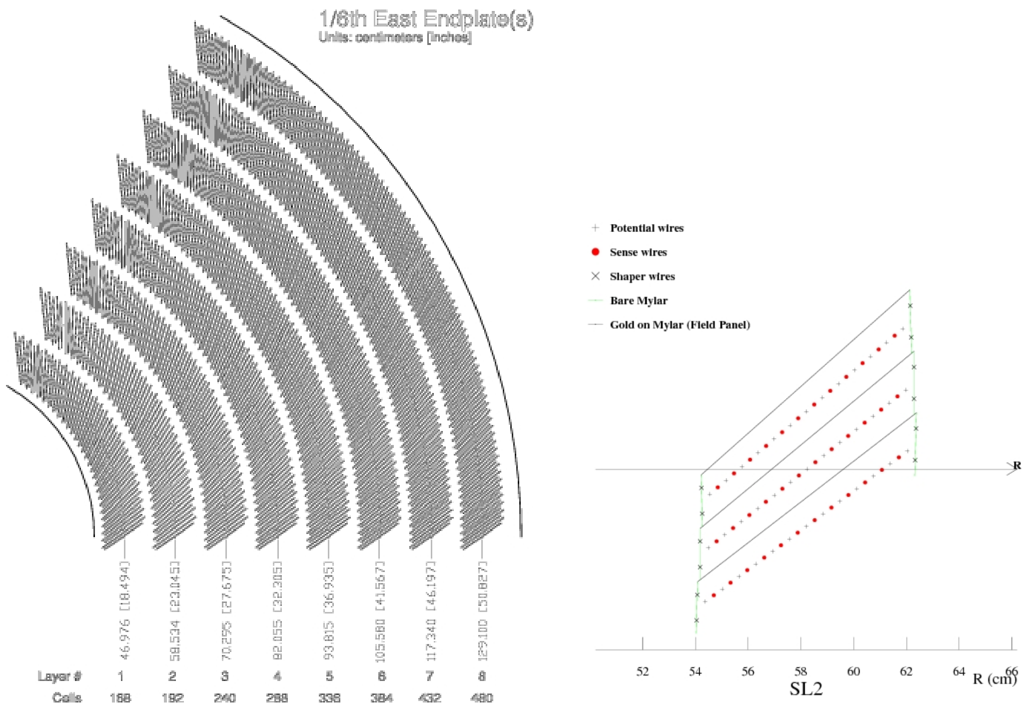

Figure 4.10: On the right: 1/6 of the COT end-plate. On the left: sketch of a axial cross-section of three cells in super-layer 3. The arrow shows the radial direction.

d_0 - signed impact parameter, i.e. the distance of the closest approach to the z-axis, defined as $d_0 = q(\sqrt{x_c^2 + y_c^2} - R)$, where (x_c, y_c) are the coordinates of the center-guide;

λ - the helix pitch, i.e. $\cot(\theta)$, where θ is the polar direction of the particle at the point of its closest approach to the z-axis. This is directly related to the longitudinal component of the momentum: $p_z = p_T \cot\theta$;

z_0 - the z coordinate of the point of the closest approach to the z-axis

The reconstruction of a charged particle trajectory consists in determining the above parameters through an helical fit of a set of spatial measurements (hits) reconstructed in the tracking detectors by clustering and pattern-recognition algorithms. The helical fit takes into account field non-uniformities and scattering in the detector materials.
The COT efficiency for tracks is typically 99 % and the single hit resolution is 140 μm. The typical resolutions of track parameters are the following: $\sigma_{p_T}/p_T^2 \sim 0.0015\ (GeV/c)^{-1}$, $\sigma_{\phi_0} \sim 0.035°$, $\sigma_{d_0} \sim 250\ \mu m$, $\sigma_{z_0} \sim 0.3\ cm$. [56]. Including the silicon information improves the impact parameter resolution of tracks which, depending on the number of the silicon hits, may reach 20 μm. This value combined with the $\sigma_T \sim 30\ \mu m$ transverse beam size is sufficiently small with respect to the typical transverse decay length of heavy flavors to allow the separation of their decay vertexes from production vertexes. The silicon tracker

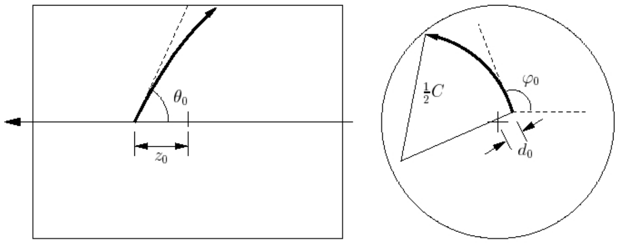

Figure 4.11: Track Reconstruction coordinates.

improves also the stereo resolutions up to $\sigma_{z_0} \sim 70\ \mu m$, while the transverse momentum and azimuthal resolutions remain approximately the same as COT only tracks. [57]
The comparison between resolutions of tracks reconstructed with only COT informations and with silicon+COT is shown in Table 4.4.

Parameter	COT	COT+SVX II+ISL
$\sigma p_T/p_T^2$ $[(GeV/c)^{-1}]$	0.0015	10^{-3}
σd $[\mu m]$	250	20
σz_0 $[\mu m]$	300	70
$\sigma cot\theta$	0.17°	0.06°

Table 4.4: *Track resolutions using COT only or Silicon information plus COT.*

4.2.5 Time of Flight detector

Between the COT and the super-conducting solenoid there is a time-of-flight detector (TOF) [58], locate at $r \sim 140$ cm from the beamline. It is a cylindrical array made of 216 scintillating bars of almost 3 m of longitude and located at $r \sim 140\ cm$. Both longitudinal sides of the bars collect the light pulse into a photo-multiplier and measure accurately the timing of the two pulses. The time between the bunch crossing and the scintillation signal in these bars defines the β of the charged particle while the momentum is provided by the tracking system. Particle identification (PID) information is available through the combination of TOF information and tracking measurements. The measured mean time resolution is 110 ps. This guarantees a separation between charged pions and kaons with $\mathrm{p_T} \leq 1.6\ GeV/c$ equivalent to 2 σ, assuming Gaussian distributions. Unfortunately, in high luminosity conditions ($\mathscr{L} \geq 5 \times 10^{31}\ cm^{-2}s^{-1}$) the occupancy of the single bars determines a degradation in efficiency, which is about 60 % per track.

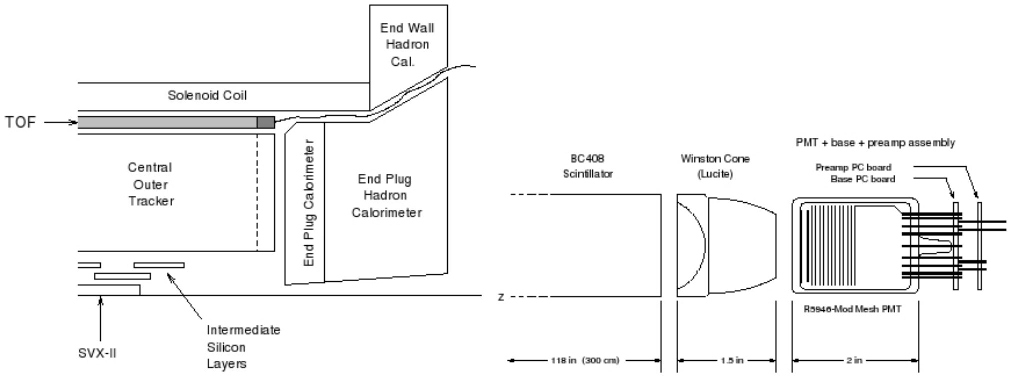

Figure 4.12: On the right view of the Time of Flight. On the left particular of the link between scintillator and photo-multiplier.

4.2.6 Calorimeters

Outside the solenoid, a scintillator-based calorimetry covers the region $|\eta_{det}| \leq 3.6$. It is devoted to the measurement of the energy deposition of electrons, photons and hadrons using the shower sampling technique.
The basic structure consists in alternating layers of passive absorbers and a plastic scintillator. Neutral particles and charged particles with a $p_T \geq 350\ MeV/c$ are likely to escape the solenoid's magnetic field and penetrate into the CDFII calorimeters. These are finely segmented in solid angle around the nominal collision point, and segmented radially outward from the collision point (in-depth segmentation). Angular segmentation is organized in projective towers. Each tower has a truncated-pyramidal architecture having the imaginary vertex pointing to the nominal interaction point. The base is a rectangular cell in the (η_{det}, ϕ) space. Radial segmentation of each tower instead consists of two compartments, the inner (closer to the beam) devoted to the measurement of the electromagnetic component of the shower, and the outer devoted to the measurement of the hadronic fraction of the energy. These two components are read independently through separated electronics channels.
A different fraction of energy released in the two compartments distinguished photons and electrons from hadronic particles. In total CDFII calorimetry consists of 1536 calorimeter towers. The light produced by the particles of the shower that cross the scintillating plate is collected by wavelength shifting (WLS) fibers that transport it to photo-multiplier tubes (PMT) located in the outermost part of the calorimeters. Every projective tower is read by one or two PMTs.
The sub-detectors that constitute the calorimeter of CDFII, are separated by the position with respect to the interaction point in two main groups: the central calorimeters, that approximately cover the region $|\eta_{det}| \leq 1.1$, and the plug calorimeters, that cover $1.1 \leq |\eta_{det}| \leq 3.6$. The central calorimeters consist of two separated halves that meet at $\eta_{det} = 0$. Due to this peculiar configuration, two gaps region exist around $\eta = 0$ an $\eta = 1.1$. Figure 4.13 shows the spacial disposition of the calorimeter and Table 4.5 lists the main characteristics of each calorimeter sub-detector.

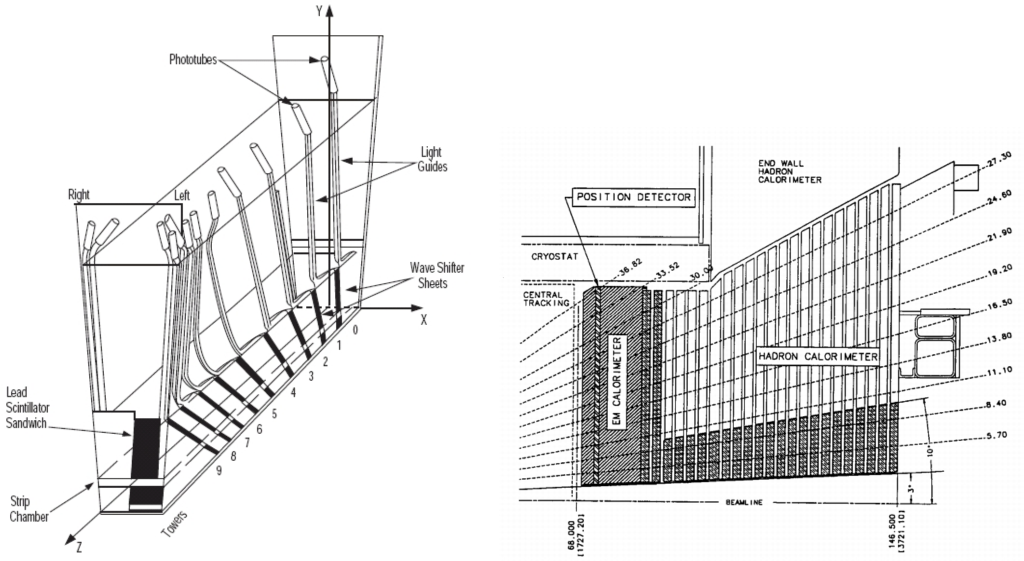

Figure 4.13: Schematic illustration of an azimuthal sector of the central electromagnetic calorimeter. On the left, elevation view of one quarter of the plug calorimeter.

	Coverage	segmentation (η)	Thickness	Resolution (E in GeV)
CEM	$\|\eta\| \leq 1.1$	0.1 $\times$ 0.26	18 X_0, λ_I	14 $\%/\sqrt{E_T} \bigoplus 2\%$
CHA	$\|\eta\| \leq 0.9$	0.1 $\times$ 0.26	4.7 λ_I	50 $\%/\sqrt{E_T} \bigoplus 3\%$
WHA	$0.9 \leq \|\eta\| \leq 1.3$	0.1 $\times$ 0.26	4.7 λ_I	75 $\%/\sqrt{E_T} \bigoplus 4\%$
PEM	$1.1 \leq \|\eta\| \leq 3.6$	(0.1-0.6) $\times$ (0.13-0.26)	23 X_0,4.7 λ_I	16 $\%/\sqrt{E_T} \bigoplus 1\%$
PHA	$1.2 \leq \|\eta\| \leq 3.6$	(0.1-0.6) $\times$ (0.13-0.26)	6.8 λ_I	80 $\%/\sqrt{E_T} \bigoplus 5\%$

Table 4.5: The CDF II calorimeters with their acronym, η region, segmentation, thickness and energy resolution. X_0 represents the shower length and λ_I is the pion nuclear absorption length in $g\ cm^{-2}$

Central region: CEM, CHA, WHA

The radial extension of the calorimeters in the central region is 1.73 m $\leq r \leq 3.5\ m$. The Central ElectroMagnetic Calorimeter (CEM) [59] [60] is constructed as four azimuthal arches (NE, NW, SE,SW), each of which subtends 180° and is divided into twelve 15° wedges. A wedge consists of 31 layers of 5 mm thick polystyrene scintillators interlayed with 30 aluminum-clad lead 3.2 mm thick sheets. It is divided along η_{det} into 10 towers. To maintain a constant thickness in X_0 (radiation length) and compensate the sin(θ) variation between towers, the same lead layers are replaced with increasing amounts of acrylic as a function of η_{det}. The spacial resolution of the CEM is about 2 mm. At a radial depth of 5.9 X_0, which is approximately the depth corresponding to the peak of shower development, the CEntral Strip multi-wire

proportional chamber (CES) measures the transverse shower shape with 1.5 cm segmentation. A further set of multi-wire proportional chambers, the Central Pre-Radiator(CPR) [61] is located in the gap between the outer surface of the solenoid and the CEM. It monitors photon conversions started before the first CEM layer. Phototube gains are calibrated once per store using an automated system of Xenon or LED light flashers.
The hadronic compartment is the combination of two sub-systems: the Central HAdronic (CHA) and the Wall HAdronic (WHA) [62] calorimeters. Each CHA wedge is segmented into 9 η_{det} towers matching in size and position the CEM towers. The WHA wedge instead consists of 6 towers of which three are matching CHA towers. Radially a CHA tower is constructed of 32 layers of 2.5 thick steel absorber alternating with 1.0 cm thick acrylic scintillator. WHA tower structure is similar but there are only 15 layers of 5.1 cm thick absorber.
The total thickness of the electromagnetic section corresponds to approximately 18 X_0 (1 λ_I, where λ_I is the pion nuclear absorption length in units of g cm^{-2}), for a relative energy resolution $\sigma_E/E = 14\%/\sqrt{E_T} \bigoplus 2\%$[2]

Forward region: PEM and PHA

The coverage of the $1.1 \leq |\eta| \leq 3.6$ region relies on the scintillating tile Plug calorimeter [63] which is composed of two identical devices, one installed in $\eta_{det} \geq 0$ and the other in the $\eta_{det} \leq 0$. Each of these two halves has electromagnetic and hadronic compartments.
In each half, the absorber of the Plug ElectroMagnetic calorimeter (PEM) consists of 23 doughnuts - shaped lead plates, 2.77 m in outer diameter, which have a central hole where the beam pipe is located. Each plate is made out of 4.5 mm thick calcium-tin-lead sandwiched between two 0.5 mm thick stainless-steel sheets. Between the absorber plates are inserted the 4 mm thick scintillator tiles organized azimuthally in 15° triangularly-shaped wedges. A Pre-shower detector consists of a thicker (10 mm) amount of scintillator installed in the first layer of PEM, while shower maximum sampling is performed at radial depth of $\approx 6X_0$ by two tilted layers of scintillator strips (pitch 5 mm).
Each half of the hadronic compartment, Plug HAdronic calorimeter (PHA), is azimuthally divided in 12 wedge-shaped modules each subtending 30°. In depth each module consists of 23 layers of 5 cm thick iron absorber alternated with 6 mm scintillator layers. Within each sampling layer the scintillator is arranged in tiles similar to those used in the PEM.
The total thickness of the electromagnetic section corresponds to approximately 23 X_0 (4.7 λ_I), for an energy resolution of $\sigma_E/E = 16\%/\sqrt{E_T} \bigoplus 1\%$. The total thickness of the hadronic section corresponds to approximately 8 λ_I, for an energy resolution of $\sigma_E/E = 75\%/\sqrt{E_T} \bigoplus 4\%$.

[2] The first term is called the stochastic term and derives from the intrinsic fluctuations of the shower sampling process and of the PMT photo-multiplier yield. The second term, added in quadrature, depends on the calorimeter non-uniformities ad in the uncertainty on the calibration. All energies are in GeV .

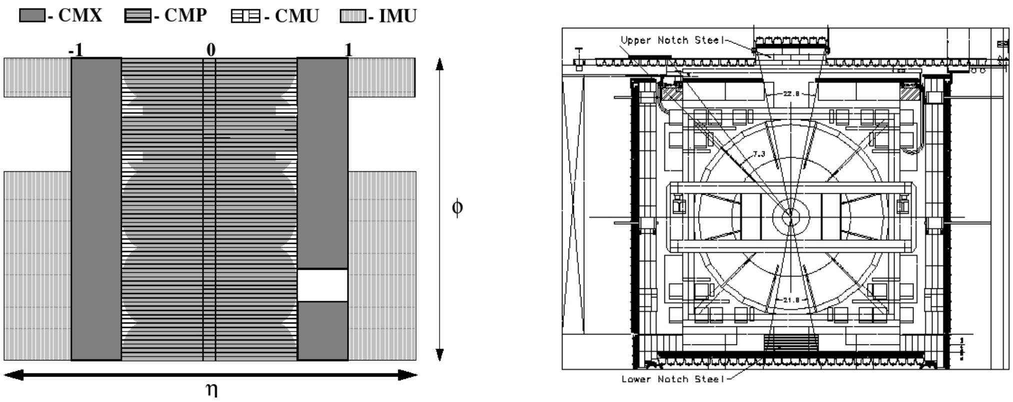

Figure 4.14: Muon sub-detectors

4.2.7 Muons systems

Muon system in Figure 4.14 is placed in the most outer part of the detector. This consists of scintillating counters and drift tubes installed at various radial distances from the beam to detect muons [64] . Scintillators serve as a trigger and vetoes while the drift chambers measure the ϕ coordinate using the absolute difference of the drift electrons arrival time between 2 cells and the z coordinate by charge division.
These sub-detectors cover the whole range of pseudo-rapidity $|\eta_{det}| \leq 2$ and are used only to identify the penetrating muon reconstructing a small segment of their path (stub) sampled by the chambers. The moment measurement is performed by pointing back the stub to the corresponding track in COT.
Different muon sub-systems cover different geometrical regions. In the $|\eta_{det}| \leq 0.6$ region moving outward from the beam we encounter the inner Central MUon detector (CMU) chambers at radial distance of 3.5 m. Approximately 5.4 λ_I of material separate the luminous region from CMU resulting in about 1/220 high energy hadrons passing through the calorimeter and reaching the muon detector. This defines also a $\mathrm{p_T}$ threshold for muons reaching the CMU which is approximately 1.4 GeV/c. In order to recognize and discard them, the Central Muon uPgrade (CMP) chambers lie in the same η_{det} region separated radially from the CMU by a 60 cm thick wall of steel achieving a rejection of 95 % of the fake muons.
The muon coverage in the $0.6 \leq |\eta_{det}| \leq 1.0$ volume is ensured by the Central Muon eXtension (CMX) chambers, embedded in scintillator counters and placed at radius of 3.5 m. The Intermediate MUon detectors (IMU) are instead drift tubes covering the pseudo-rapidity range $1.0 \leq |\eta_{det}| \leq 2.0$. CDFII triggers on muons only emerging at $|\eta_{det}| \leq 1.5$ where the muon coverage is segmented with sufficient granularity to survive high occupancies. The granularity of muon devices in the forward regions is less fine and not adequate for triggering, but sufficient for off-line muon assignment to high $\mathrm{p_T}$ tracks going through that region.

4.2.8 The Cherenkov Luminosity counters

The luminosity ($\mathscr{L}$) is inferred from the average number of inelastic interactions per bunch crossing ($\bar{N}$) according to :

$$\bar{N} \times f_{b.c.} = \sigma_{p\bar{p}-in} \times \epsilon \times \mathscr{L}$$

where the bunch-crossing frequency ($f_{b.c.}$) is precisely known from the Tevatron RF, $\sigma_{p\bar{p}-in} = 60.7 \pm 2.4\ mb$ is the $p\bar{p}$ cross-section resulting from the average CDFII and E811 luminosity independent measurement at $\sqrt{s} = 1.8\ TeV$, and extrapolated to $\sqrt{s} = 1.96$ TeV. ϵ is the efficiency for detecting an inelastic scattering [65].
The Cherenkov luminosity Counters (CLC) are two separate modules, covering the $3.7 \leq |\eta_{det}| \leq 4.7$ range symmetrically in the forward and backward regions. Each module consists of 48 thin, 110-180 cm long, conical, ISO-butene-filled Cherenkov counters. They are arranged around the beam-pipe in three concentric layers and pointed to the nominal interaction region. The base of each cone, 6-8 cm in diameter and located at the furthest extremity from the interaction region, contains a canonical mirror that collects the light into a PMT, partially shielded from the solenoidal magnetic field. ISO-butane guarantees high refraction index and good transparency for ultraviolet photons. With a Cherenkov angle $\theta_C = 3.4°$ the momentum thresholds for light emission are 9.3 MeV/c for electrons and 2.6 MeV/c for charged pions. Prompt charged particles from the $p\bar{p}$ interactions are likely to transverse the full counter length, thus generating large signals and allowing discrimination from the smaller signals of angled particles due to the beam halo or to secondary interactions. In addition, the signal amplitude distribution shows distinct peaks for different particle multiplicities entering the counters. This allows a measurement of $\bar{N}$ with 4.2 % relative uncertainty in the luminosity range $10^{31} \leq \mathscr{L} \leq 10^{32} cm^{-2}s^{-1}$. This accuracy, combined with the 4 % relative uncertainty on the inelastic $p\bar{p}$ cross section, results in an instantaneous luminosity measurement with 5.8 % relative uncertainty.

4.3 Trigger and data acquisition system

Tevatron produced almost 1.7 millions collisions between bunches of proton and antiproton every second. Each collision recorded by CDFII is called event and dead-time is the percentage of events which are rejected because the trigger is busy during the acquisition of an event (due to the read-out of the entire detector that takes approximately 2 ms).
The most interesting processes constitute only a minimal fraction of the total events. For this reason a system is necessary to discriminate the events during their acquisition. This is the task of the trigger system, which evaluates the partial information provided by the detector and discards the uninteresting events on-line.
The CDFII trigger is a three-level system that selectively reduces the acquisition rate with virtually no dead-time, i.e. keeping each event in the trigger memory a time sufficient to allow for a trigger decision without inhibiting acquisition of the following events. Each level receives the accepted event from the previous one and, provided with detector information of increasing complexity and with more time for proceeding, applies a logical OR of several sets of programmable selection criteria to make its decision.

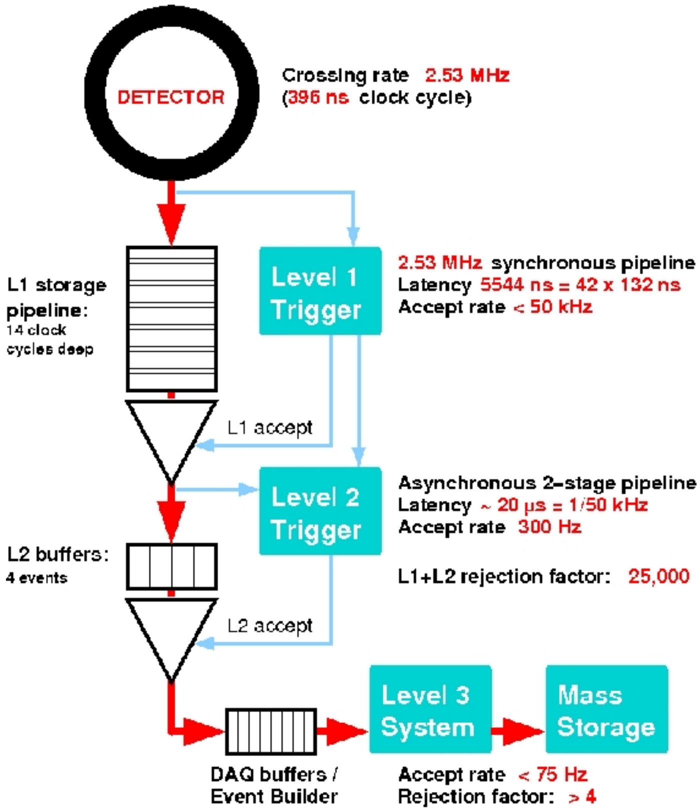

Figure 4.15: CDFII trigger system

4.3.1 Level 1

At Level-1 (L1), a buffered synchronous system of custom-designed hardware processes a simplified subset of data in three parallel streams to reconstruct information from the calorimeters (total energy and presence of single towers over threshold), the COT (two dimensional tracks in transverse plane) and the muon system (muon stubs in the CMX, CMU and CMP chambers). A decision stage combines the information from these low resolution physics objects, called primitives, into more sophisticated objects. For instance, track primitives are matched with muon stubs or tower primitives to form muon, electron or jet objects, which then undergo some basic selections. This trigger can decide if to record the event in 5.5 μs. In such a way it is able to reduce the rate of potentially interesting events to 30 kHz.
The fundamental processor in this passage is the eXtremely Fast Tracker (XFT) [66] that identifies two dimensional tracks in the (r, ϕ) view of the COT (transverse plan) in time with L-1 decision.

4.3.2 Level-2

Level-2 is an asynchronous system of custom designed hardware that processes the time ordered events accepted by the Level-1. Additional information from the shower-maximum

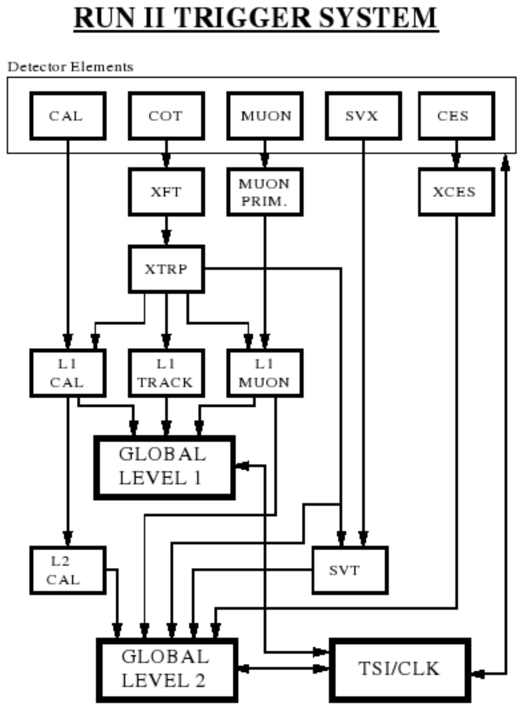

Figure 4.16: CDFII trigger block diagram.

strip chambers in the central calorimeter and the axial hits in the SVXII is combined with Level-1 primitives to produce Level-2 primitives. A energy-clustering is done in the calorimeter by merging the energies in adjacent towers to the energy of a seed tower above threshold. Level-1 track primitives, matched with consistent shower maximum clusters, provide refined electron candidates whose azimuthal position is known with 2° accuracy. Information from the (r, ϕ) sides of the SVXII is combined with Level-1 tracks primitives to form two dimensional tracks with resolution similar to the offline one. Finally, an array of programmable processors makes the trigger decision, while the Level-2 objects relative to the following event accepted at Level 1 are already being reconstructed.
One important task at L-2 is performed by the Silicon Vertex Trigger.

Silicon Vertex Trigger

Reconstructing decay vertexes on-line is technically challenging and requires constrained geometrical fitting of high-resolution tracks at high events rates. The Silicon Vertex Trigger (SVT) [67] computes instead the impact parameters of the charged particles, which is faster than fully reconstructing their decay vertexes, but still provides information on the lifetimes of the decaying particle. The full spatial resolution of silicon detectors is needed to discriminate O(100 μm) impact parameters from the O(10 μm) beam spot. Thus the SVT requires the coincidence of hits in four axial SVXII layers with a XFT track. Since silicon signals are digitized only after the Level 1 accept decision, the SVT is used at Level-2, whose average

latency is around 20 μs. Within this time, the SVT reconstructs two dimensional tracks in the bending plane of the spectrometer with off-line resolution. The SVT speed is largely due to its high-parallelized structure and to the implementation of novel techniques both in pattern recognition and in track fitting.
The output of the SVT are the reconstructed parameters of the two dimensional track in the transverse plane: ϕ_0, $\mathrm{p_T}$ and the impact parameter d_0. The list of parameters for all found tracks is sent to Level-2 for trigger decision.
The SVT measures the impact parameter with a standard deviation of $\approx 35\mu m$ and a average latency of 24 μs, 9 of which spent waiting for the start of the read-out of silicon data.

4.3.3 Level 3

The digitalized output relative to the Level-2 accepted event reaches Level-3 via optical fibers and it is fragmented in all sub-detectors. It is collected by a custom hardware switch that arranges it in the proper order and transfers it to commercial computers. The ordered fragments are assembled in the event records, a block of data that univocally corresponds to a bunch crossing and it is ready for the analysis of the Level 3 software [68]. The event reconstruction benefits from full detector information and improved resolution with respect to the proceeding trigger levels, including three-dimensional track reconstruction, tight matching between tracks and calorimeter or muon information. If an event satisfies the Level-3 requirements, the corresponding event record is transferred to mass storage at a maximum rate of $\sim$ 100 kHz. A fraction of the output is monitored in real time to search for detector malfunctions, to derive calibrations constants and to graphically display events. The Level-3 decision is made after the full reconstruction of an event is completed and the integrity of its data is checked.

4.3.4 Operation and data quality

During the data taking there are several procedures to check the data quality and the complete operativeness of the all sub-detectors.
Each time that at least one of the trigger path fires, an event is labeled with a progressive number. Events are grouped into runs, i.e. periods of continuous data taking in constant configurations of trigger table, set of active sub-detectors and so on. Several parameters of the operation are stored in the database on a run-averaged format.
All data manipulation occurring some time after the data are written to permanent memories are referred to as off-line processes, as opposed to the online operations that take place in real time, during the data-taking. The most important offline operation is the processing with a centralized production analysis that generated collections of high-level physics objects suitable for analysis, such as tracks, vertexes, muons, electrons and jets from low level information such as hits in the tracking sub-detectors, muon stubs and fired calorimeter towers. During the production, more precise informations about the detector conditions and more sophisticated algorithms are used than those ones available at the Level-3 of the trigger.

To ensure homogeneous data-taking conditions, each run undergoes a quality inspection.

One line shift operators, offline production operators, and sub-detector experts certify in what fraction of data the running conditions for all relevant sub-detectors are compliant to physics quality standards.

5 Physics Objects Reconstruction

Events passing trigger requirements are reconstructed offline in a process during which collections of high-level physics objects are generated. This chapter presents the standard CDF algorithms to reconstruct objects, such as electrons, muons and jets. Particular attention is given to the secondary vertex finder algorithm utilized to identify jets originated from $b-$quarks.

5.1 Primary Vertex

5.1.1 z primary vertex

The $z-$coordinate of the primary vertex is reconstructed using an algorithm called *ZVertexFinder*. This combines all the track information of an event and it is based on an iterative procedure. The reconstruction starts determining the zero approximation vertex coordinate z_V from the median of the z_{0i} track coordinates of a given track collection. After that a χ^2 is calculated as:

$$\chi^2 = \sum_{i=1}^{N_T} \frac{(z_V - z_{0i})^2}{\sigma_i^2} \tag{5.1}$$

where N_T is the number of tracks and σ_i is the uncertainty of z_{0i}.
Tracks whose contributions of χ^2 is greater than 3 are excluded therefore the vertex coordinate is recalculated:

$$z_V = \frac{\sum_{i=1}^{N_T} \frac{z_{0i}}{\sigma_i^2}}{\sum_{i=1}^{N_T} \frac{1}{\sigma_i^2}} \tag{5.2}$$

This procedure is repeated until there is no track to exclude. The algorithm may return more than one vertex. In that case, the one with the highest $\sum p_T$ is selected, where the sum runs over the assigned tracks.

5.1.2 3-D Primary Vertex

A precise three dimensional vertex is fundamental to look for displaced secondary vertexes, as it will be discussed later.
The 3-D vertex reconstruction starts with an input seed defined by the $x - y$ positions of the

run average beam-line and from the z_V found with ZVertexFinder algorithm. The *PrimeVtx* selects good quality tracks that pass cuts in Table 5.1 and are compatible with the seed vertex. Using this tool a fit is performed to find a new primary vertex. At this point the algorithm starts removing tracks that contribute with the worst χ^2 (≥ 10) relative to the fit. The iterative process stops when there are not more tracks with $\chi^2 \geq 10$ in the vertex. The resolution of the primary vertex coordinates obtained depends on the number of tracks, and it is of the order of $\sim 50\ \mu m$.

$\lvert z_0 - z_{seed}\rvert$	≤ 1 cm
p_T	≥ 0.5 GeV/c
$\lvert d_0\rvert/\sigma_{d_0}$	≤ 3.0
Axial COT SL with at least 6 hits	≥ 2
Stereo COT SL with at least 6 hits	≥ 2
Silicon hits	≥ 3

Table 5.1: Track quality cuts for the primary vertex

5.2 Electrons

Electron candidates are reconstructed from the electromagnetic deposit in on or two calorimeter towers matched to clusters in the pre-shower and in the shower maximum detectors. When possible, it is also associated the maximum $\mathrm{p_T}$ track, among all the tracks pointing to the shower-max cluster.
The total energy of an electron is given by the sum of the hadronic and electromagnetic energy of all the towers in the cluster. The centroid and the respective E_T, η, ϕ are evaluated according the Snowmass principles:

$$\eta = \frac{E_{EM} \times \eta_{EM} + E_{Had} \times \eta_{Had}}{E}$$

$$\phi = \frac{E_{EM} \times \phi_{EM} + E_{Had} \times \phi_{Had}}{E}$$

where the angular variables are:

$$\eta_{EM} = \frac{\sum_i E^i_{EM} \times \eta^i}{\sum_i E^i_{EM}}$$

$$\eta_{had} = \frac{\sum_i E^i_{had} \times \eta^i}{\sum_i E^i_{Had}}$$

$$\phi_{EM} = \frac{\sum_i E^i_{EM} \times \phi^i}{\sum_i E^i_{EM}}$$

$$\phi_{had} = \frac{\sum_i E^i_{had} \times \phi^i}{\sum_i E^i_{Had}}$$

In order to identify electrons among the selected candidates, characteristic variables will be used in the analysis to discriminate electrons from fake signals. These are:

$E_T = E\sin\theta$: The transverse electromagnetic energy, E_T, is obtained from the energy of the EM cluster and the polar angle θ of the associated track.

$p_T = P\sin\theta$: The transverse momentum of the track associated with the electron. P is the momentum of the track.

E_{Had}/E_{EM}: The ratio between the hadronic and electromagnetic energy deposition in the calorimeter. This is particularly important to discriminate electrons from jets.

E/P: The ratio between the transverse energy of the EM cluster and the transverse momentum of the track. This ratio could be large if electrons radiate photons. For high energy electrons the value of the fraction is close to 1.

$\Delta x_{CES}Q$, Δz_{CES}: Distances between the extrapolated track and the best matching CES cluster respectively in the plane (r,ϕ) and (r,z). Δx_{CES} is usually multiplied for the track charge Q.

χ^2_{CES}: The χ^2 comparison of the CES shower profile with the shower profile obtained from the test beam measurement.

L_{shr}: This is a variable useful to discriminate electrons and photons from hadronic showers faking these particles in the central electromagnetic calorimeter. It compares the distribution of adjacent CEM tower energies in the cluster to shapes derived from test-beam, as function of the seed energy.

$Isol04$: The isolation is defined as:

$$Isol04 = \frac{E_T^{cone} - E_T^{electron}}{E_T^{electron}}$$

where $E_T^{electron}$ is the energy of the electron cluster and E_T^{cone} is the transverse energy in a cone of radius $\Delta R = \sqrt{(\Delta\eta)^2 + (\Delta\phi)^2} \leq 0.4$ around the electron cluster.

$\chi^2_{3\times3}$: The χ^2 comparison of the PEM shower profile with the shower profile obtained from the test beam measurement.

$PES\ U\ energy$: The energy for the U strip of the best matched cluster in PES

$PES\ V\ energy$: The energy for the V strip of the best matched cluster in PES

$\Delta R(PEM, PES)$: The difference between the PEM and PES coordinates of the electron cluster

N^{Si}_{hits}: The number of the silicon detector hits

N_{trk}: Number of tracks associated to the cluster

$Ene_{3\times3}$: Energy of 3×3 PEM cluster

5.3 Muons

Muons, as minimum ionizing particles, leave only residual energy in the calorimeters. They are identified by signals left in the tracking system and also by the stubs present in those detectors. Depending on the muon chamber where the stub is found, muons are classified as CMU, CMP and CMX muons.
The muon reconstruction begins from the information collected in drift chambers and scintillators of the muon sub-detectors, looking for a stub that links a few hits. This is obtained with an iterative fit of the hits and the criteria used depend on the particular muon detector. Tracks are then associated to the stubs. Only one track should be assigned for each stub. When more than one track is matched, tracks are sorted based on the quality of the fit extrapolation and the best track is assigned. For the candidates that passed this step, calorimeter information is added by extrapolating the track trajectory into the calorimeter. Tracks that remain without a stub are integrated with calorimeter information and are stored as a stub-less muon candidates (CMIO).
The main variables used in the analysis to identify muons are:

p_T, E_{EM}, E_{HAD}: The transverse momentum p_T of the best matched track associated to the muon, the EM (HAD) calorimeter energy corresponding to the muon

N_{SL}: Number of COT super-layers passed through by the track associated to the muon

z_0: The z-coordinate of the muon associated track at the distance of the closest approach to the beam-line

d_0: The impact parameter, that is the distance of the muon associated track to the primary vertex in the (r, ϕ) plane.

$Isol04$: The ratio between the energy deposited in the calorimeter towers within a cone ($\Delta R = 0.4$) and the muon track p_T

$\frac{\chi^2}{n.d.f}$: The reduced χ^2 for the stub-track association

N_{hits}^{Si}: The number of the silicon detector hits

N_{hits}^{COT}: The number of the COT detector hits

N_{SL}^{AX}: The number of axial COT SL with at least 5 hits

N_{SL}^{ST}: The number of stereo COT SL with at least 5 hits

5.4 Jets

As defined in Chapter 2, jets [69] consist of collimated spray of high-energy hadrons. The signature of jets are deposits of energy in electromagnetic and hadronic calorimeters. Their reconstruction starts from the physical towers in the calorimeter and depends on the jet algorithm used.

A physical tower is created from the detector tower using the following formulas:

$$p_x = E_{EM} \sin\theta_{EM} \cos\phi_{EM} + E_{HAD} \sin\theta_{HAd} \cos\phi_{HAD}$$
$$p_y = E_{EM} \sin\theta_{EM} \sin\phi_{EM} + E_{HAD} \sin\theta_{HAd} \sin\phi_{HAD}$$
$$p_z = E_{EM} \cos\theta_{EM} + E_{HAD} \cos\theta_{HAd}$$
$$E = E_{EM} + E_{HAD}$$

where E_{EM} (E_{HAD}) is the energy deposited in the electromagnetic (hadronic) compartment of the detector tower. θ_{EM} and ϕ_{EM} (θ_{HAD}, ϕ_{HAD}) represent the direction from the interaction point to the shower maximum position of an electromagnetic (hadronic) shower (Figure 5.1).

In this analysis we are using jets reconstructed with the Midpoint algorithm in a cone of radius $R = 0.7$.

5.4.1 The CDF MidPoint Jet clustering Algorithm

As explained in Chapter 2, the Midpoint is a seed based algorithm. The calorimetric towers with an energy greater than 100 MeV are selected and sorted in p_T. Towers belonging to identified electrons or muons are excluded from the towers available to reconstruct the jet. Starting from the highest $\mathrm{p_T}$ seed towers (with a momentum greater than 1 GeV/c), a protojet is created by adding adjacent towers within a cone of radius 0.7 in $\eta - \phi$ space. This is an iterative process, whenever a tower is added, a cluster centroid is recalculated, a new cone is drawn and the process continues until the protojet becomes stable[1]. The determination of the centroid is done in E-massive scheme that consists in adding the four-momenta. This makes the jet massive, contrary to the Snowmass scheme where the jets are considered massless.

After that, a list of midpoints is generated between protojets separated by less than twice the cone radius therefore new stable protojets are found around midpoints. Adding midpoint seeds between all stable cones reduces the sensitivity of the algorithm to soft radiation [25].

The protojets then pass to splitting/merging steps where the overlapping protojets are separated based on the percentage of $\mathrm{p_T}$ shared by the lower $\mathrm{p_T}$ protojet. Protojets that are sharing a fraction greater than 75 % will be merged, otherwise they will split and towers assigned to the closer cone.

What we have described is the detector level jet reconstruction. In this analysis we also use jets defined at hadron level in MC where four-vectors of the stable particles are the basic elements to be clustered. The reconstruction procedure follows the steps listed above.

5.4.2 Jet Corrections

Jets reconstructed at calorimeter level are affected by losses in the gaps, multiple interactions, instrumental effects and detector non linearity in addition to the extra energy added by multiple interactions. In order to match the corresponding particle energy, jets are corrected[70]

[1] This means that the process is iterated until the cone axis and the centroid coincide, indicating that the configuration results stable.

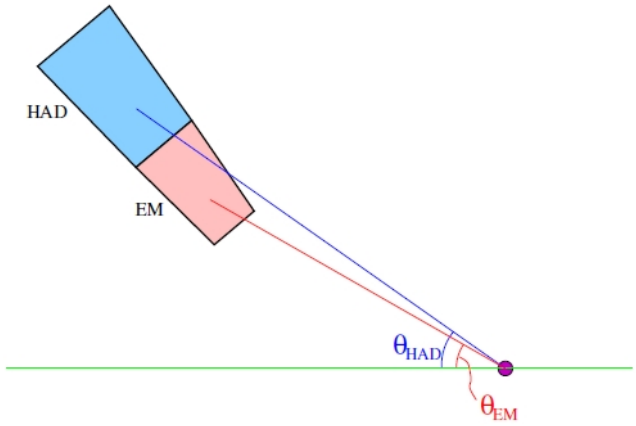

Figure 5.1: Scheme of a single calorimeter tower with electromagnetic (pink) and hadronic compartments. θ_{EM} and θ_{HAD} are the respective directions with respect the interaction point.

in the following way:

$$p_T^{particle} = (p_T^{jet} \times C_\eta - C_{MI}) \times C_{abs}$$

where p_T^{jet} is the transverse momentum of the jet and C_η, C_{MI}, C_{ABS} are the corrections due to the rapidity dependence of the calorimeter response, the multiple interactions and the absolute energy, which are described below.

Eta corrections

C_η, called relative corrections or L1, are performed to flatten the η dependence of the calorimeter response. These corrections are determined using the dijet balancing method which assumes the two jets to be balanced in p_T in absence of hard QCD radiations. A "trigger jet" is required to be in the central calorimeter and the other jet, called "probe jet", could be anywhere in η. The correction factors, defined as $\beta = \frac{p_T^{probe}}{p_T^{trigger}}$, are determined separately for data and MC for different $\mathrm{p_T}$ regions.
The systematic uncertainty is obtained by varying the event selection requirements and the fitting procedure. Plots of Figure 5.2 (5.3) show β as a function of rapidity and for different p_T regions before (after) the L1-corrections.

Multiple Interaction Corrections (C_{MI})

The multiple interaction corrections, or L4, subtract the energy coming from extra $p\bar{p}$ interactions taking place in the same bunch crossing, estimated by the number of reconstructed $z-$vertexes (N_{vtx}). These corrections are determined using a minimum bias data sample

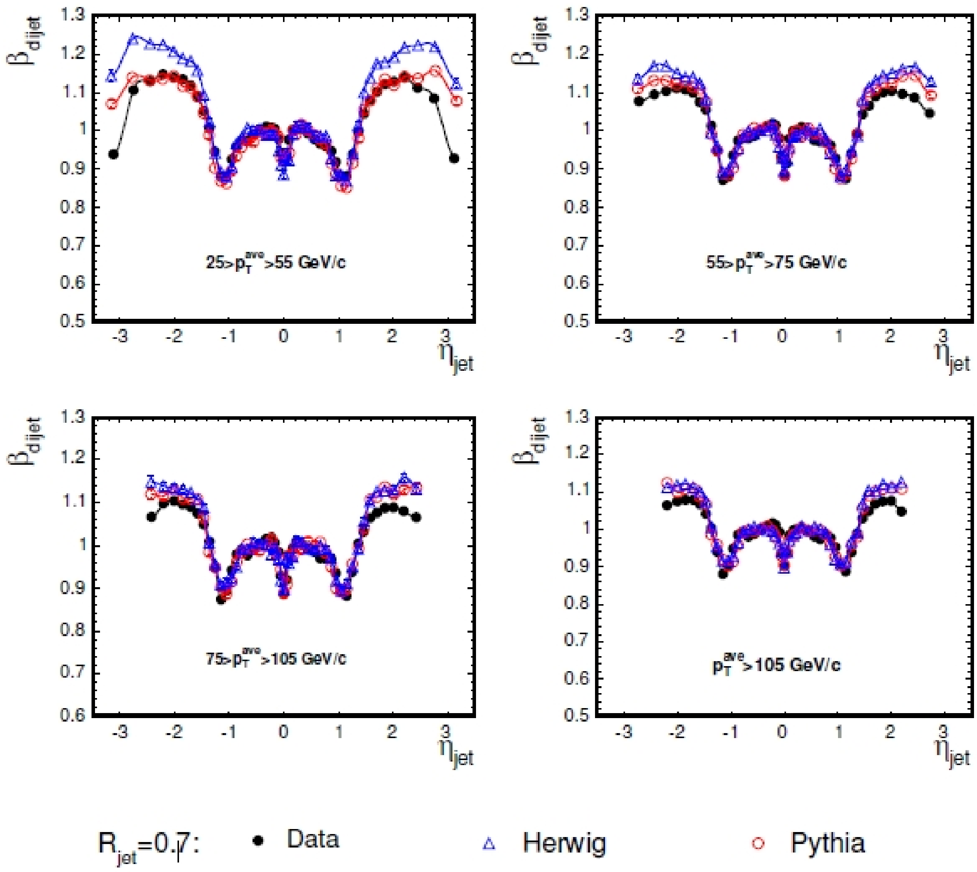

Figure 5.2: Dijet p_T balance as a function of η_{det} in data, HERWIG and PYTHIA MC samples for jets of cone size $R = 0.7$. Shown are the correction factor for several p_T regions. Figure taken from [70].

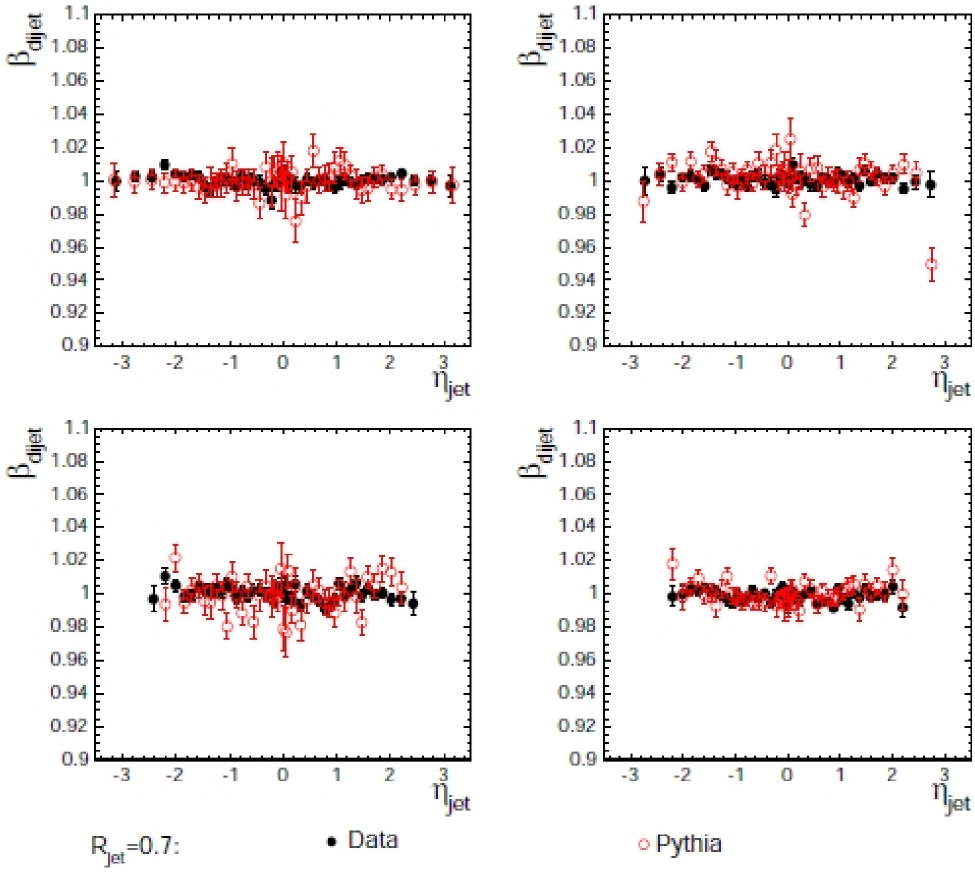

Figure 5.3: Dijet p_T balance as a function of η_{det} in data and PYTHIA MC samples for jets of cone size $R = 0.7$. Shown are the correction factor for several p_T regions after applying the L1-corrections. Figure taken from [70].

(collected requiring at least one $p\bar{p}$ interaction). The average transverse energy in a cone is measured in the central calorimeter as a function of the number of vertices for three cone sizes. Data are parameterized using a fitted straight line (Figure 5.4) where the slope parameters give the extra transverse energy per interaction as a function of N_{vtx}. The $\mathrm{p_T}$ is corrected according to this formula:

$$p_T^{'} = p_T - \epsilon(N_{vtx} - 1)$$

The systematic uncertainty from this correction is approximately 15 %. It is due to dependence on instantaneous luminosity and event topologies.

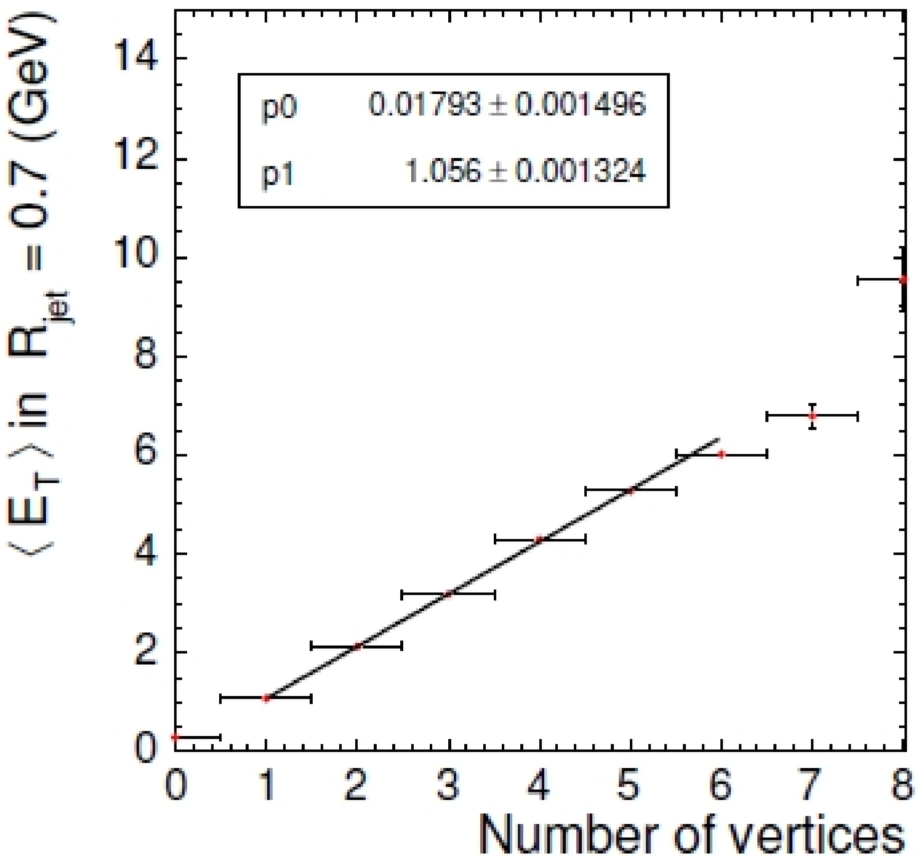

Figure 5.4: $< E_T >$ versus the number of vertexes for jets of cone size $R = 0.7$. A linear fit is also shown. Figure taken from [70]

Absolute Correction (C_{abs})

The absolute jet energy scale correction or L5 transforms the jet energy measured in the calorimeter into the corresponding to the particle jet so that the jet energy scale can be independent from the detector. This is done to compensate for non linearity and energy loss in the un-instrumental regions of the calorimeter. The correction is obtained in MC by mapping the total $\mathrm{p_T}$ of the particle level jet to the $\mathrm{p_T}$ of the calorimeter level jet. Jets reconstructed at calorimeter and particle level use CDF standard clustering, and they are required to be in a central region and to be one of the two leading jets. Particle jets are matched to calorimeter jets within $\Delta R \leq 0.1$.
The difference between the particle and calorimeter jet p_T is shown in Figure 5.5 for four p_T ranges. In Figure 5.6 the absolute corrections are shown for different cone size jets.
The main source of systematic error is uncertainty on the simulation of the calorimeter response to charge hadrons. The overall uncertainty is approximately of 2 % for low p_T^{jet} and rises to 3 % at high p_T^{jet}.

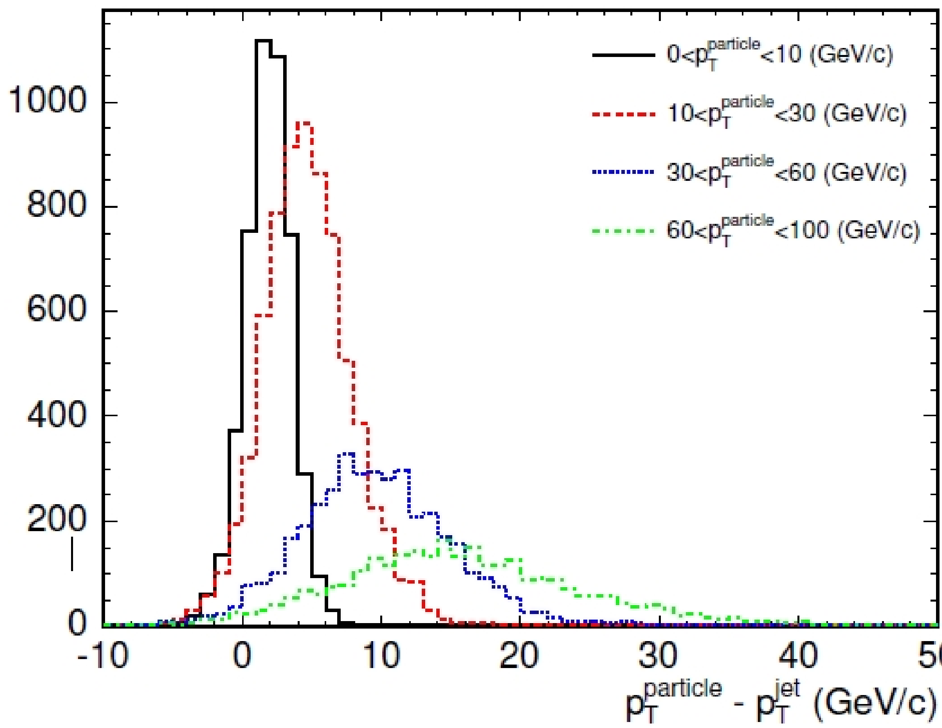

Figure 5.5: p_T difference between particle and calorimeter jet for different p_T range. Image taken from [70].

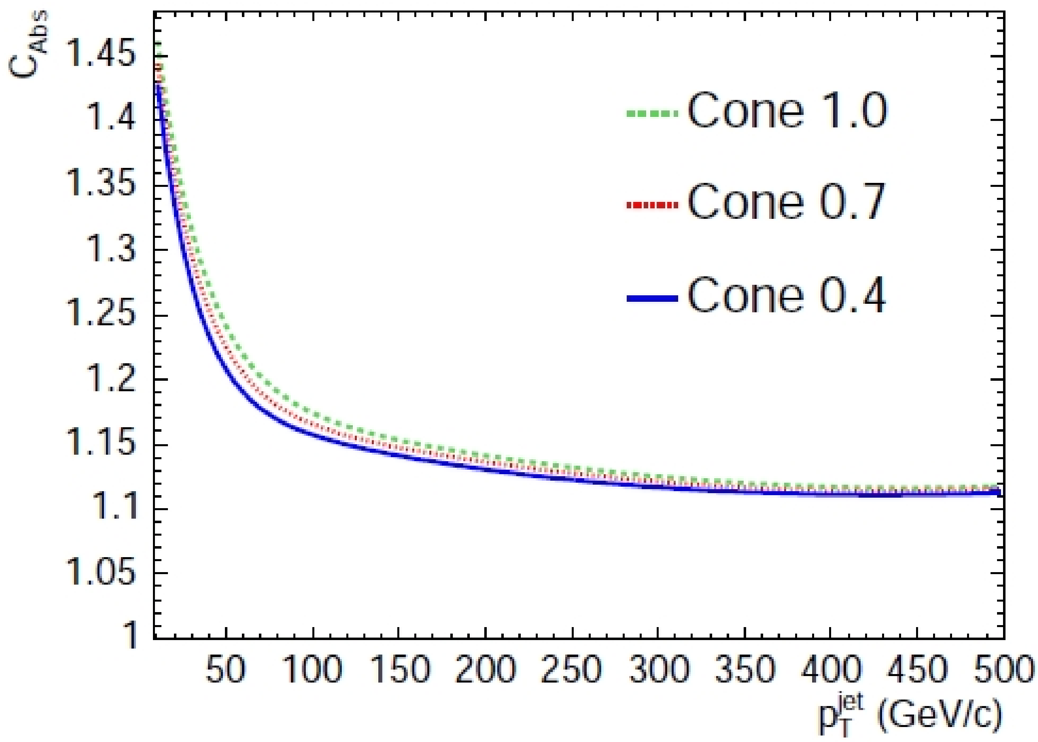

Figure 5.6: Absolute corrections for different cone sizes as a function of calorimeter jet p_T. Taken from [70].

5.4.3 b-tagging : bottom jet identification

In this analysis, it is key to identify jets coming from $b-$quarks. At CDF several algorithms that exploits different qualities of B hadrons have been developed. We use the SecVtx algorithm which takes advantage from the relatively large B lifetime of $\approx 1.5\ ps$ and its large mass $\approx 5\ GeV/c^2$. B-hadrons fly on average 0.5 mm before decaying, which is a larger distance than the intrinsic beam size. Thus their decay products are characterized by a non-zero impact parameter. The algorithm [71] looks for a reconstructed secondary vertex displaced from the primary vertex inside a jet.

Secondary vertex tagging operates on a per-jet basis where only tracks within the jet cone ($|\Delta R| \leq 0.4$) are considered for each jet in the event. A combination of cuts involving the transverse momentum, the number of silicon hits attached to the tracks, the quality of those hits, and the χ^2/ndf of the track fit are applied to discard poorly reconstructed tracks. Only jets with at least two of these good tracks can produce a displaced vertex and are defined as "taggable". Displaced tracks in the jet are selected based on the significance of their impact parameter with respect to the primary vertex. They are used as input to the SecVtx algorithm that used a two-pass approach to find secondary vertices. In the first pass, using tracks with $\mathrm{p_T} \geq 0.5\ GeV/c$ and significance of d_0 (S_{d_0}) greater than 2.0, it attempts to reconstruct a secondary vertex which includes at least three tracks. If the first pass is unsuccessful, it performs a second pass which makes tighter track requirements ($p_T \geq 1$

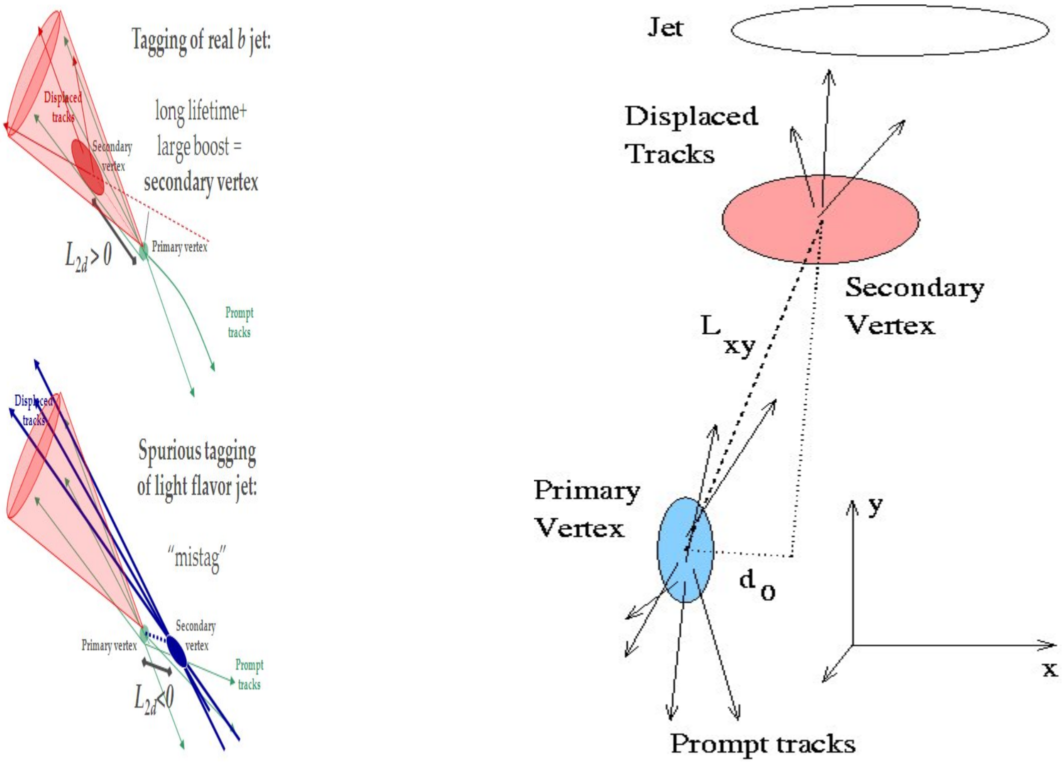

Figure 5.7: Scheme of a tagging variable, in particular the geometrical interpretation of L_{xy} and d_0 is shown.

GeV/c and $S_{d_0} \geq 3.5$) and tries to reconstruct a two-track vertex. Tracks consistent with K_0 or Λ are not considered by the algorithm. In Table 5.2 are summarized the most relevant parameters.
Once a secondary vertex is found inside a jet, two dimensional decay length of the secondary vertex L_{xy} (Figure 5.7) is calculated as the projection onto the jet axis (in r-ϕ view only) of the vector pointing from the primary vertex to a secondary vertex. The sign of L_{xy} is defined relative to the jet direction. To reduce backgrounds a cut on L_{xy} significance is required and according to the value of this cut a loose and a tight Tagger is defined.

Tagging efficiency

The $b-$tag algorithm is calibrated in data. However, since MC simulations are widely used the $b-$tag efficiency is also evaluated in a controlled MC sample. Then a scale factor SF is calculated to take into account possible discrepancies between data and MC. The efficiencies as a function of jet p_T and jet rapidity are shown in Figure 5.8. The average scale factor for the Tight SecVtx Tagger is $SF_{tag} = 0.96 \pm 0.05$ [72].
In order to estimate the efficiency in data we need a control sample of pure b-jets. For this reason, we select dijet events which have a lepton within one jet. Then we require at least one

Variable		SecVtx Tight Pass 1	SecVtx Tight Pass 2
Tracks criteria			
p_T (GeV/c)	>	0.5	1.0
SVXII layer with hits	>	3	3
$\frac{d_0}{\sigma_{d_0}}$	>	2.0	3.5
d_0 (cm)	<	0.15	0.15
$\frac{\chi^2}{n.d.f.}$	<	8.0	8.0
χ^2	<	45	30
$\delta(z_0)$ (cm)	<	2.0	2.0
Vertex criteria			
$\frac{d_0}{\sigma_{d_0}}$ of third track	>	4.0	
at least 1 track with p_T (GeV/c)	>	1.0	1.5
χ^2 of primary vertex	<	50	50
χ^2 of the fit vertex	<	50	50
L_{xy} (cm)	<	2.5	1.2
$\frac{L_{xy}}{\sigma_{L_{xy}}}$	>	7.5	7.5

Table 5.2: SecVtx Tight parameters for Pass 1 and for Pass 2.

tagged jet back-to-back with the lepton jet and we examine the tag rates on the lepton-jet to determine the efficiency.

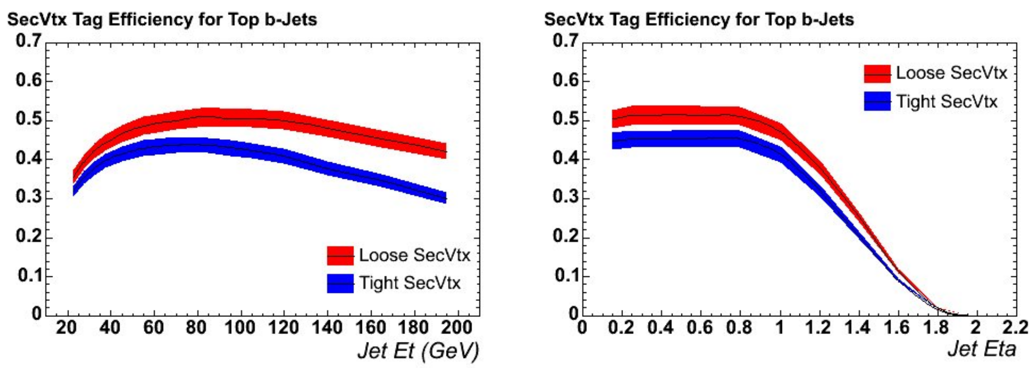

Figure 5.8: Efficiency for SecVtx tagger algorithm as a function of jet p_T and jet rapidity. The measurements were done using $t\bar{t}$ samples. From [72].

The algorithm also tagged jets not coming from heavy flavor quarks. These jets, that fake the SecVtx, are called mistag and their rate is estimated using a parameterization done in a dijet data sample. The results as a function of p_T^{jet} and of Y^{jet} are shown in Figure 5.9.

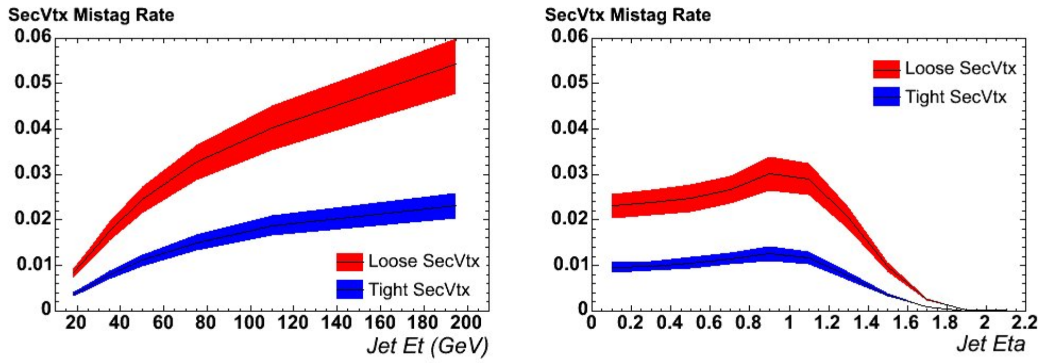

Figure 5.9: SecVtx tagger mistag as a function of jet p_T and jet rapidity. The measurement were perform in data dijet sample. From [72].

6 The $Z/\gamma^* + b-$jet cross section measurement

This chapter describes the $b-$jet cross section measurement produced in association with a Z/γ^* boson. The description includes the measurement definition, the identification of the physics objects utilized in the analysis and the full treatment of the systematic uncertainties. Particular attention is given to the method used to estimate the $b-$jet fraction on data and its uncertainties.

6.1 Measurement definition

The production cross section, σ, for a given physics process, can be determined as follows:

$$\sigma = \frac{N_{data} - N_{bkg}}{A \cdot \mathscr{L}} \tag{6.1}$$

where N_{data} is the number of events observed in the data and N_{bkg} the expected background. A is the acceptance times the event selection efficiency and $\mathscr{L}$ is the total integrated luminosity of the data.
This definition, which corresponds to an event cross section, can be modified to obtain a per jet cross section by replacing the number of events with the number of jets. In this analysis in particular, we are interested in the number of $b-$jets. By defining a per jet cross section in a well defined phase space, the measurement of $Z/\gamma^* + b-$jet cross section would not depend on possible flaws of the $Z/\gamma^* + b$ modeling, such as the number of $b-$jets per event or the extrapolation outside the detector acceptance. Moreover by performing a cross section ratio measurement with respect to Z/γ^* inclusive and Z/γ^*+jets cross sections some systematics (such as luminosity, lepton ID efficiencies) would largely cancel in the ratio. Therefore the measurement will be presented as the per jet cross section ratio with respect to the Z/γ^* inclusive cross section defined as:

$$R = \frac{\sigma(Z/\gamma^*_{(\rightarrow l^+l^-)} + b\ jet)}{\sigma_{(Z/\gamma^* \rightarrow l^-l^+)}} = \frac{A_{Z/\gamma^*}}{A_{Z/\gamma^*+b-jet}} \cdot \frac{N^{data}_{Z/\gamma^*+b-jet} - N_{bkg}}{N^{data}_{Z/\gamma^*} - N_{bkg}} \tag{6.2}$$

where l denotes an electron or muon, A_{Z/γ^*} and $A_{Z/\gamma^*+b-jet}$ are respectively the Z/γ^* and $Z/\gamma^* + b-$jet acceptance times the efficiency.
The definition with respect Z/γ^*+jets is similar and is obtained replacing A_{Z/γ^*} and N^{data}_{Z/γ^*} with the corresponding for Z/γ^*+jet.

The b jets in data are identified using the Tight SecVtx Tagger. Since the tagged jet sample is not only composed by $b-$jets, $N^{data}_{Z/\gamma^*+b-jet}$ is determined from a fit to the secondary vertex mass distribution M_{SecVtx} :

$$N^{data}_{Z/\gamma^*+b-jet} = \frac{n^{tagged}_{data} \cdot f_b}{\epsilon^b_{tag}} \tag{6.3}$$

where n^{tagged}_{data} is the number of tagged jets, f_b the fraction of $b-$jets in the tagged sample obtained from the fit and ϵ^b_{tag} the $b-$tagged efficiency.
The measurement is defined for events with a Z boson in the mass range $66 \leq M_Z \leq 116$ GeV/c^2 and at least a b hadron level jet with $p_T \geq 20$ GeV/c and $|Y^{jet}| \leq 1.5$.
Event selection, secondary vertex mass fit, background subtraction and acceptance calculation are discussed in the following sections.

6.2 Definition of the dataset

We have analyzed the full dataset collected at CDF during Run II (March 2002-September 2011), that consists of $\sim 10\ fb^{-1}$ of integrated luminosity. Events are required to fire one of the following trigger paths for high-$\mathrm{p_T}$ central leptons. Each path consists of different criteria for each trigger level.

- ELECTRON_CENTRAL_18;
  - L1 - A central electron cluster with $E_T > 8$ GeV, $E_{HAD}/E_{EM} < 0.125$, and an associated $p_T > 8$ GeV XFT track.
  - L2 - A central electron cluster with $E_T > 16$ GeV, $E_{HAD}/E_{EM} < 0.125$, and an associated $p_T > 8$ GeV XFT track
  - L3 - A central electron cluster with $E_T > 18$ GeV, $E_{HAD}/E_{EM} < 0.125$, $L_{SHR} < 0.4$ and an associated $p_T > 9$ GeV L3 track that extrapolates to the CES within 8 cm in z cluster position.
- MUON_CMUP18
  - L1 - An XFT track with $p_T > 4$ GeV/c associated with both a CMU and a CMP stub
  - L2 - An XFT track with $p_T > 15$ GeV/c associated with both a CMU and a CMP stub
  - L3 - A minimum ionizing track with $p_T > 18$ GeV/c associated CMU and CMP stubs, $|\Delta X_{CMU}| < 20$ cm, and $|\Delta X_{CMP}| < 10$ cm.
- MUON_CMX18
  - L1 - An XFT track with $p_T > 8$ GeV/c associated with a CMX stub and CSX scintillator information

  - L2 - An XFT track with $p_T > 15$ GeV/c associated with a CMX stub
  - L3 - A minimum ionizing track with $p_T > 18$ GeV/c associated with a CMX stub with $|\Delta X_{CMX}| < 10$ cm

- MUON_CMP18
  - L1 - An XFT track with $p_T > 15$ GeV/c
  - L2 - An XFT track with $p_T > 15$ GeV/c and hits in ≥ 4 COT super layers
  - L3 - A minimum ionizing track with $p_T > 18$ GeV/c associated with a CMP stub with $|\Delta X_{CMP}| < 20$ cm

- MUON_CMU18
  - L1 - An XFT track with $p_T > 10$ GeV/c associated with a CMU stub
  - L2 - An XFT track with $p_T > 14$ GeV/c associated with a CMX stub and at least hits in 4 COT super layers
  - L3 - A minimum ionizing track with $p_T > 18$ GeV/c associated with a CMU stub with $|\Delta X_{CMU}| < 10$ cm

From all the data collected during Run II only those events acquired with a functional silicon tracker, electron systems and central muon systems (CMU,CMP and CMX) are considered. The total integrated luminosity per channel is $\sim 9.1\ fb^{-1}$.

6.2.1 Electron Trigger Efficiency

The electron trigger requires a cluster of energy in the central electromagnetic calorimeter and a track associated to the cluster. The trigger efficiency is evaluated separately for the calorimeter and for the track requirements. The efficiency of the calorimeter is found to be flat as function of the electron E_T and consistent with 100%. The track efficiency is calculated using a sample of $W \to e\nu$ events passing a trigger with the same calorimeter requirements as for the electron trigger used in the analysis but which does not have tracking requirements. The efficiency is evaluated for each trigger level and for each period. The final values for electron trigger efficiency is reported in Table 6.1.

6.2.2 Muon Trigger Efficiency

Four muon triggers corresponding to the central muon detectors are used. All of them require a reconstructed track in the COT matched to a stub in the corresponding muon chamber. In order to evaluate the trigger efficiencies, events with a reconstructed $Z/\gamma^* \to \mu^+\mu^-$ in which one muon is fiducial in CMX and the other is fiducial to CMU and CMP are selected. The Z/γ^* reconstruction is performed with the same selection used in the analysis (section 6.4). For each period p, Z/γ^* events are divided in categories in relation to the trigger that they fired, for example N_{CMX}, N_{CMUP} and $N_{CMX-CMUP}$. The event yield for each category corresponds to:

$$N^p_{CMUP-CMX} = \epsilon^p_{CMUP} \cdot \epsilon^p_{CMX} \cdot F^p$$

$$N^p_{CMUP} = \epsilon^p_{CMUP} \cdot F^p$$
$$N^p_{CMX} = \epsilon^p_{CMX} \cdot F^p$$
$$F^p = \mathscr{L} \cdot \sigma(Z \to \mu^+\mu^-) \cdot A$$
$$p = 0d, 0h, 5-7, 8, ..., 38$$

where $\mathscr{L}^p$ is the integrated luminosity for period p, $\sigma(Z \to \mu^+\mu^-)$ is the inclusive cross section of Z/γ^* production and A is the Z/γ^* reconstruction acceptance.
The CMUP and CMX trigger efficiencies for each period are obtained as:

$$\epsilon^p_{CMUP} = \frac{N^p_{CMUP-CMX}}{N^p_{CMX}}$$
$$\epsilon^p_{CMX} = \frac{N^p_{CMUP-CMX}}{N^p_{CMUP}}$$

The same method is used for the CMU (CMP) trigger efficiency where, in this case, the Z/γ^* is reconstructed with one muon fiducial in CMX and the other in CMU (CMP). The results are shown in Table 6.1.

6.3 Monte Carlo Samples

Monte Carlo simulated samples are used to model Z/γ^*+ jets events, to estimate background contributions, to evaluate the acceptance and to build the secondary vertex mass templates. These templates are used to discriminate the different jet flavors in the tagged sample. MC events are produced according to its respective generator algorithm and then passed through the GEANT 3 based [73] CDF detector simulator. Several checks are performed to guarantee the agreement between data and MC distributions (section 6.6).

6.3.1 Alpgen+Pythia $Z + jets$ MC

ALPGEN v2.10' interfaced to PYTHIA v6.325 tune BW with CTEQ5L PDFs [74] is used to simulate Z/γ^*+ jets events. Samples were generated for $Z/\gamma^* + 0, 1, 2, 3, 4$ partons with the built-in mechanism, called "MLM matching" (see section 2.4.3), to remove overlap between jets from parton showers (PS) and from matrix element (ME) at the generator level. Since this procedure is not applied to heavy flavor (HF) quarks, when combining the samples, we remove events in each sample in order to avoid double-counting. Alpgen generates ME heavy flavor separately ($Z/\gamma^* + Np$, $Z/\gamma^* + bb + Np$, $Z/\gamma^* + cc + Np$). In the ME light flavor sample ($Z/\gamma^* + Np$) Alpgen generates only up, down, strange and massless charm quarks, while the parton shower, done by Pythia, can generate all five flavors with mass. A heavy flavor double-counting can occur: for example $Z/\gamma^* + b\bar{b} + 1p$ and $Z/\gamma^* + 1p + (bb)^{PS}$ can occupy the same phase space. The procedure applied to avoid this overlap is a jet-based removal that allows HF from ME only if they are in a different reconstructed jet and from

Period	$\epsilon_{electron}$	ϵ_{CMUP}	ϵ_{CMX}	ϵ_{CMU}	ϵ_{CMP}
0d	0.962 ± 0.007	0.831 ± 0.008	0.963 ± 0.004	0	0
0h	0.976 ± 0.006	0.838 ± 0.007	0.868 ± 0.006	0	0
5-7	0.979 ± 0.004	0.833 ± 0.008	0.854 ± 0.008	0	0
8	0.959 ± 0.007	0.847 ± 0.010	0.858 ± 0.010	0	0
9	0.960 ± 0.002	0.827 ± 0.011	0.804 ± 0.011	0	0
10	0.959 ± 0.002	0.799 ± 0.009	0.859 ± 0.008	0	0.392 ± 0.023
11	0.961 ± 0.004	0.781 ± 0.010	0.836 ± 0.009	0	0.483 ± 0.022
12	0.960 ± 0.003	0.764 ± 0.013	0.795 ± 0.012	0	0.596 ± 0.029
13	0.957 ± 0.003	0.761 ± 0.010	0.780 ± 0.010	0	0.653 ± 0.020
14	0.960 ± 0.030	0.803 ± 0.025	0.782 ± 0.025	0	0.720 ± 0.052
15	0.963 ± 0.005	0.788 ± 0.012	0.825 ± 0.012	0	0.561 ± 0.027
16	0.961 ± 0.005	0.742 ± 0.016	0.839 ± 0.015	0	0.551 ± 0.032
17	0.962 ± 0.003	0.766 ± 0.012	0.842 ± 0.011	0	0.557 ± 0.026
18	0.962 ± 0.003	0.750 ± 0.008	0.830 ± 0.008	0	0.551 ± 0.018
19	0.962 ± 0.003	0.753 ± 0.011	0.815 ± 0.010	0	0.495 ± 0.025
20	0.959 ± 0.003	0.750 ± 0.011	0.822 ± 0.010	0	0.514 ± 0.023
21	0.958 ± 0.002	0.746 ± 0.008	0.829 ± 0.007	0.103 ± 0.011	0.482 ± 0.017
22	0.958 ± 0.003	0.752 ± 0.010	0.850 ± 0.009	0.632 ± 0.022	0.500 ± 0.022
23	0.960 ± 0.003	0.752 ± 0.012	0.807 ± 0.011	0.637 ± 0.025	0.480 ± 0.024
24	0.960 ± 0.003	0.735 ± 0.011	0.813 ± 0.010	0.568 ± 0.024	0.420 ± 0.022
25	0.960 ± 0.003	0.739 ± 0.011	0.797 ± 0.011	0.683 ± 0.024	0.453 ± 0.024
26	0.953 ± 0.003	0.766 ± 0.013	0.782 ± 0.013	0.753 ± 0.026	0.530 ± 0.027
27	0.950 ± 0.003	0.768 ± 0.008	0.800 ± 0.008	0.771 ± 0.016	0.496 ± 0.017
28	0.950 ± 0.003	0.739 ± 0.010	0.792 ± 0.010	0.721 ± 0.022	0.553 ± 0.023
29	0.950 ± 0.003	0.740 ± 0.009	0.772 ± 0.009	0.668 ± 0.020	0.429 ± 0.020
30	0.946 ± 0.003	0.729 ± 0.009	0.752 ± 0.009	0.614 ± 0.019	0.422 ± 0.018
31	0.943 ± 0.007	0.723 ± 0.014	0.737 ± 0.014	0.627 ± 0.030	0.409 ± 0.030
32	0.939 ± 0.007	0.708 ± 0.009	0.747 ± 0.009	0.637 ± 0.018	0.426 ± 0.018
33	0.941 ± 0.007	0.711 ± 0.010	0.719 ± 0.010	0.602 ± 0.021	0.417 ± 0.020
34	0.942 ± 0.007	0.720 ± 0.009	0.771 ± 0.009	0.559 ± 0.020	0.410 ± 0.019
35	0.937 ± 0.007	0.721 ± 0.010	0.741 ± 0.010	0.559 ± 0.021	0.403 ± 0.020
36	0.940 ± 0.007	0.697 ± 0.010	0.729 ± 0.010	0.490 ± 0.021	0.368 ± 0.019
37	0.941 ± 0.007	0.726 ± 0.014	0.718 ± 0.014	0.490 ± 0.032	0.463 ± 0.028
38	0.940 ± 0.007	0.725 ± 0.012	0.717 ± 0.012	0.549 ± 0.027	0.439 ± 0.026

Table 6.1: Trigger efficiencies for electron and muon triggers.

PS only if they end up in the same jet.
Since the MC samples are generated using a luminosity profile representative of only a fraction of the data sample, a reweight procedure was applied to match that of the full dataset. This was done converting the luminosity profile in a multiple interactions profile and using the latter to reweight the MC.

6.3.2 Pythia MC

Pythia Tune A MC samples are used to simulate inclusive $Z/\gamma^* \to l^+l^-$ production, top pair production and dibosons (WW, WZ, ZZ). Λ_{QCD} is set to 0.146 and the PDFs used are CTEQ5L [74].

6.4 Event Selection

The event selection starts at online level when the trigger requirements described in Section 6.2 are applied. Data is then analyzed offline to reconstruct the physics objects of interest. In this case the event signature contains two high-p_T leptons (electrons or muons) and at least a $b-$jet.
The full event selection is explained in this section. The same selection is applied on data and on simulated events from Monte Carlo programs.
Events passing trigger criteria are required to have a high-quality $z-$vertex within 60 cm from the center of the detector. In the same way all the MC events are filtered requiring the generated primary vertex to be within 60 cm from the center. This suppresses non-collision backgrounds and removes events with abnormal calorimeter topologies which might violate assumptions implicit in the standard jet energy corrections [70].
Z/γ^* boson candidates are reconstructed via the identification of two high-p_T leptons. In the case of the decay into a pair of electrons, they are required to have $E_T \geq 20$ GeV, being central ($|Y| \leq 1.0$) or one of them central and the other in the forward region ($1.2 \leq |Y| \leq 2.8$). For muons, they should have $p_T \geq 20$ GeV/c, opposite charges and invariant mass $66 \leq M_{\mu\mu} \leq 116$ GeV/c^2 (the same cuts are applied to M_{ee}).
The procedures explained in Chapter 5 are utilized to reconstruct leptons and jets. Further cuts are made to identify these objects reducing contributions from false signals and background sources. The standard way to identify leptons is to apply a rectangular cuts on a set of variables suitable to differentiate fake leptons from real ones while in this analysis they are identified by means of an Artificial Neural Network (ANN). This allows to use the full distribution of variables, increasing the lepton identification efficiency while keeping a similar fake rejection rate.

6.4.1 Muon identification and $Z/\gamma^* \to \mu^+\mu^-$ reconstruction

Two ANNs are trained to discriminate between high-p_T muons coming from a $Z/\gamma^* \to \mu^+\mu^-$ decay and two different sources of fake (misidentified) muons. The first category of fakes comes from tracks of charged particles originated within jet fragmentation. This kind of

fakes can be distinguished from real muons because they have similar probability to have same charge or opposite charge with respect to a muon identified in the same event. For this reason this category is defined as *Same Charge* (SC) fakes. The other category of fake muons comes from low $\mathrm{p_T}$ charged particles that undergo a decay in flight, and which, due to a kink in their trajectory, are incorrectly reconstructed as high $\mathrm{p_T}$ tracks. This category is defined as *Decay in Flight* fakes (DIF) and can be distinguished from real muons for their high impact parameter and poor quality of the tracking fit.
Three different samples of muons corresponding to real muons, SC fakes and DIF fakes are selected from data in the high-p_T sample using the following criteria.

- Real muons from $Z/\gamma^* \to \mu^+\mu^-$ decay
  - One tight CMUP or CMX
    - At least 2 COT SL
    - $|d_0| \leq 0.2$ cm if no silicon track or $|d_0| \leq 0.02$ cm if silicon track
    - $Isol04 \leq 0.1$
    - $E_{HAD} \geq 6$ GeV
    - $E_{Em} \geq 2$ GeV
  - W + jet veto: discard events with $\not{E}_T > 20$ GeV[1] and $p_T^{jet} > 15$ GeV/c
  - Select probe muons passing kinematic requirements associated to an identified tag muon so that the two muons have
    - Opposite charge
    - $\Delta z_0 < 4\ cm$
    - Invariant mass within $86 - 96\ GeV/c^2$
- Fake SC muons
  - One tight CMUP or CMX muon
  - Select probe muons passing kinematic requirements and $\frac{\chi^2}{n.d.f.} \leq 4$ associated to an identified tag muon so that the two muons have
    - Same charge
    - $\Delta z_0 < 4\ cm$
- Fake DIF muons
  - One tight CMUP or CMX muon
  - W + jet events: $\not{E}_T > 20$ GeV and $p_T^{jet} > 15$ GeV/c
  - Select muons passing kinematic requirements and $|d_0| > 0.2\ cm$

Figure 6.1 shows some relevant distributions for the three data driven muon and fakes samples.
The ANN used to differentiate SC fakes from signal muons employs the following variables:

[1] Missing E_T: is the missing transverse energy, defined as the magnitude of $-\sum E_T^i \hat{n}^i$ where $\hat{n}^i$ is the unit vector in the azimuthal plane that points from the beam line to the ith calorimeter tower.

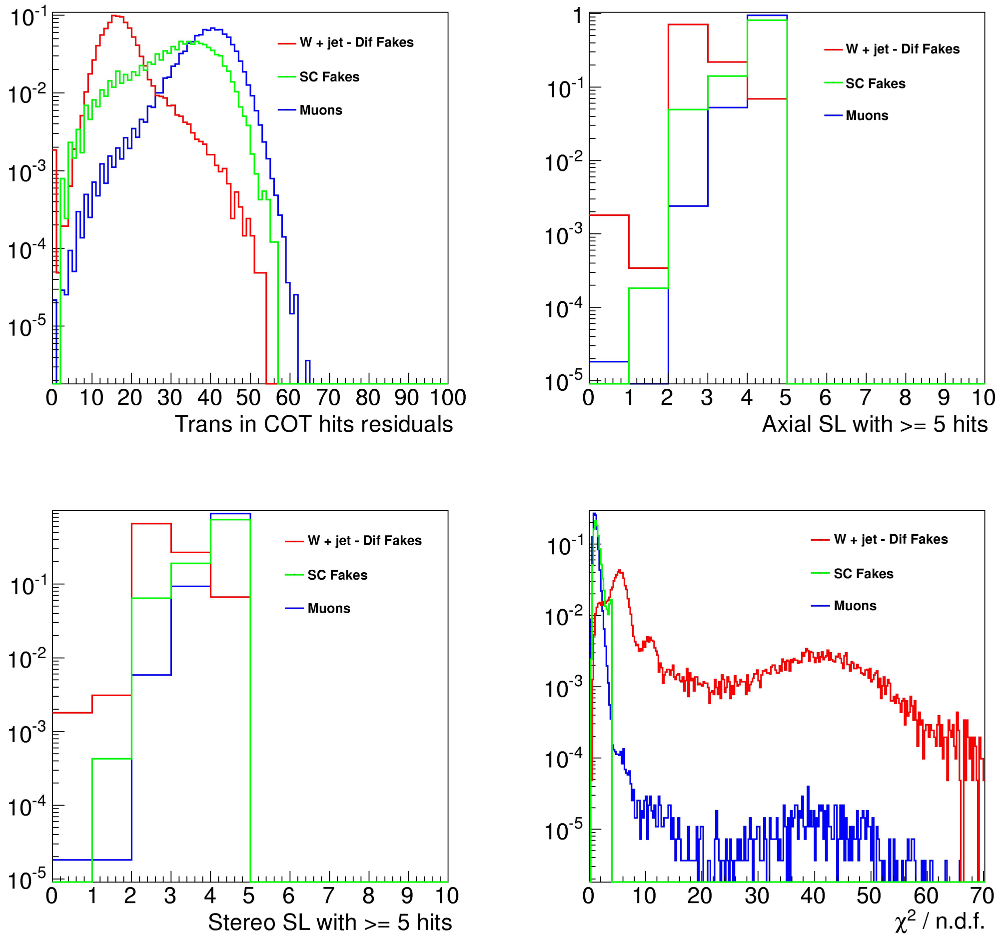

Figure 6.1: Comparison between probe and fake muons for some kinematical distributions used by muon ANNs to discriminate between real muons and fakes. The distributions are normalized to 1.

- Energy in the EM calorimeter
- Energy in the HAD calorimeter
- Number of Axial COT SL with at least 5 hits
- Number of Stereo COT SL with at least 5 hits
- Number of COT hits
- Number of Silicon hits
- Distance from $z-$vertex
- Impact parameter d_0
- Isolation

The DIF fake ANN makes use of:

- Energy in the EM calorimeter
- Energy in the HAD calorimeter
- Number of Axial COT SL with at least 5 hits
- Number of Stereo COT SL with at least 5 hits
- Number of COT hits
- Number of Silicon hits
- Number of transitions in the residuals of the COT fit
- $\frac{\chi^2}{n.d.f}$
- Maximum number of consecutive residuals on the same side of the track in the COT track fit
- Distance from $z-$vertex

Figure 6.2 (6.3) shows the muon efficiency, ϵ_{ID}, and fake muon survival rate as function of the output of the trained SC (DIF) ANN and Figure 6.4 presents the output of the trained ANNs. The ϵ_{ID} are high, close to 99 % over almost all the ANN output range, allowing to obtain high efficiency with very low background. Cuts for each ANN were found optimizing the significance $\frac{S}{\sqrt{(S+B)}}$ with S the number of reconstructed $Z/\gamma^* \rightarrow \mu^+\mu^-$ and B the background (Figure 6.5). Muons are selected if the SC ANN output is higher than 0.875 and the DIF ANN output is higher than 0.9. With this selection the Z/γ^* acceptance is increased by $\sim 34\%$.

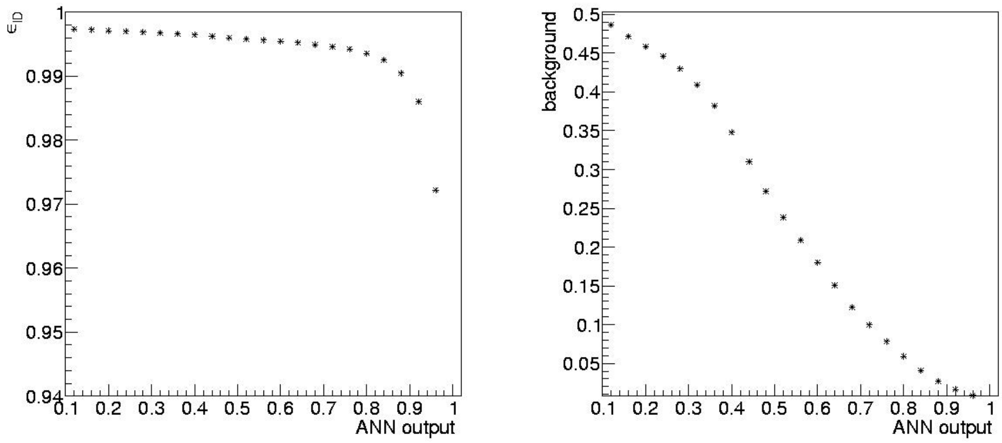

Figure 6.2: Muon ϵ_{ID} and background reduction rate as function of Same Charge ANN output. The cut on this ANN output in the analysis is 0.875.

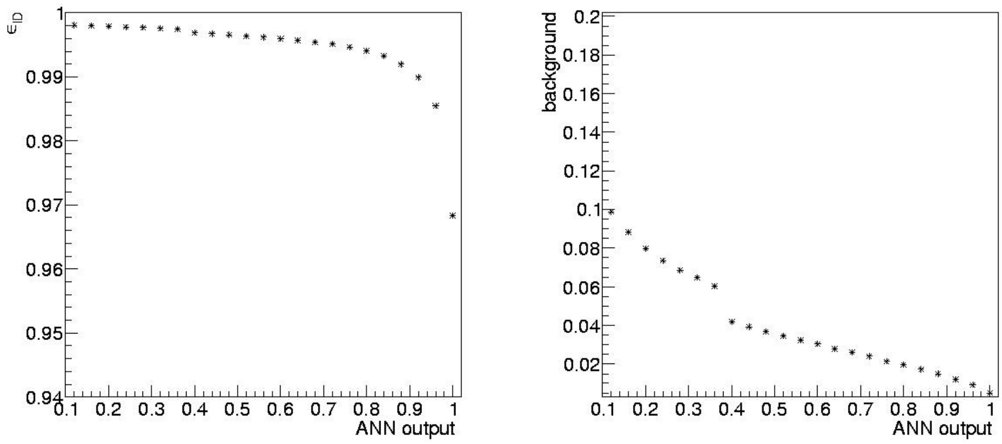

Figure 6.3: Muon ϵ_{ID} and background reduction rate as function of Decay In Flight ANN output. The cut applied in the analysis on this ANN output is 0.9.

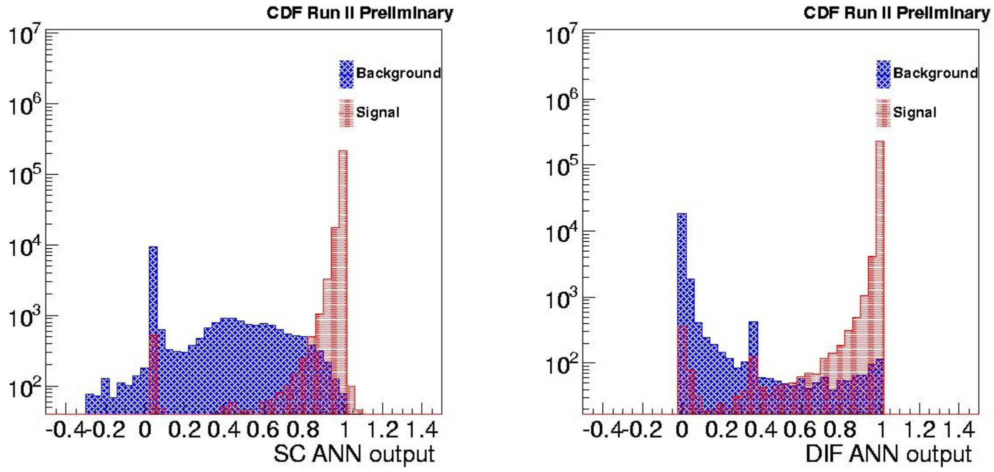

Figure 6.4: SC and DIF ANNs output.

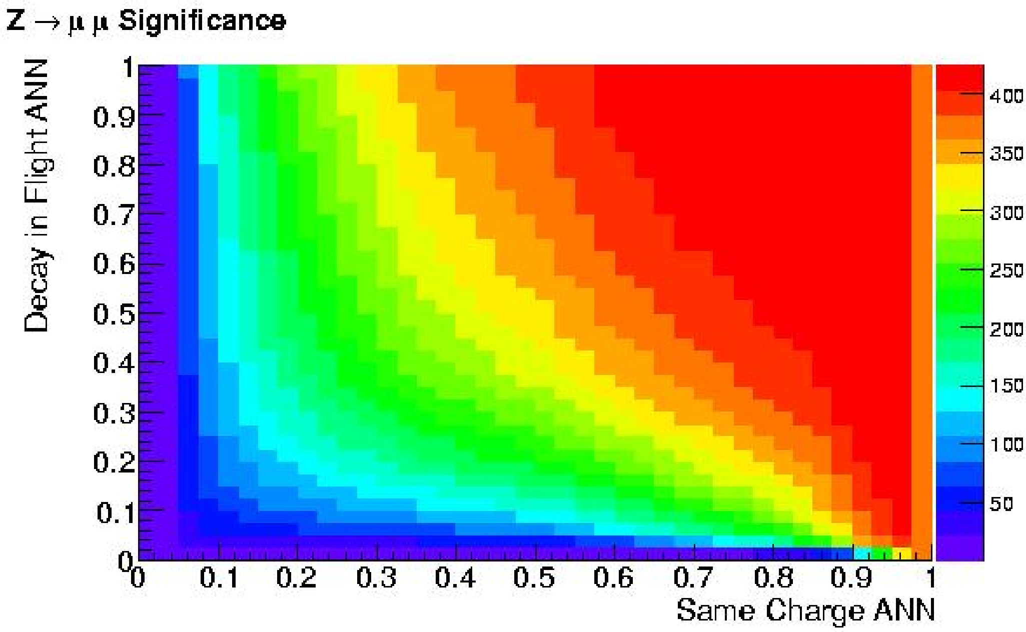

Figure 6.5: $Z/\gamma^* \to \mu^+\mu^-$ inclusive significance as a function of the output of the SC and DIF ANNs.

The muon identification efficiency

The muon identification efficiency and the data/MC scale factors are calculated using the lepton counting method in a Z/γ^* sample. This consist in defining a tag leg muon and a probe tag muon. The tag leg is a muon passing the kinematics and identification criteria and should be linked to a stub in a muon detector. The probe leg is a muon that passes the kinematics cuts and that, coupled with the tag leg, should have an invariant mass within 86-96 Gev/c^2. Tag and probe muon couples should have opposite track charges and $|\Delta Z_0| \leq 4$ cm. All events with at least one tag-probe pair are selected and the probe legs are used to calculate the identification efficiency using

$$\epsilon_{ID} = \frac{N_{ID}}{N_{probe}} \tag{6.4}$$

where N_{probe} is the number of probe muons, and N_{ID} is the subset of probe legs which pass the identification selection. The muon efficiencies are combined into Z/γ^* reconstruction efficiencies and then a scale factor for each category is evaluated. Since the reconstruction efficiencies for each category were found to be consistent within the statistical uncertainties, an overall efficiency is evaluated and shown as a function of the different data periods in Figure 6.6.

Z/γ^* reconstruction

Muons passing the identification requirements are used to reconstruct the $Z/\gamma^* \to \mu^+\mu^-$ candidates. Events are selected if the reconstructed Z/γ^* boson has an invariant mass within 66-116 GeV/c^2. Categories are divided depending on the trigger that fired the event and the category the muon belongs to (such as CMUP-CMUP, CMX-CMIO, etc). Reconstruction efficiency and data/MC scale factors are calculated for each Z/γ^* category and for each period combining trigger and muon identification efficiencies.

6.4.2 Electron identification and $Z/\gamma^* \to e^+e^-$ reconstruction

The electron identification is done similarly to the muon case using the help of two artificial neural networks. It is based on the discrimination between real high-p_T electrons coming from $Z/\gamma^* \to e^+e^-$ decay (probes) and jets that could fake the electron signal. Both samples are selected from data, probe electrons from high$-p_T$ dataset and fakes from a dijet dataset according to the following criteria:

Probes electrons from $Z/\gamma^* \to e^+e^-$

- One very tight electron (tag electron)
  - $E_T \geq 20$ GeV
  - $p_T \geq 10$ GeV/c

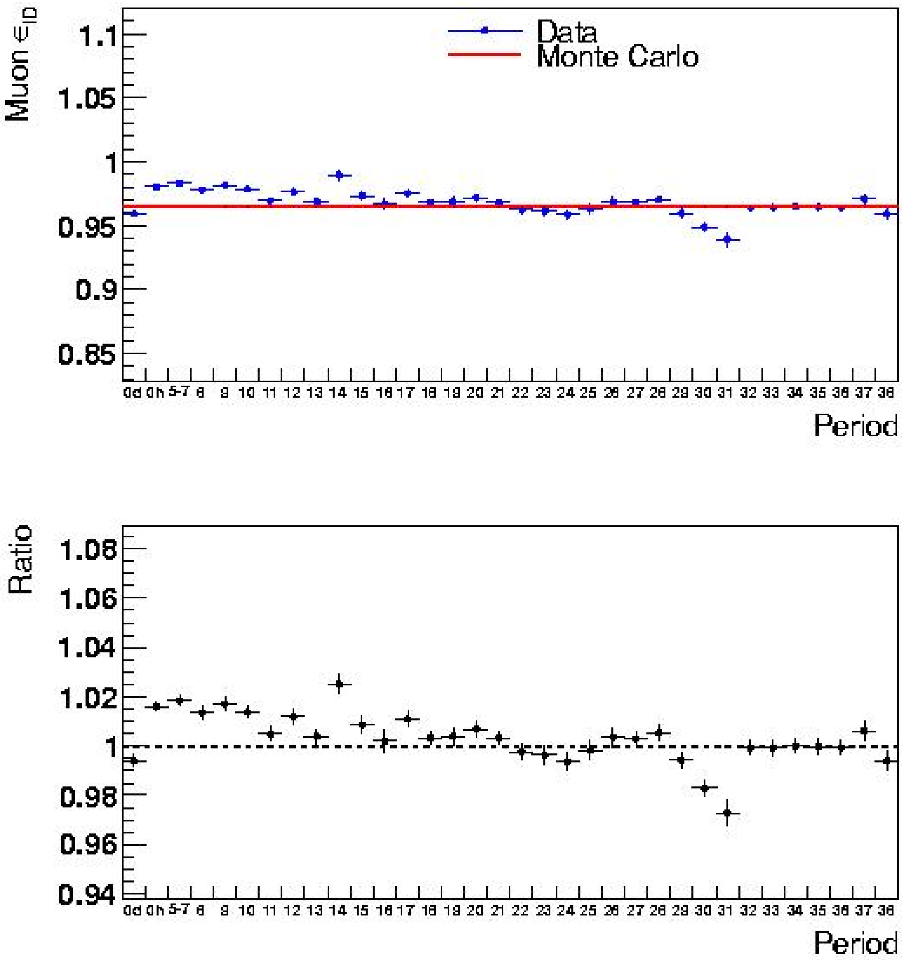

Figure 6.6: Event Muon identification efficiency in data and Monte Carlo as a function of the data period. On the bottom plot is shown the data/MC scale factors.

  - $L_{shr} \leq 0.1$
  - $E/P \leq 1.2$
  - $E_T(\Delta R \leq 0.4)/E_T(e) \leq 0.05$
  - firing $ELECTRON\_18$ trigger

- Discard events with $\not\!\!E_T \geq 20$ GeV, to reduce W+jets contribution

- Select probe electron passing basic kinematic cuts:
  - $E_T \geq 20$ GeV for central or plug electron
  - $p_T \geq 10$ GeV/c only for central electrons
  - associated to a tag electron so that the two electrons have invariant mass in [86−96] GeV/c^2 range and opposite charge if both are central

Fake electrons:

- candidates from dijet dataset, where there is at least one jet with $p_T \geq 20$ GeV/c and one fakeable object (electron matched with a jet)
- discard events with $\not\!\!E_T \geq 20$ GeV
- the fakeable object should pass some basic kinematic cuts:
  - $E_T \geq 20$ GeV for central and plug
  - $p_T \geq 10$ GeV/c and $|z_0| \leq 60$ cm only if it is central
- should exist a jet with $p_T \geq 20$ GeV/c that is matched with the fakeable object. This jet should not be the leading jet to avoid trigger bias.
- combination of the leading jet and fakeable object should be outside the Z mass peak

Two different ANNs are trained to differentiate real electrons from fakes: one for central and the other for plug electrons.
The central ANN employs the following variables:

- CES χ^2 [2]
- E_{Had}/E_{Em}
- Isolation/E_T
- Number of Si Hits

[2] Comparison of the CES shower profile on the $r - z$ plane to the expected profile as measured for electrons in the test beam

- Number of Axias COT SL with at least 5 Hits
- Number of Stereo COT SL with at least 5 Hits
- Number of tracks associated to the electron candidate
- E/P

while the plug ANN utilizes:

- Pem χ^2 [3]
- Pes U energy/ Pes average E [4]
- Pes V energy/ Pes average E
- ΔR Pem-Pes
- Pem cluster energy / E_T
- E_{Had}/E_{Em}
- Isolation/E_T

Figures 6.7 and 6.8 show the distribution comparison between fakes and probes for the variables in the ANN, while the output of the two ANNs is presented in Figure 6.9.

Central electrons are selected using a cut of 0.8 on the ANN output, while for the plug electrons a cut of 0.4 on the corresponding ANN is applied. These cuts are chosen based on the ϵ_{ID} and background rate shown in Figures 6.10 and Figure 6.11. With these values, the background rate is low and comparable to that obtained using rectangular cuts. The Z/γ^* acceptance is larger respect to the standard Z/γ^*+jets cuts [75] by $\sim 42\%$.

The electron identification efficiency

Also the electron identification efficiency and the data/MC scale factors are evaluated using the lepton counting method in $Z/\gamma^* \rightarrow e^+e^-$ sample. In this case the method consists in defining a tag electron that passes the kinematics and the identifications cuts together with a probe electron requiring to pass only the kinematic selection and to form with the tag electron an invariant mass within the Z mass peak 86-96 GeV/c^2. All events having a tag-probe couple so defined are selected and the probe electrons are used to evaluate the efficiency according to this formula:

$$\epsilon_{ID} = \frac{N_{ID}}{N_{probes}} \tag{6.5}$$

[3] Value of the 3x3 PEM cluster energy distribution as compared to the hypothesis that EM object is an electron cluster

[4] Pes average energy is calculated as : (Pes U energy +1.2 * PES V energy)/2.2

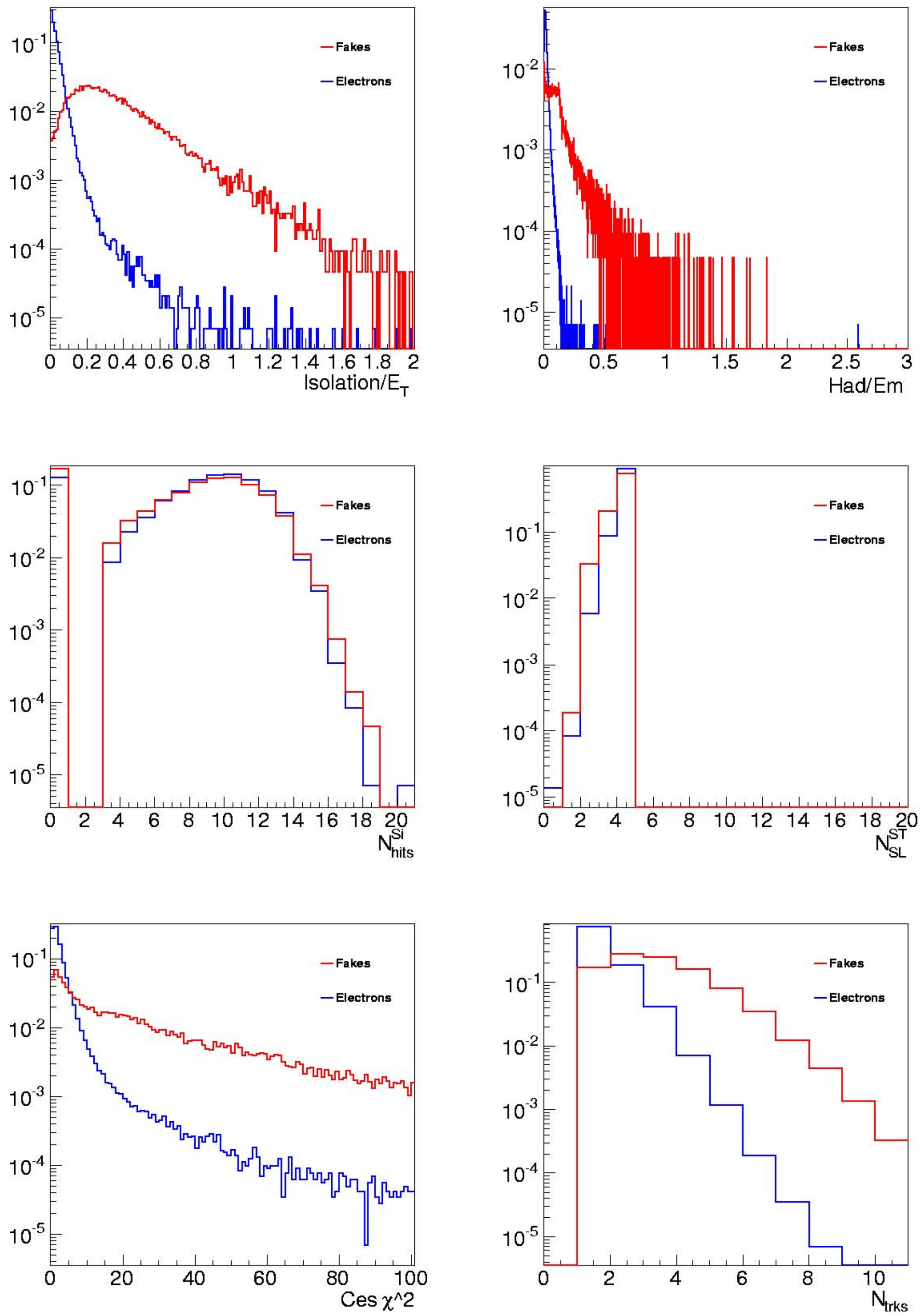

Figure 6.7: Comparison between fake and probe central electron distributions for the variables used in the central ANN.

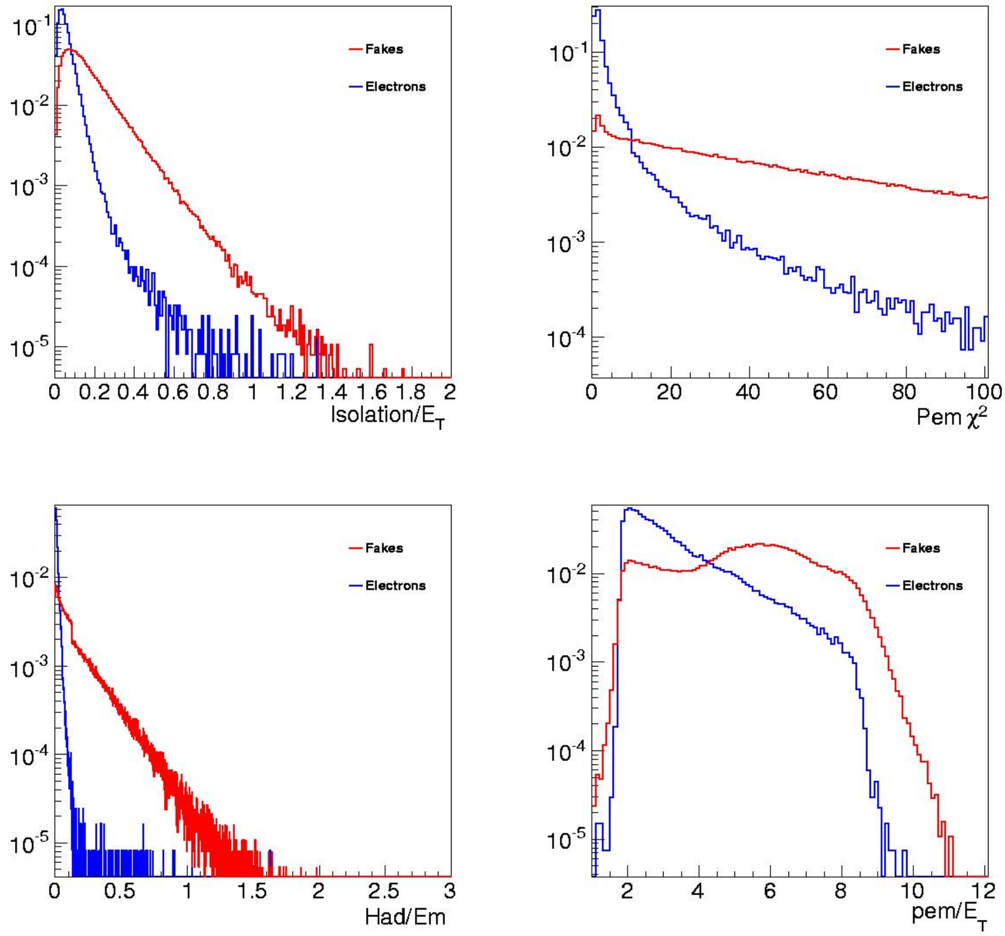

Figure 6.8: Comparison between fake and probe plug electron distributions for the variables used in the plug ANN.

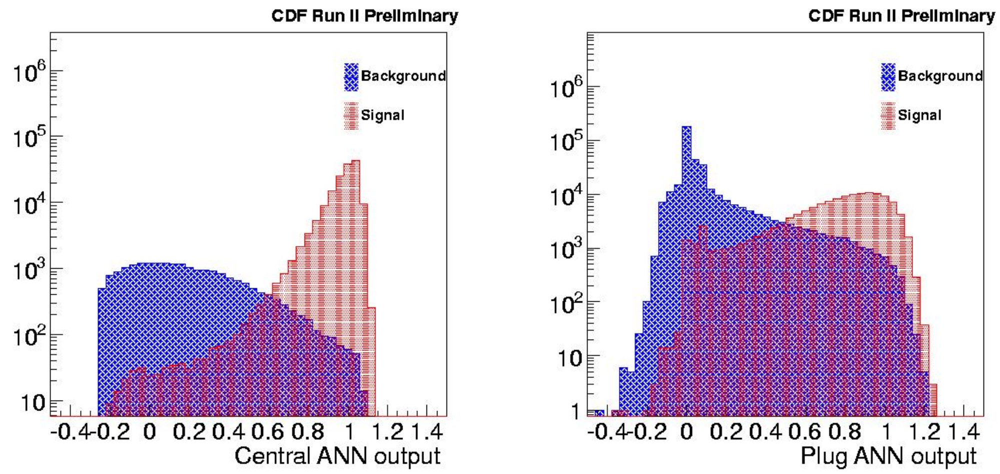

Figure 6.9: Output of the central and plug ANNs

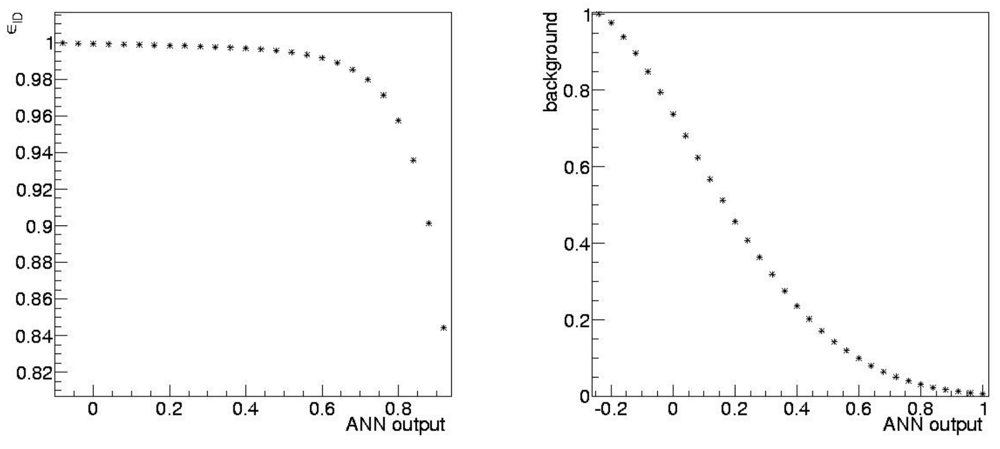

Figure 6.10: Electron ϵ_{ID} and background reduction rate as a function of central ANN

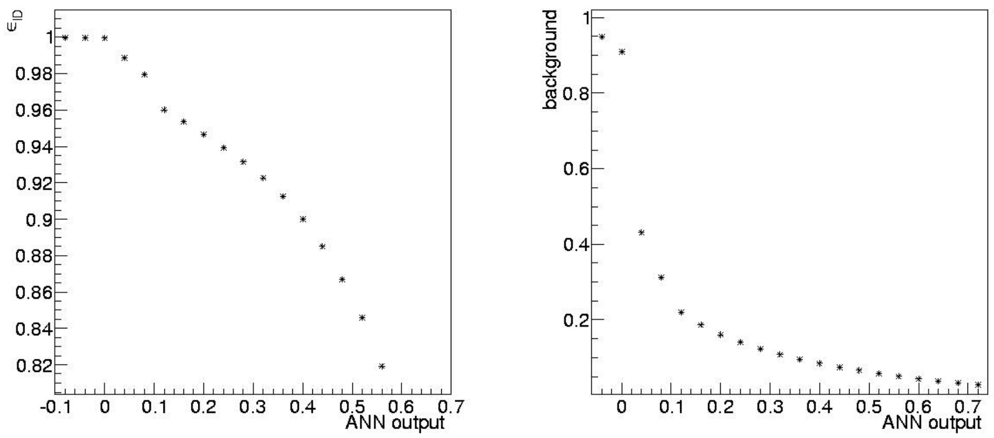

Figure 6.11: Electron ϵ_{ID} and background reduction rate as a function of plug ANN

where N_{probe} is the number of probe legs and N_{ID} are those probes that pass also the identification criteria. A different identification efficiency is evaluated for every period and for central and plug electrons, the results are shown in Figure 6.12

Z/γ^* reconstruction

The $Z/\gamma^* \to e^+e^-$ is divided in 2 categories, central-central (CC) or central-forward (CF), depending on the category the electron belongs to (CEM or PEM). The Z/γ^* reconstruction efficiency and data/MC scale factors are calculated for each category and for each period combining trigger and electron identification efficiency. Events are selected if the Z/γ^* has an invariant mass within 66-116 GeV/c^2.

6.4.3 Jet selection

Jets are identified using the MidPoint algorithm with a cone size of R=0.7 and a merging/splitting fraction set to 0.75. In data and MC, jets are clustered using calorimeter towers with transverse momentum above 0.1 GeV/c and seed towers of 1 GeV/c after excluding the towers associated to leptons from the Z/γ^* boson decay. In addition we also require a minimum distance between jet and leptons: $\Delta R_{lepton-jet} \geq 0.7$. After reconstruction the momentum of the jet is corrected following the prescription explained in Chapter 5 . Jets are not corrected for underlying event or energy loss due to out-of-cone parton radiation. Measurements are performed at hadron level and these corrections (UE and hadronization) are applied to the theoretical predictions (see Chapter 8).
Jets are required to have $p_T \geq 20$ GeV/c and $|Y| \leq 1.5$. The rapidity cut is due to the reduction of $b-$tagging efficiency at larger rapidity values. It falls rapidly since a requirement of COT hits is made by the SecVtx algorithm to maintain a good track purity.

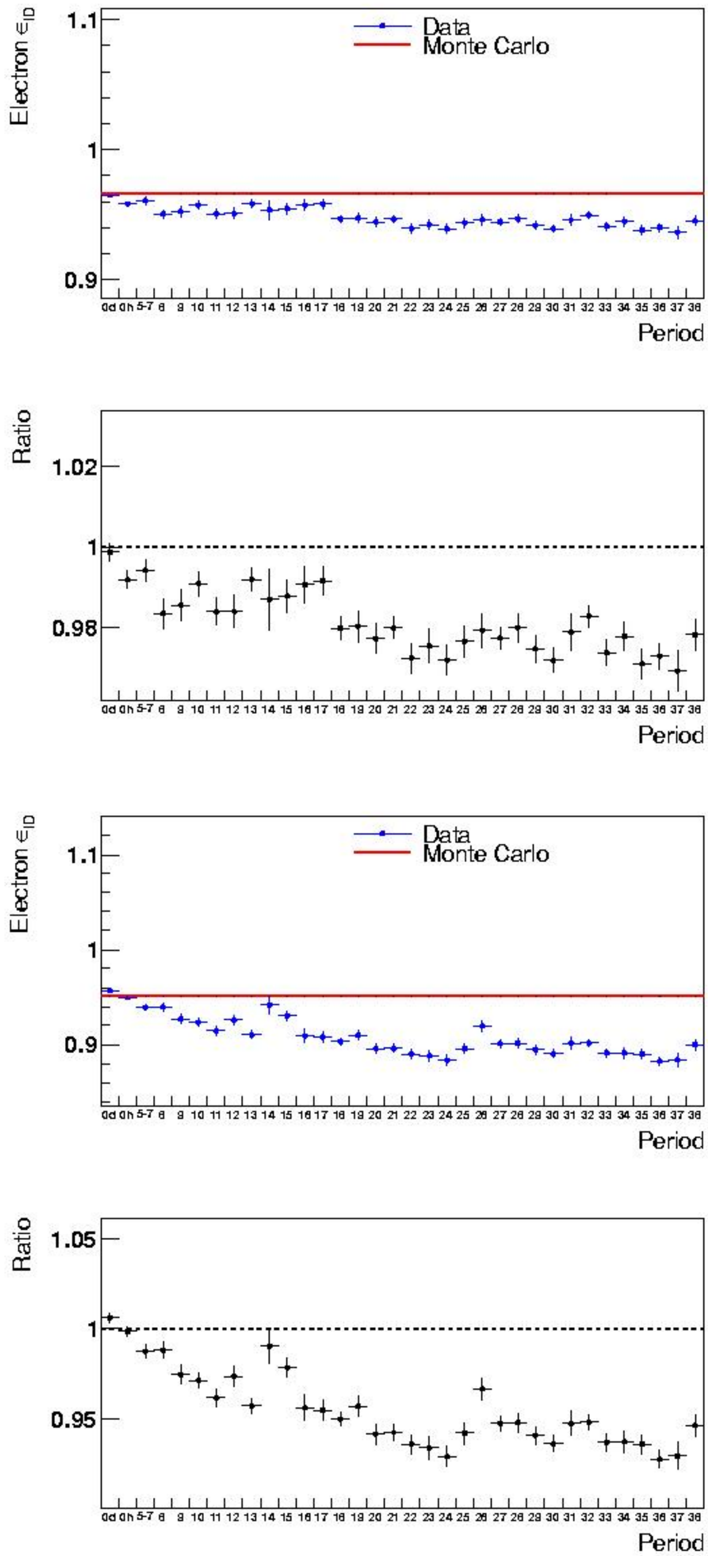

Figure 6.12: Event Electron identification efficiency in data and Monte Carlo as a function of the data period for CEM and for PEM. On the bottom of each plot the data/MC ratio that represents the scale factors.

b tagged jets

Jets are further required to have a reconstructed secondary vertex within a cone of 0.4 around the jet axis. The secondary vertex is reconstructed using the TIGHT SECVTX package. The efficiency of reconstructing a $b-$jet has been measured in data and Monte Carlo and varies between 30 % and 40% for the jet p_T and rapidity range of interest. Following these studies the Monte Carlo efficiency is adjusted by a scale factor of 0.96 ± 0.05.

6.4.4 Event selection Summary

From the full dataset collected during Run II, a sample of $\sim 9.1\ fb^{-1}$ of integrated luminosity, passing high-p_T lepton triggers requirements is analyzed. Events are selected using the following criteria:

- at least one reconstructed primary vertex with $z-$position within 60 cm from the nominal interaction point
- a $Z/\gamma^* \rightarrow l^+l^-$ ($l = e, \mu$) boson reconstructed
  - in muon channel requiring two high p_T ($p_T \geq$ 20 GeV/c) muons with opposite charges passing ANN requirements
  - in electron channel asking for one central electron and a second electron that can be central or plug, both with $E_T \geq$ 20 GeV/c and passing ANN requirements
  - with $66 \leq M_{ll} \leq 116$ GeV/c^2
- at least one jet (MidPoint cone size R=0.7) Tight SecVtx tagged with $p_T \geq$ 20 GeV/c, $|Y| \leq 1.5$

Table 6.2 summarizes the observed candidate events for different stages of the event selection.

	Data	
	$Z/\gamma^* \rightarrow \mu^+\mu^-$	$Z/\gamma^* \rightarrow e^+e^-$
N_{Z/γ^*}	303 194	540 734
N_{Z/γ^*-jet}	54 133	84 833
$N_{Z/\gamma^*-b-tag-jet}$	857	1086

Table 6.2: Observed events for the electron and muon channels at different stages of the event selection.

6.5 Background Modeling

Several physic processes have signatures that mimic the $Z/\gamma^* + b-$jet one. These processes include diboson (ZZ, ZW, WW) and top pair production and are modeled using MC samples. Another source of contamination, which could be important in particular in the electron channel when jets are misidentified as electrons, is originated from multi-jet production and W+jets events (QCD). It is estimated using data driven technique.

6.5.1 Diboson and $t\bar{t}$

The diboson and top pair production background are obtained using Pythia MC samples scaled to the data integrated luminosity and normalized to their theoretical cross sections (Table 6.3).

Backgrounds	Monte Carlo	Integrated luminosity
ZZ	Pythia	21518 fb^{-1}
WZ	Pythia	28677 fb^{-1}
WW	Pythia	5967 fb^{-1}
$t\bar{t}$	Pythia	860 fb^{-1}

Table 6.3: MC samples used to estimated the expected background in the analysis.

6.5.2 QCD and $W+$ jets backgrounds

In the muon channel, the QCD, W+jets and DIF backgrounds are evaluated using data-driven techniques. Events are selected using the same muon criteria as described in section 6.4.1 but instead of requiring two muons tracks to be opposite in charge they are required to have the same charge, since the probability to fake a muon is assumed to be charge independent.

For the electron case the evaluation is more involved. QCD multi-jet events and W+jets could fake the signal when hadronic jets are misidentified as electrons. A data-driven method is used to determine these contributions. The method consists in measuring the fake rate, that is the probability of a jet to be identified as an electron in data. The expected background is obtained applying the fake rate to jets in the high-p_T lepton data sample.

Fake rate.

The fake rate is defined as the probability that a jet passes the electron selection and results identified as an electron candidate. This probability is evaluated in a dijet sample where events with more than one electron or $\not{E}_T \geq 15$ GeV are excluded to reject events containing Z/γ^* or W boson candidates. Therefore the fake rate is defined as:

$$fake\_rate = \frac{N_{jets}(that\ pass\ electron\ cuts)}{N_{fakeable}(that\ are\ suitable\ to\ pass\ electron\ cuts)} \tag{6.6}$$

where a fakeable is a jet that satisfies the kinematic requirements of the electron selection and the numerator is the number of such jets passing the electron identification cuts.
A different fake rate is calculated for each electron category (central or plug). The energy of the jet is smeared to better model that of the electron. Due to the differences in the reconstruction algorithms of the jets and electrons, a jet of E_T^{jet} would fake an electron of E_T^{ele} with $E_T^{ele} \leq E_T^{jet}$. The energy scale factors E_T^{ele}/E_T^{jet} are shown in Figure 6.13.

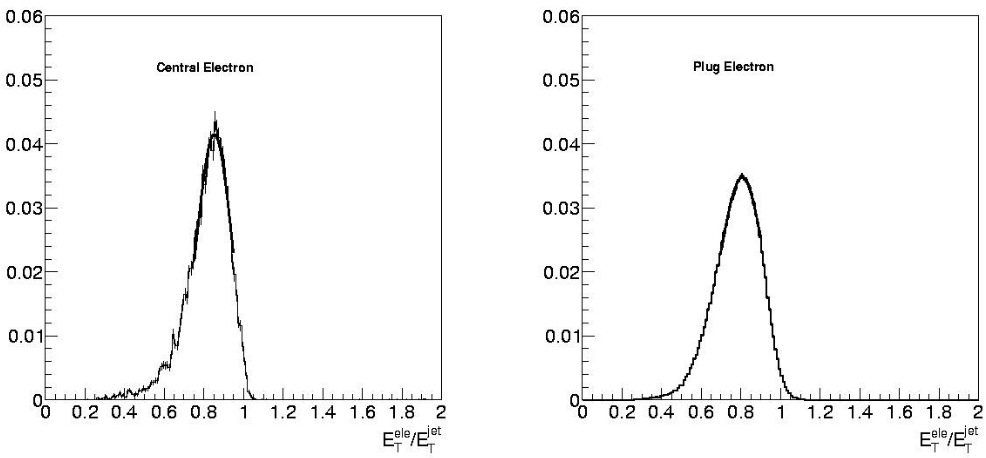

Figure 6.13: Scale factors for central and plug electron fakes. The distributions are fitted with a Gaussian distribution.

Once the fake rates (in Figure 6.14) and scale factors are obtained, the high p_T electron sample is used to estimate the background from QCD and W+jets. Real Z/γ^* events are rejected selecting events with one and only one electron. Every electron-jet pair is considered with a weight equal to the fake rate of the jet, adjusted by the probability of the others to not fake an electron.

6.6 The Z/γ^* inclusive cross section and the Pretag Sample

The accuracy of the Z/γ^* reconstruction and the modeling of signal and backgrounds has been challenged by performing a measurement of the inclusive cross section and validated through the comparison of various kinematic distributions in the pretag (no tagging requirement is applied) sample.

6.6.1 $Z/\gamma^* \to l^+l^-$ inclusive cross section

Measuring the Z/γ^* inclusive cross section is an excellent check to perform in order to validate the understanding of the Z/γ^* selection and reconstruction. The selection of the Z boson therefore follows the same method as for the main analysis while the considered backgrounds

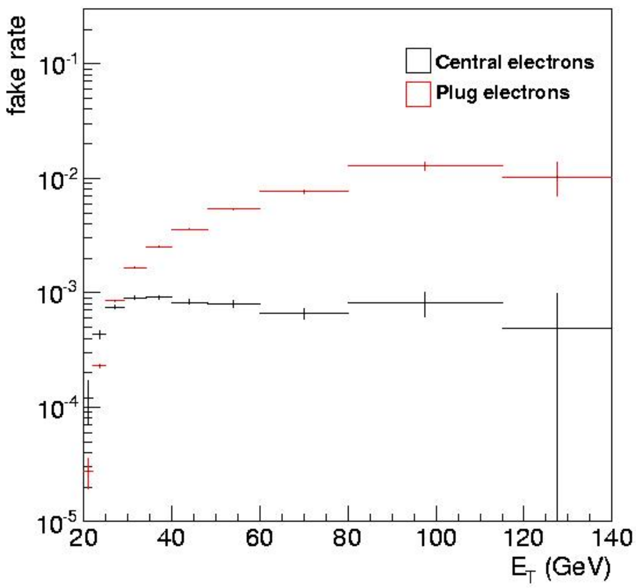

Figure 6.14: Fake rate for central and plug electrons.

are QCD, diboson (WW) and top pair production. The cross section was evaluated in the electron and muon channel as a function of the data period p using the following formula:

$$\sigma_p = \frac{N_p^{data} - N_p^{Bkg} - N_p^{MC-Bkg}}{\mathscr{L}_p \cdot A_p^{data}} \tag{6.7}$$

where N_p^{data} corresponds to the reconstructed Z/γ^* events for the data period p, N_p^{Bkg} the QCD background, N_p^{MC-Bkg} is the background obtained from MC and $\mathscr{L}_p$ is the integrated luminosity for the period. Finally A_p^{data} is the acceptance evaluated from MC and corrected by the trigger and lepton ID scale factors and the primary vertex acceptance, ϵ_p^{vtx}, for each period, according to the equation:

$$A_p^{data} = \sum_i A_{ip}^{MC} \cdot SF_{ip} \cdot \epsilon_p^{vtx} \tag{6.8}$$

where the sum is performed over the Z boson categories.
The inclusive Z/γ^* cross section as a function of the data period p is shown in Figure 6.15 for the muon channel and in Figure 6.16 for the electron channel. A good agreement is seen between periods within the statistical and Luminosity (uncorrelated part only) uncertainties. A drop has been observed in the latest data periods that could be related with the Luminosity measurement but that has negligible effect on the overall cross section.

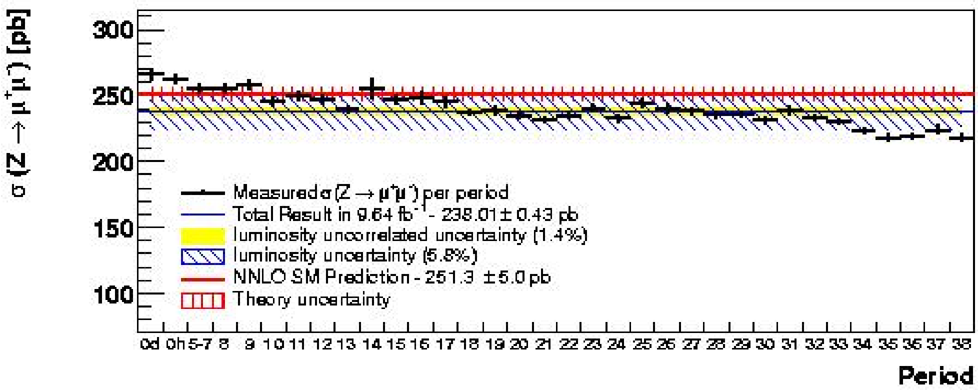

Figure 6.15: $Z/\gamma^* \to \mu^+\mu$ inclusive cross section as a function of data period.

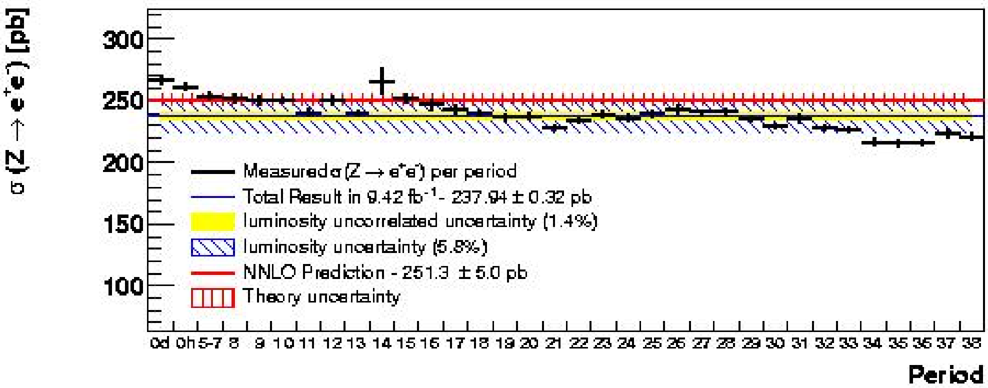

Figure 6.16: $Z/\gamma^* \to e^+e$ inclusive cross section as a function of data period.

6.6.2 Pretag Sample: Data - Monte Carlo Comparison

The pretag sample was used to compare Data and Monte Carlo in order to validate the modeling. Distributions of variables, such as p_T and absolute rapidity of the jets, as well as the invariant mass of the two leptons are presented in Figure 6.17. A good agreement is observed in all cases. For this comparison Alpgen+Pythia MC prediction has been normalized to data.

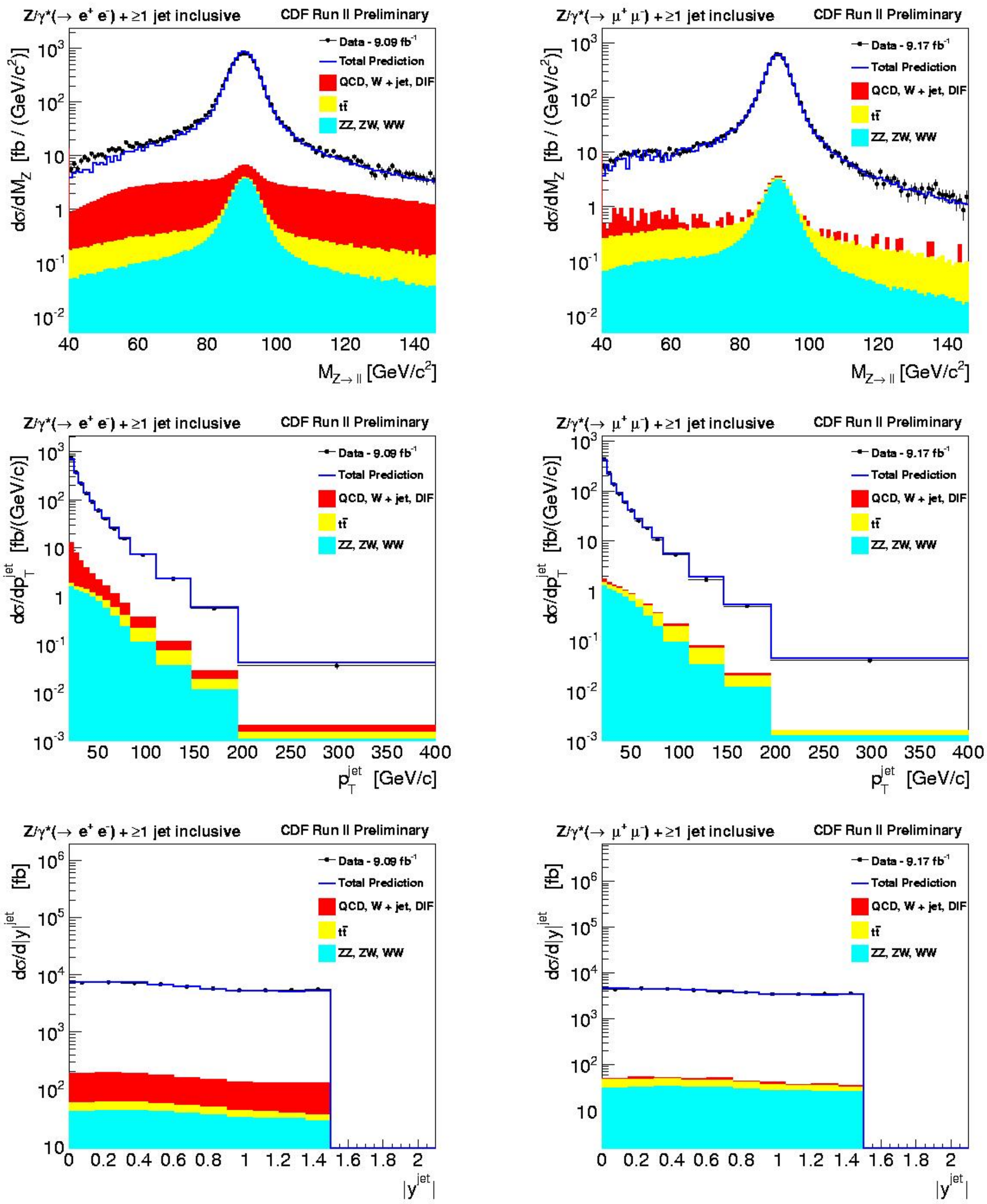

Figure 6.17: Data-MC comparison for M_{Z/γ^*}, p_T and rapidity of jets for electron and muon channel in the pretag sample.

6.7 Composition of b-tagged sample

The tagged jet sample is contaminated by diboson, $t\bar{t}$ and QCD events, however the largest contributions are due to Z/γ^*+jets events where charm and light/gluon jets (LF) are misidentified as $b-$jets by the SecVtx tagger. In order to estimate the fraction of $b-$jets we perform a fit to the invariant mass of the tracks that define the secondary vertex (M_{SecVtx}).

6.7.1 Fitting procedure

As can be seen in Figure 6.18 the mass of the tracks constituting the secondary vertex is related to the mass of the particles decaying at that point. Templates of tagged $b-$jet, $c-$jet, $LF-$jet are built using the Alpgen+Pythia $Z/\gamma^* + Np$ samples following the procedure described below.

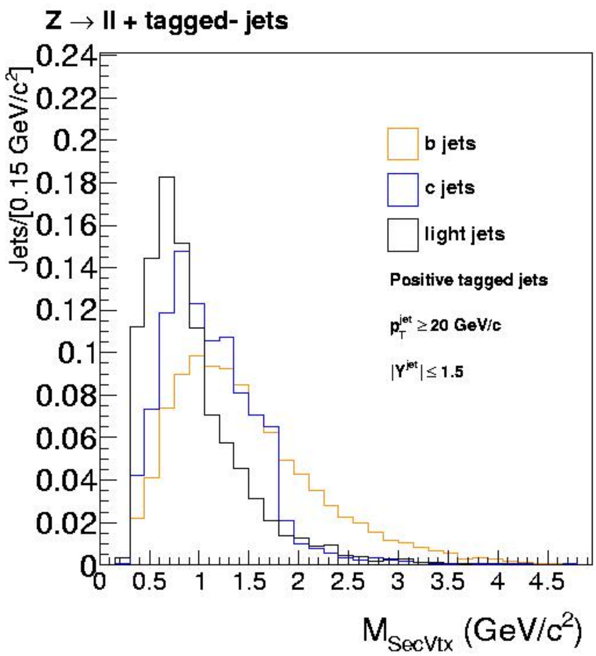

Figure 6.18: Secondary vertex mass templates for Tight SECVTX tagged b, c, LF jets.

Tagged jets have been matched within $\Delta R \leq 0.4$ to either bottom and charm (HF) hadrons. A tagged jet that has not been matched is assigned as a LF jet. To avoid contaminations in the LF sample from heavy flavor, samples that contain HF from the matrix element are vetoed. The main contribution of tags LF jets comes from the $Z/\gamma^* + 1p$ sample.
The feature in the charm shape near M_{SecVtx} = 1.8 GeV/c is attributable to D (mass = 1.865 GeV/c) and $D^{\pm}$ (mass = 1.869 GeV/c^2) vertices for which the invariant mass very nearly reproduces that of the parent. The feature can be seen also in the b shape. These cases correspond to B $\rightarrow D^{\pm}/D^0X$ decays, whose secondary vertex contains tracks from the

tertiary charm state decay.
When building the templates, the contribution from each Alpgen+Pythia sample is weighted according to its prediction. The weighted templates are shown in Figure 6.19 and the normalized ones are in Figure 6.20. Normalized templates show that M_{SecVtx} shapes vary only slightly with the process of origin.

Having found no significative differences between templates built from the electron and muon Alpgen+Pythia samples (Figure 6.21), the final templates have been obtained by merging both. In this way we benefit from a larger statistics which in turn reduce the uncertainties on the $b-$fraction.

Some differences were found on the b template constructed from signal MC and the $t\bar{t}$ samples, which could be attributable to differences in the jet transverse momentum spectra, as it is shown in Figure 6.22. For this reason the $t\bar{t}$ template is added to the signal one normalized to its expected contribution.

Once the templates are built, the components from b, c and LF jets are obtained via a binned maximum likelihood fit. The expected number of total tagged jets in bin i can be expressed as:

$$\mu_i = N_{Tot} \cdot [f_b^{fit} \cdot N_b^i + f_c^{fit} \cdot N_c^i + f_{LF}^{fit} \cdot N_{LF}^i] \tag{6.9}$$

where N_j^i is the normalized contribution of flavor j ($j = b, c, LF$) given by the M_{SecVtx} template, f_j is the fit fraction for species j and N_{Tot} is the number of tagged jets in data sample. The sum of the fit fractions is constrained by:

$$f_b^{fit} + f_c^{fit} + f_{LF}^{fit} = 1 \tag{6.10}$$

The Poisson probability $P(n_i|\mu_i)$ of observing n_i tagged jets in bin i of a secondary vertex distribution given μ_i, is:

$$P(n_i|\mu_i) = \frac{e^{-\mu_i} \cdot \mu_i^{n_i}}{n_i!} \tag{6.11}$$

Therefore the Likelihood function $\mathscr{L}$ can be constructed as:

$$\mathscr{L} = \prod_{i=1}^{N_{bins}} P(n_i|\mu_i) = \prod_{i=1}^{N_{bins}} \frac{e^{-\mu_i} \cdot \mu_i^{n_i}}{n_i!} \tag{6.12}$$

for the N_{bins} of the M_{SecVtx} templates.
The fit fractions are obtained by maximizing the likelihood:

$$\ln(\mathscr{L}) = \ln\left(\prod_{i=1}^{N_{bins}} \frac{e^{-\mu_i} \cdot \mu_i^{n_i}}{n_i!}\right) = \sum_{i=1}^{N_{bins}} [-\mu_i + n_i \ln \mu_i + const] \tag{6.13}$$

The MINUIT package implemented in ROOT is used for this purpose.
The result of the fit is shown in Figure 6.23 where the fraction of $b-$jets obtained is 0.46 ± 0.03, thus the number of $b-$tagged jets in the data are 903 ± 78.

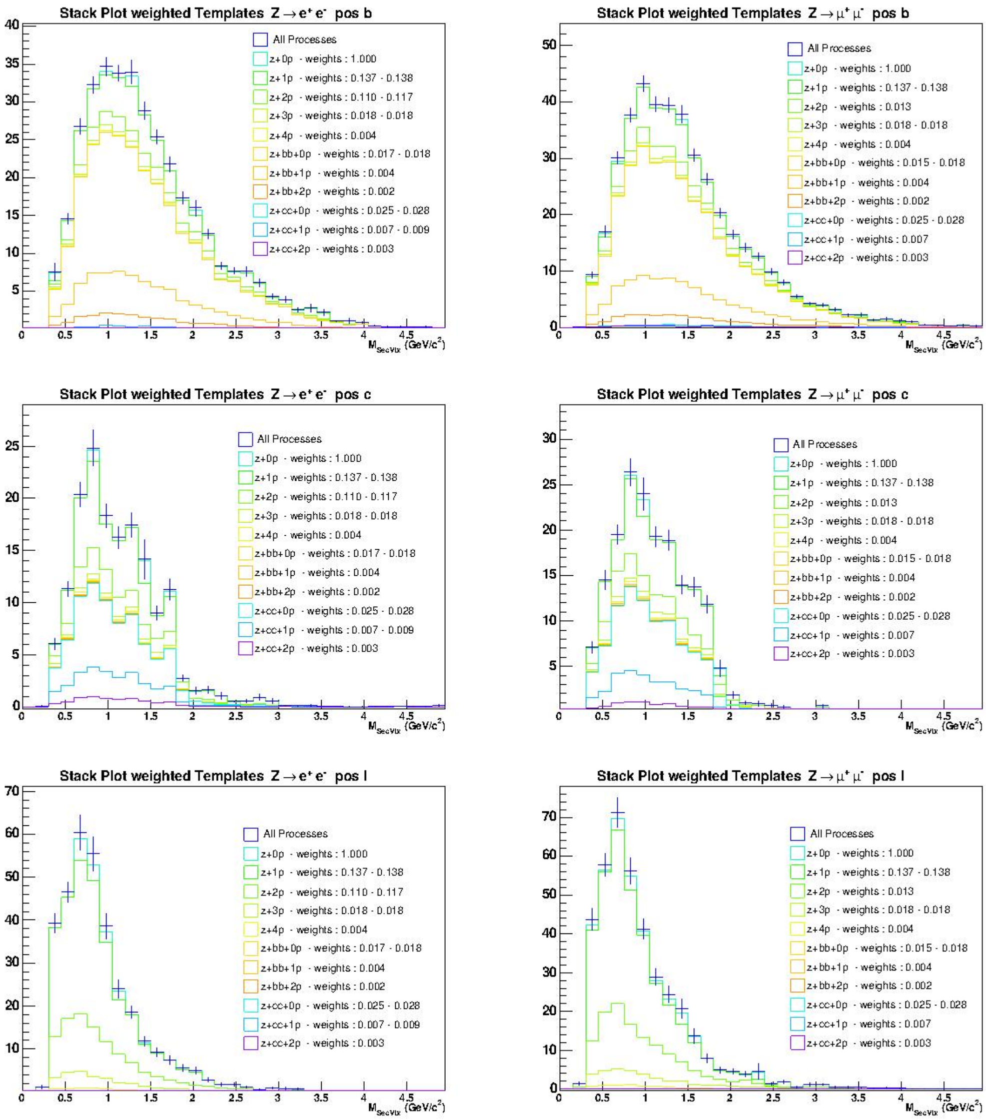

Figure 6.19: Secondary vertex mass templates for Tight SECVTX tagged b, c, LF jets. Plots show the contribution from each process and its corresponding weight.

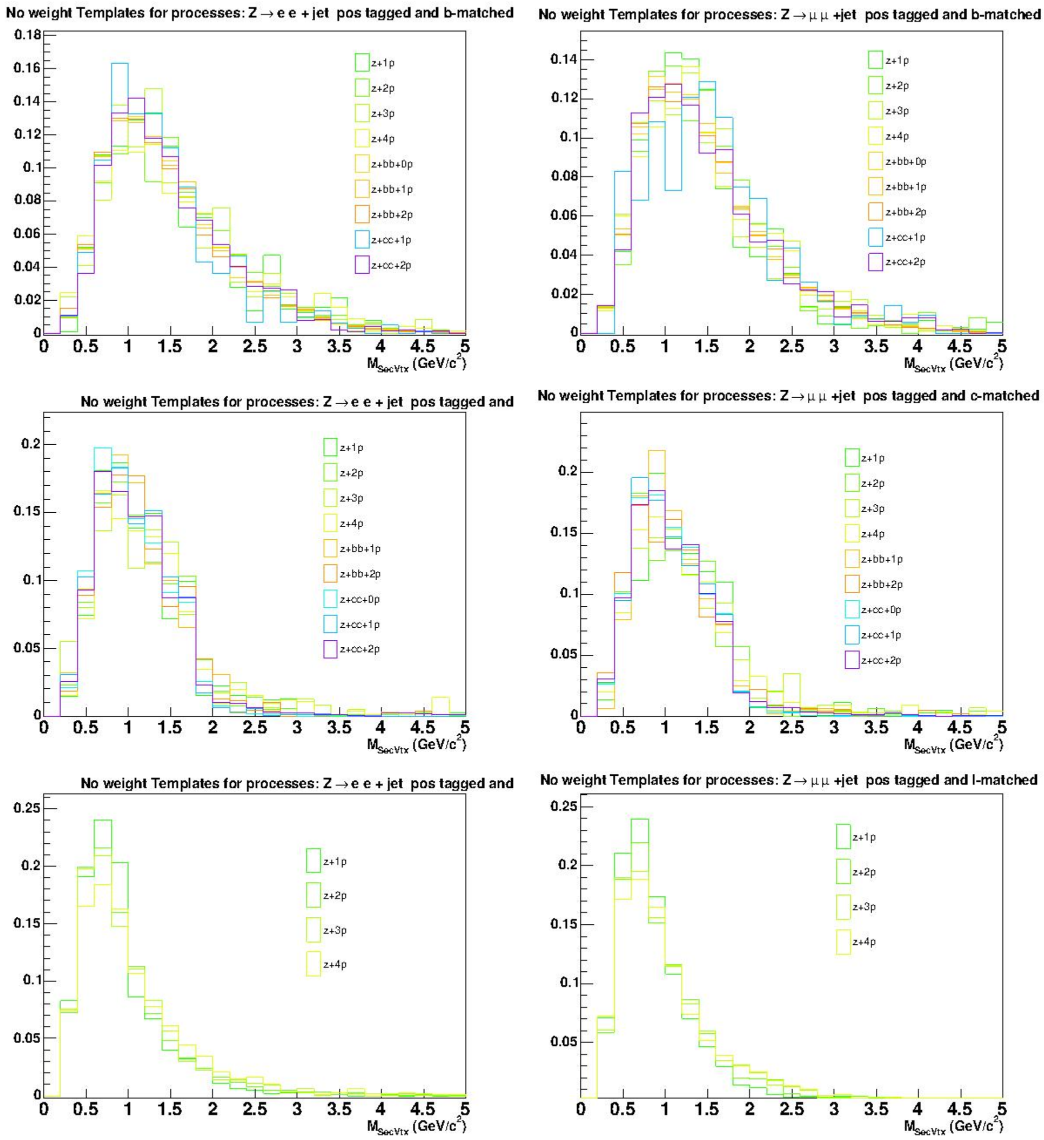

Figure 6.20: Secondary vertex mass templates for Tight SECVTX tagged b, c, LF jets for different processes, normalized to 1.

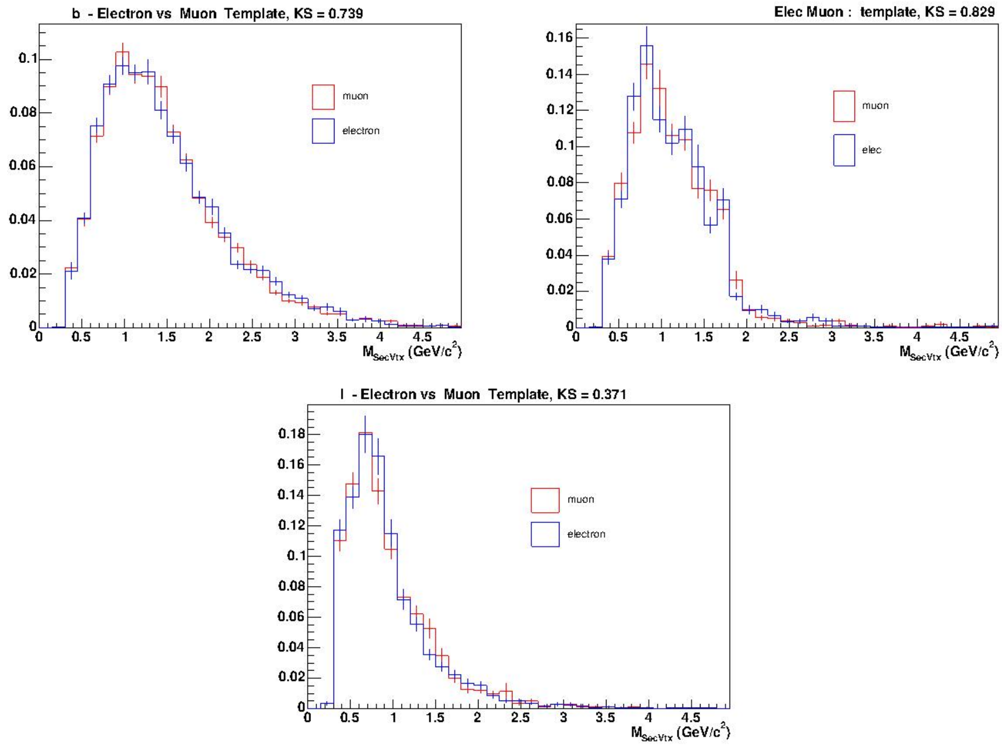

Figure 6.21: Comparison between electron and muon channel SecVtx templates for the b, c and LF jet flavors. The Kolmogorov-Smirnov statistical test (KS) on the top of the plots shows that there is a good agreement.

6.7.2 Bias Checks

The fit procedure was validated using pseudo-experiments (PE). Pseudodata are drawn from the various species of M_{SecVtx} templates with the same statistics as data for a particular choice of $b/c/LF$ fractions. The new M_{SecVtx} distribution, built from the pseudodata, is fitted with the same procedure described above. For each PE, f_b is obtained and histograms of the fitted f_b, its uncertainty and its pull $((f_b^{fit} - f_b^{input})/\sigma_{f_b}^{fit})$ are filled. The procedure is repeated for 5000 pseudo-experiments.
The pull distribution for the scenario $b/c/LF = 47/15/38$ is shown in Figure 6.24. The width of the pull, RMS ~ 1.0, as expected for properly defined uncertainties. No bias is observed in the mean of the distribution. The dependence on the input fraction was studied: a linear dependence, which shows no bias, is observed in Figure 6.25 where the value of the measured fractions is plotted as a function of the input.

6.7.3 Background Expectation

As explained previously, background contributions are mainly due to QCD (inclusive jets, $W + jets$ and decay in flight) events and processes such as diboson (WW, ZZ, ZW) and

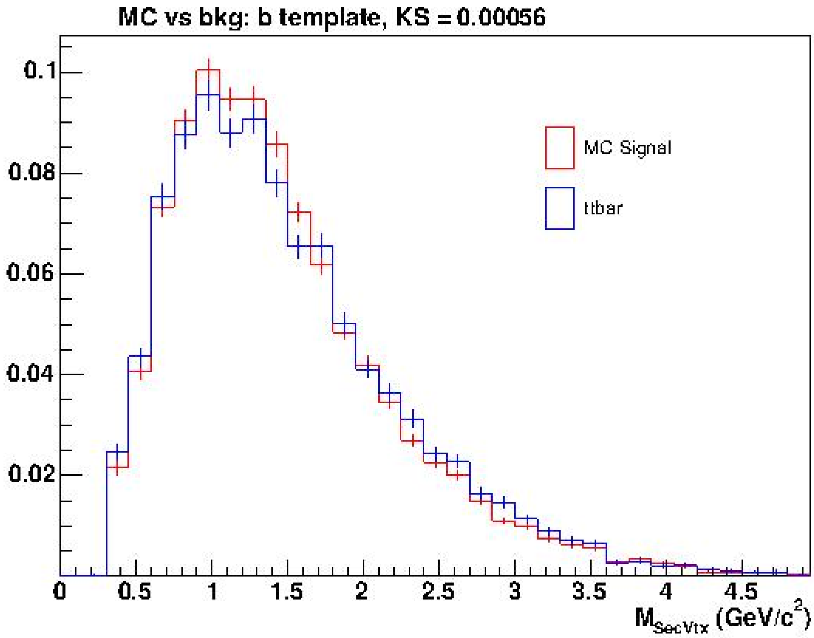

Figure 6.22: b SecVtx Mass template comparison between MC signal and $t\bar{t}$.

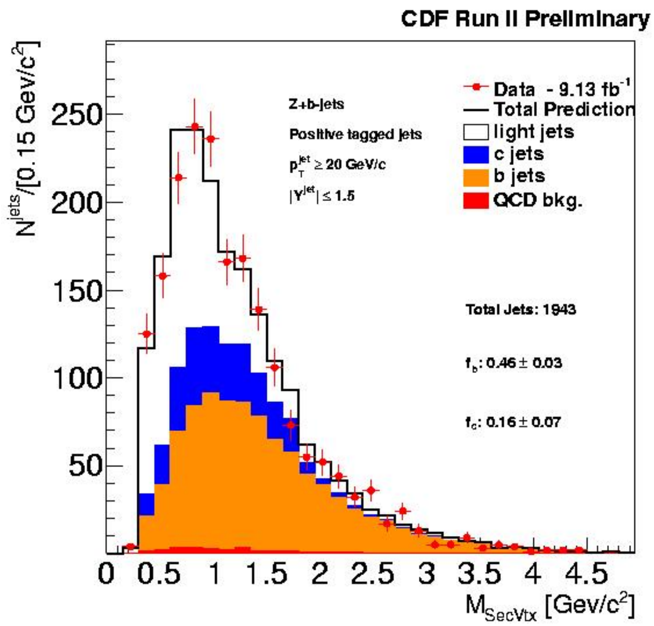

Figure 6.23: SecVtx Mass distribution for $Z/\gamma^* \to l^+l^-$. In colors is shown the contributions from each flavor (as result of the fit)

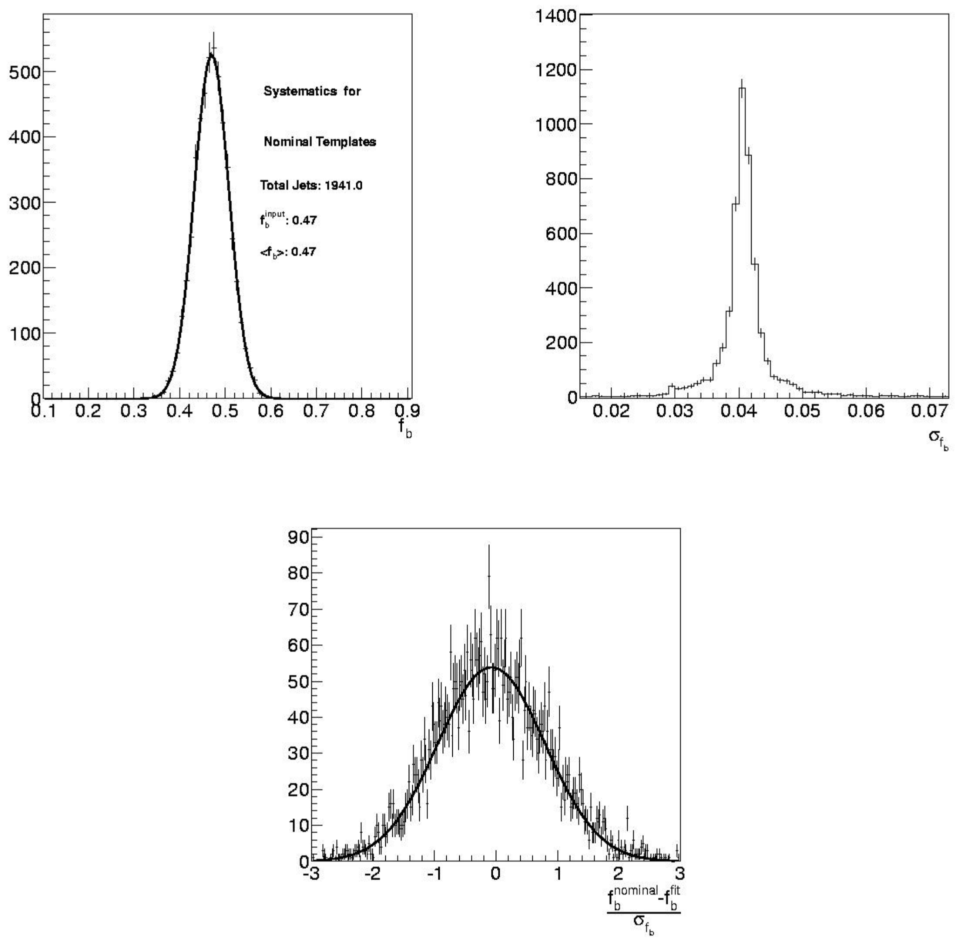

Figure 6.24: Fraction of $b-$jet, its uncertainty (σ_{f_b}) and pull obtained from pseudo-experiments for the scenario in the data, i.e. b/c/LF=0.47/0.15/0.38.

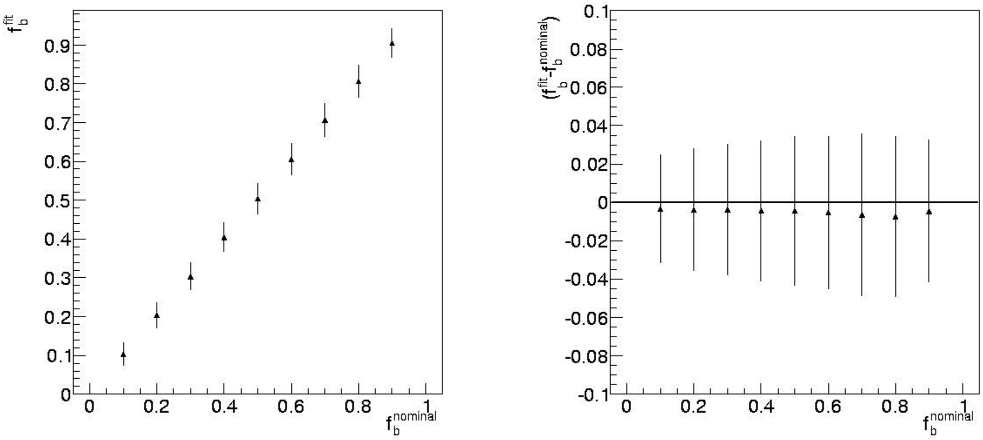

Figure 6.25: Results from pseudo-experiments using different input scenarios. Left: PE f_b mean as a function of input f_b. Right: residual means as a function of input f_b, the uncertainty is coming from the width of the Gaussian centered in f_b.

$t\bar{t}$ jets. For the case of Z/γ^* and Z/γ^*+jets cross sections, the expected backgrounds are subtracted from the number of observed data events passing the corresponding selection requirements. In the case of the $b-$tagged jet sample, the predicted number of $b-$jets from tagged diboson and top pair production (Table 6.4) are subtracted from the fitted number of $b-$jets. The background originated from QCD (fakes) is included directly in the SecVtx Mass fit through a template obtained from data by weighting events by the fake rate (section 6.5.2).
Background expectations are summarized in Tables 6.4 and 6.5.

process	bkg $Z/\gamma^* \to \mu^+\mu^-$	process	bkg $Z/\gamma^* \to e^+e^-$
dibosons	12.5 ± 2.5	dibosons	13.3 ± 3.0
$t\bar{t}$	56.5 ± 5.4	$t\bar{t}$	58.8 ± 5.9
total	69.4 ± 5.9	total	73.2 ± 6.6

Table 6.4: The background contributions for $Z/\gamma^* + b$ tagged jets in muon and electron channel.

6.8 Acceptance

The acceptance for each process considered in this analysis, inclusive Z/γ^* production, Z/γ^*+ jets and $Z/\gamma^* + b-$jets, was evaluated separately for the muon and electron channel and later

	Data		Fakes		MC Bkg.	
	muon	electron	muon	electron	muon	electron
N_{Z/γ^*}	303 194	540 734	115	4452	617 ± 64	718 ± 77
N_{Z/γ^*-jet}	54 133	84 833	43	1465	574 ± 60	671 ± 72
$N_{Z/\gamma^*-b-tag-jet}$	857	1086	1	27	69.4 ± 5.9	73.2 ± 6.6

Table 6.5: Events observed in data and expected backgrounds for all processes in the electron and muon channels

combining weighting by its corresponding integrated luminosity. They are extracted from MC and corrected by the SF to take into account differences between data and MC for the trigger and lepton ID efficiencies. Details on the calculation are described below and results are shown in Table 6.7.

Acceptance for the Z/γ^* inclusive cross section

It is evaluated using the Pythia Z/γ^* inclusive sample. The numerator is defined as the number of the events that pass the Z/γ^* selection cuts while the denominator is given by the number of generated events that have a Z/γ^* with M_Z between 66 and 116 GeV/c^2

$$A_{Z/\gamma^*} = \frac{N\ Z/\gamma^*\ reconstructed}{N\ Z/\gamma^*\ generated\ within\ mass\ range\ cut}$$

Acceptance for Z/γ^* + jets

For the calculation of Z/γ^*+jets acceptance, we considered the same selection as for the Z/γ^* inclusive cross section to which we have added the requirement of the presence of at least a jet that at both, calorimeter and hadron level, should pass the requirements $p_T \geq 20$ GeV/c and $|Y| \leq 1.5$.

$$A_{Z/\gamma^*-jet} = \frac{N\ Z/\gamma^*\ reconstructed\ +\ calorimetric\ jets\ in\ phase\ space}{N\ Z/\gamma^*\ generated\ within\ mass\ range\ cut +\ hadron\ level\ jets\ in\ phase\ space}$$

Acceptance for $Z/\gamma^* + b-$jets

In this case the acceptance is obtained from the ratio between the number of $b-$tagged calorimeter jets found in events with a reconstructed Z/γ^* passing selection requirements and the number of $b-$matched hadron jets in events generated with a Z/γ^* passing selection requirements.

$$A_{Z/\gamma^*\_btag\_jet} = \frac{N\ Z/\gamma^*\ reconstructed + calorimetric\ jets\ in\ phase\ space\ tagged\ positively\ and\ b-matched}{N\ Z/\gamma^*\ generated\ within\ mass\ range\ cut + hadron\ level\ jets\ in\ phase\ space\ b-matched}$$

Process	$Z/\gamma^* \to e^+e^-$	$Z/\gamma^* \to \mu^+\mu^-$
A_{Z/γ^*}	0.2455 ± 0.0002	0.1354 ± 0.0001
A_{Z/γ^*+jet}	0.2837 ± 0.0007	0.1915 ± 0.0005
$A_{Z/\gamma^*+b\_tag\_jet}$	0.0688 ± 0.0008	0.0554 ± 0.0007

Table 6.6: Acceptance table for electron and muon channel for different processes. The increase seen on the muon acceptance with respect to the electron one when adding the requirement of the presence of a jet in the event, is due to changes on the Z/γ^* rapidity distribution, as it becomes predominantly central.

6.9 Systematics

Sources of systematic uncertainties may affect the analysis by altering the shape of the M_{SecVtx} templates, the acceptances or background rates. Their contributions to the uncertainty on the cross section measurement are summarized in Table 6.8 and their estimation is discussed below.

6.9.1 Secondary Vertex Mass shape systematics

Since templates are built using MC, possible sources of mismodeling have been analyzed. For each of them new templates are built to take into account the corresponding effect in M_{SecVtx}. Contributions to the uncertainty are due to:

- **Track reconstruction inefficiency**: A track reconstruction inefficiency of 3 % was observed in MC [4]. New templates are built by randomly rejecting 3 % of tracks and recomputing the value of M_{SecVtx}. The differences between the templates are shown in Figure 6.26.

- **Single/Double B/C hadron in a jet**: In Alpgen the fraction of $b\bar{b}$ to b jets (and $c\bar{c}$ to c jets) is 0.23 (0.68). However previous studies[4] have presented differences of a factor of 3 (2) times. In order to take into account this effect we built the new b and c templates by weighting Alpgen events in such a way that the double fraction varies between 0 to 0.7 for b and between 0 to 1.36 for c. Figure 6.27 shows the modified templates.

- **Light flavor template systematic** The default light flavor template is made of positively tagged jets that have not been matched to any HF hadron in $Z/\gamma^* + Np$ Alpgen+Pythia MC samples.
  For mistag jets, the probability to be positively or negatively tagged is expected to be approximately the same. In order to evaluate a systematic uncertainty, a template from negatively tagged jets from data (mostly populated by mistags) is built. The data

sample utilized is defined requiring a high-p_T lepton and low $\not\!\!E_T$ (Figure 6.28).

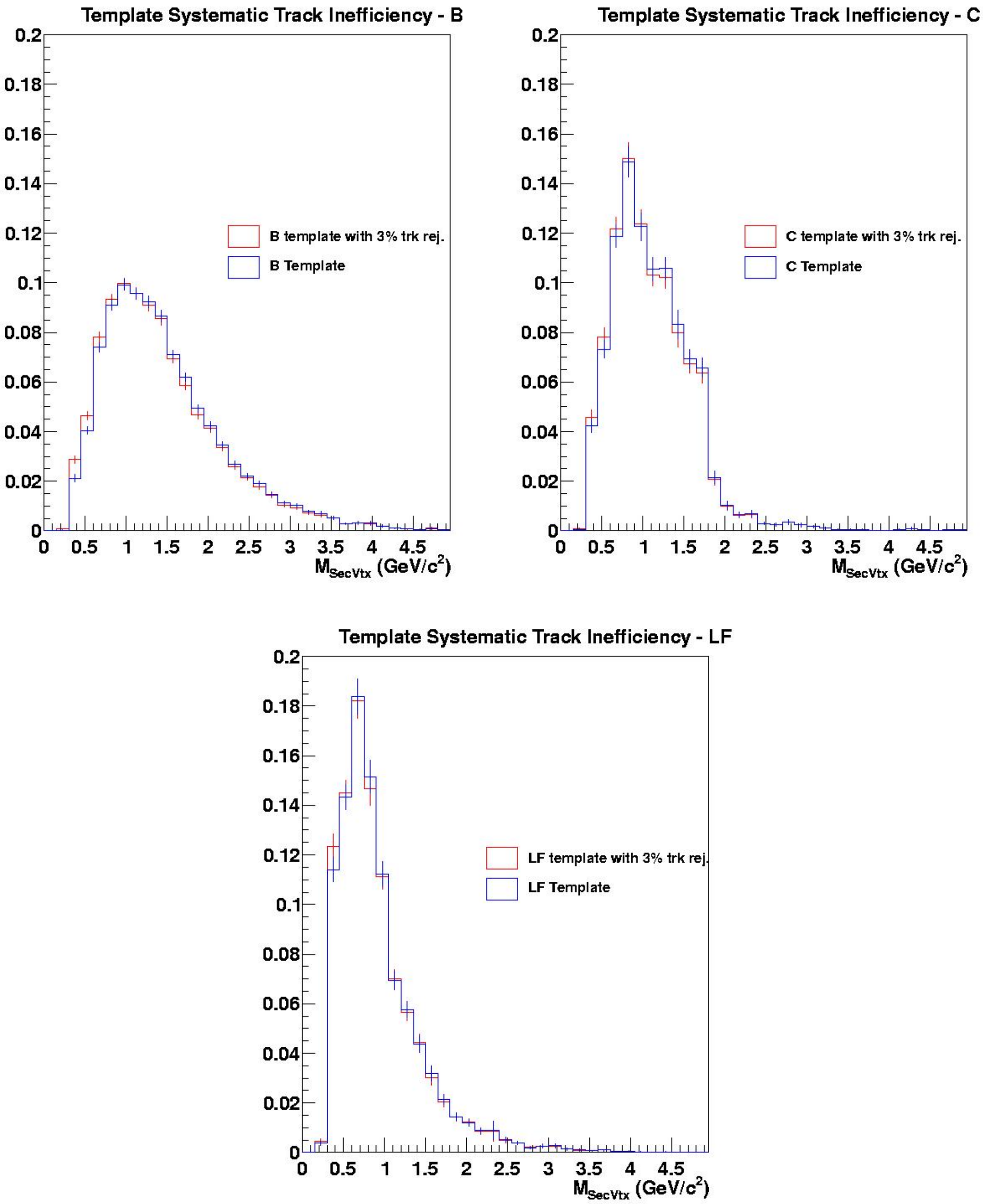

Figure 6.26: SecVtx Mass templates built with and without the 3% track rejection.

The method to evaluate these systematics consists in performing pseudo-experiments (PE), building pseudo-data from the new templates and fitting them using the nominal ones. For example, let us consider the track reconstruction inefficiency systematic, the procedure is the

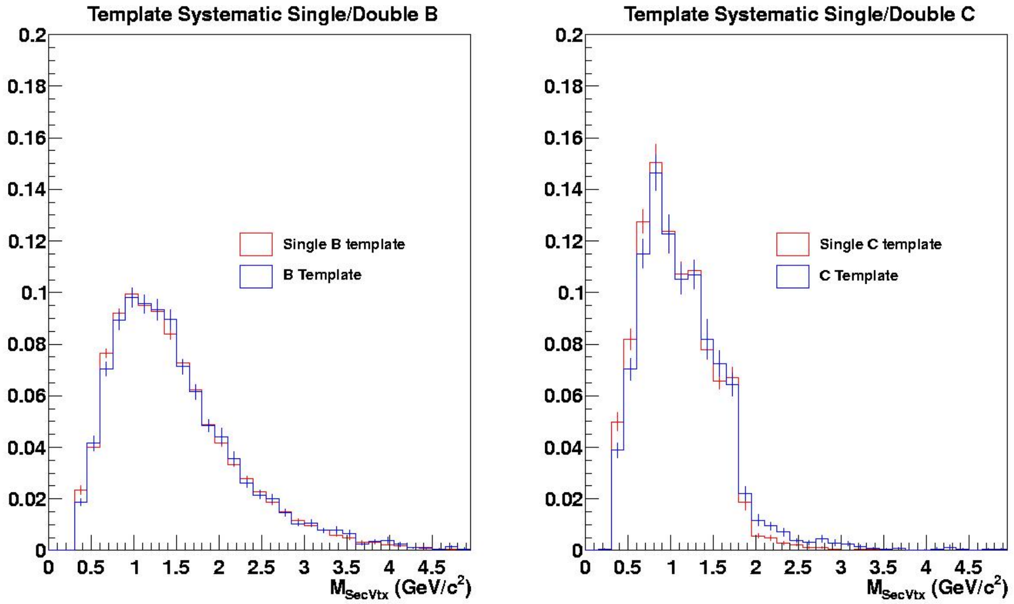

Figure 6.27: SecVtx Mass templates comparison for Single/Double b/c hadron in tagged jets. The fraction of 2b jets to 1b jets in the B(C) Template is 0.7(1.36).

following:

- build pseudo-data from the new M_{SecVtx} template, that includes the rejection of 3 % of the tracks
- fit pseudo-data using the original templates and find f_{b-syst}
- repeat the procedure 5000 times
- assign as systematic the shift between the mean value of the f_{b-syst} distribution and the nominal one obtained from PE drawn from nominal templates[5].

6.9.2 Bootstrap

Uncertainties due to the limited MC statistics have been also estimated using the bootstrapping technique. This method consists in using the MC dataset to create multiple datasets by random selection from the same parent distribution. f_{b-syst} distributions are obtained using these new datasets. The RMS of the f_{b-syst} mean distribution is a measure of the uncertainty due to the limited MC statistics. We verified that these uncertainties are negligible. However it was not the case for the first attempt to build a negative tagged jets data template. The

[5]For the single/double b/c the half difference obtained by varying the $b\bar{b}/b$ ($c\bar{c}/c$) ratio from 0 to 3 (2) is used as systematic uncertainty.

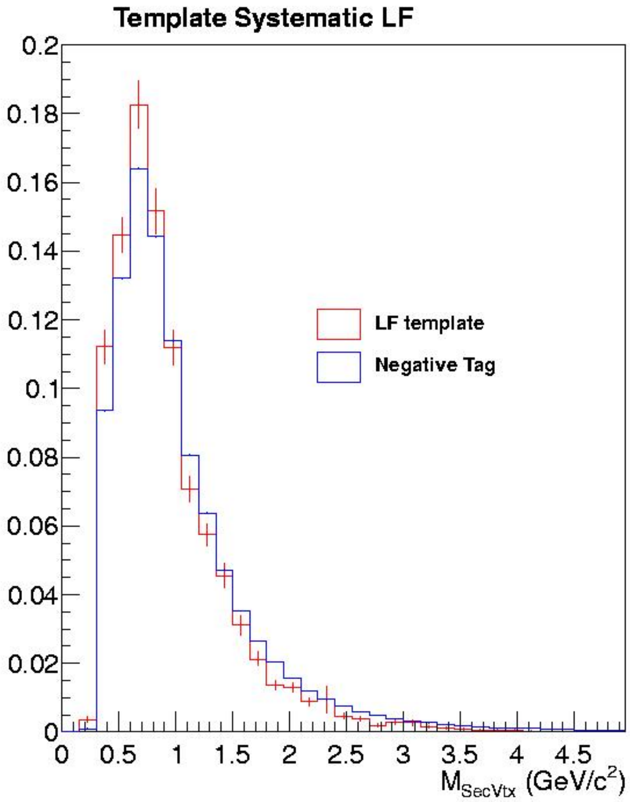

Figure 6.28: Comparison of SecVtx Mass templates constructed using LF MC jets and Negative tags from data

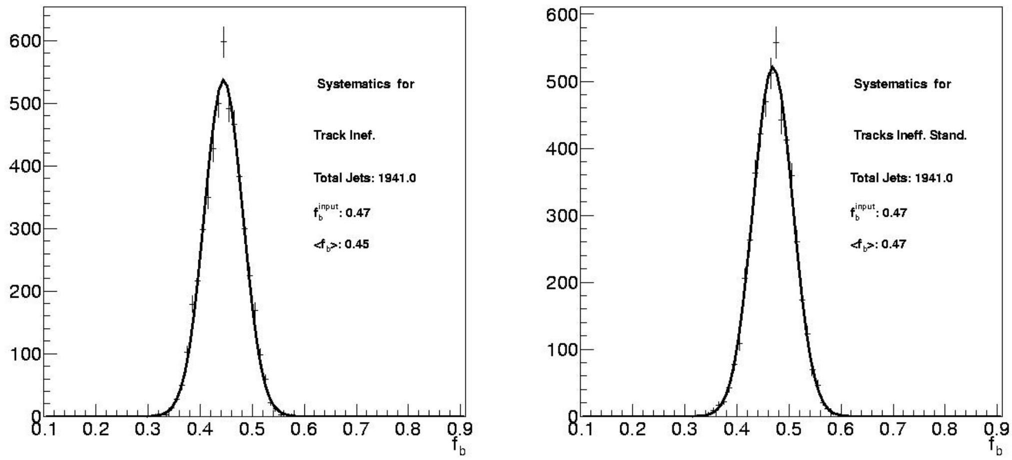

Figure 6.29: Example of the template systematic uncertainty evaluation where are presented f_b distributions for PE using nominal and track reconstruction inefficiency templates. The shift in $< f_b >$ is used as systematic.

first sample used was the Z/γ^*+ jets sample but the statistics proved to be too low. A new template was obtained from a larger dataset as explained in the previous subsection.

6.9.3 Acceptance systematics

The acceptance in the cross section measurement is affected by the JES and the $b-$tag SF uncertainties.
The uncertainty on the jet energy corrections is described in Chapter 5. These corrections are designed to properly scale back to particle level the measured energy of jets. To evaluate this uncertainty, the jet energies are shifted in the MC by $\pm 1\sigma$ for each of the jet energy corrections individually. The uncertainty is assigned as half the difference between the two new acceptance values. The total jet energy scale uncertainty is taken as the quadrature sum of the uncertainty from all 3 jet energy corrections. The relative effect on $A_{Z/\gamma^*+b-jet}$ is of 2% while in the case of A_{Z/γ^*+jet} is larger, $\sim 8\%$, due to differences on the transverse momentum spectra.

The second source of systematic error in the acceptance rises from the imprecise knowledge of the $b-$tag efficiency in data. This uncertainty is introduced in the measurement through the error of the b-tag SF (0.96 ± 0.05). Other systematics that affects the acceptances are the errors on the trigger, lepton ID and z vertex efficiency, but these are negligible and canceling in the ratio.
The final acceptances uncertainties are found in the table 6.7.

Process	$Z/\gamma^* \to e^+e^-$ tag(%)	$Z/\gamma^* \to e^+e^-$ JES(%)	$Z/\gamma^* \to \mu^+\mu^-$ tag(%)	$Z/\gamma^* \to \mu^+\mu^-$ JES(%)
A_{Z/γ^*+jet}	/	9.3	/	8.7
$A_{Z/\gamma^*+b\_tag\_jet}$	5.2	2.2	5.2	1.7

Table 6.7: Systematic uncertainties for the acceptances due to jet energy scale (JES) and tag efficiency (tag)

6.9.4 Background subtraction systematics

A systematic error was estimated due to the background normalization uncertainty. For backgrounds evaluated from MC, the uncertainty on the cross section is the main component ($\sim$ 20% for diboson and $\sim$ 10% for top) and the remaining comes from the luminosity uncertainty ($\sim$ 5.8%). However, the overall effect in the $b-$jet cross section is less than 0.1 %.
For data-driven backgrounds, though a 100 % uncertainty is applied to the background estimation in the muon case, the final effect is negligible. For electrons, distributions in Figure 6.14 are fitted and an error of 15 % is applied to cover possible deviations from the fit but also in this case the effect is small.

6.9.5 Summary of systematics uncertainties

The total uncertainty is obtained summing quadratically each contribution in Table 6.8 and is $\sim$ 13% for the ratio with respect to the Z/γ^* inclusive cross section, and 15 % for the ratio with respect to Z/γ^*+jets. The systematics is comparable to the statistical uncertainties.

Systematics	$\frac{\sigma_{Z\_bjet}}{\sigma_Z}$ (%)	$\frac{\sigma_{Z\_bjet}}{\sigma_{Zjet}}$ (%)
Acceptance Systematics		
Jet Energy Scale abs	1.1	2.9
Jet Energy Scale mi	1.5	6.2
Jet Energy Scale eta	0.6	2.0
b tag efficiency	5.2	
Templates Systematics		
Light Templates - data	9.5	
Double 1b/2b	1.6	
Double 1c/2c	2.6	
Tracks Inefficiency	7.3	
Others		
Background subtraction	0.07	0.07
Total	13.4	15.2

Table 6.8: Summary of the systematics that affects the cross section measurement.

7 $Z/\gamma^* + b-$jet Differential Cross Sections

The $Z/\gamma^* + b-$jet cross section ratios are also measured differentially as a function of jet transverse momentum and jet rapidity. This chapter describes how the measurement was performed.

7.1 Measurement definition

The strategy utilized for these measurements is the same as for the integrated one (described in Chapter 6), but in this case data is divided in p_T^{jet} and $|Y^{jet}|$ bins and for each bin the complete analysis chain is repeated, including a reevaluation of the systematic uncertainties. The bin size has been optimized for the statistical uncertainty.
Differential cross sections normalized to the inclusive Z/γ^* cross section are defined as:

$$\frac{d(\sigma_{Z/\gamma^*+b-jet}/\sigma_{Z/\gamma^*})}{d\alpha} = U^{cal}_{had}(Z/\gamma^*+b-jet)(\alpha) \times \frac{N^{data}_{Z/\gamma^*+b-jet} - N^{bkg}_{Z/\gamma^*+b-jet}}{\frac{N^{data}_{Z/\gamma^*} - N^{bkg}_{Z/\gamma^*}}{A_{Z/\gamma^*}}} \frac{1}{\Delta\alpha} \tag{7.1}$$

where:

- $\alpha = p_T^{jet}, Y^{jet}$
- $N^{data(bkg)}_{Z/\gamma^*+b-jet}$ and $N^{data(bkg)}_{Z/\gamma^*}$ are the number of $Z/\gamma^*+b-jet$ and Z/γ^* in data (expected background)
- A_{Z/γ^*} is the Z/γ^* acceptance times the event selection efficiency
- $U^{cal}_{had}(\alpha)$ the unfolding factors.

In order to remove effects from the experimental environment, the measurement is unfolded back to hadron level. The Unfolding factors, $U^{cal}_{had}(\alpha)$, are derived for each distribution using Monte Carlo and applied bin-by-bin.

7.2 Sample composition

Events are selected following the same prescription described in Chapter 6, but in this case divided in jet p_T and jet rapidity bins. Table 7.1 shows the number of tagged jets and expected background for each bin in electron and muon channels.

	$Z/\gamma^* \to \mu^+\mu^-$			$Z/\gamma^* \to e^+e^-$		
p_T bins						
	data	fake	bkg	data	fake	bkg
20 - 27 GeV/c	174	0	3.4 ± 0.5	222	5.1 ± 1.6	4.1 ± 0.6
27 - 35 GeV/c	155	0	5.9 ± 0.8	224	5.4 ± 1.6	6.5±0.9
35 - 45 GeV/c	159	1 ± 1	9.8 ±1.2	193	4.8± 1.5	10.0 ± 1.3
45 - 60 GeV/c	121	0	15.0 ±1.8	196	4.7 ± 1.4	15.9±1.9
60 - 100 GeV/c	167	0	25.2 ±2.8	175	5.3 ± 1.6	25.8±3.0
$\lvert Y^{jet}\rvert$ bins						
0.0 - 0.3	233	1 ± 1	19.9 ±2.3	279	7.1 ± 2.2	21.3± 2.5
0.3 - 0.6	214	0	19.2± 2.5	265	7.6 ± 2.3	20.4± 2.4
0.6 - 1.0	258	0	19.6 ±2.4	335	8.1 ± 2.4	20.9± 2.5
1.0 - 1.5	152	0	10.5± 1.3	207	4.3 ± 1.4	10.5 ±1.5

Table 7.1: Number of observed tagged jets and expected background contributions. An error of 100 % is assigned to the negligible fake muon background. For the electrons the uncertainty on the fakes is coming from the fit of the fake rate.

The amount of $b-$tagged jets is obtained via a fit of the M_{SecVtx} distribution. Templates are created for each bin, combining electron and muon channel, and the fit is then performed via a maximum binned Likelihood. Results of the fit, summarized in Table 7.2, are presented as function of p_T jet in Figures 7.1, 7.2, 7.3 and for different rapidity bins in Figure 7.4, 7.5.

p_T bins	Fit result with Stat. uncert.
20 - 27 GeV/c	251±41
27 - 35 GeV/c	184±32
35 - 45 GeV/c	200±35
45 - 60 GeV/c	195±23
60 - 100 GeV/c	129±38
$\lvert Y^{jet}\rvert$ bins	
0.0 - 0.3	238±38
0.3 - 0.6	249±38
0.6 - 1.0	295± 43
1.0 - 1.5	188± 28

Table 7.2: Number of fitted b tagged jets.

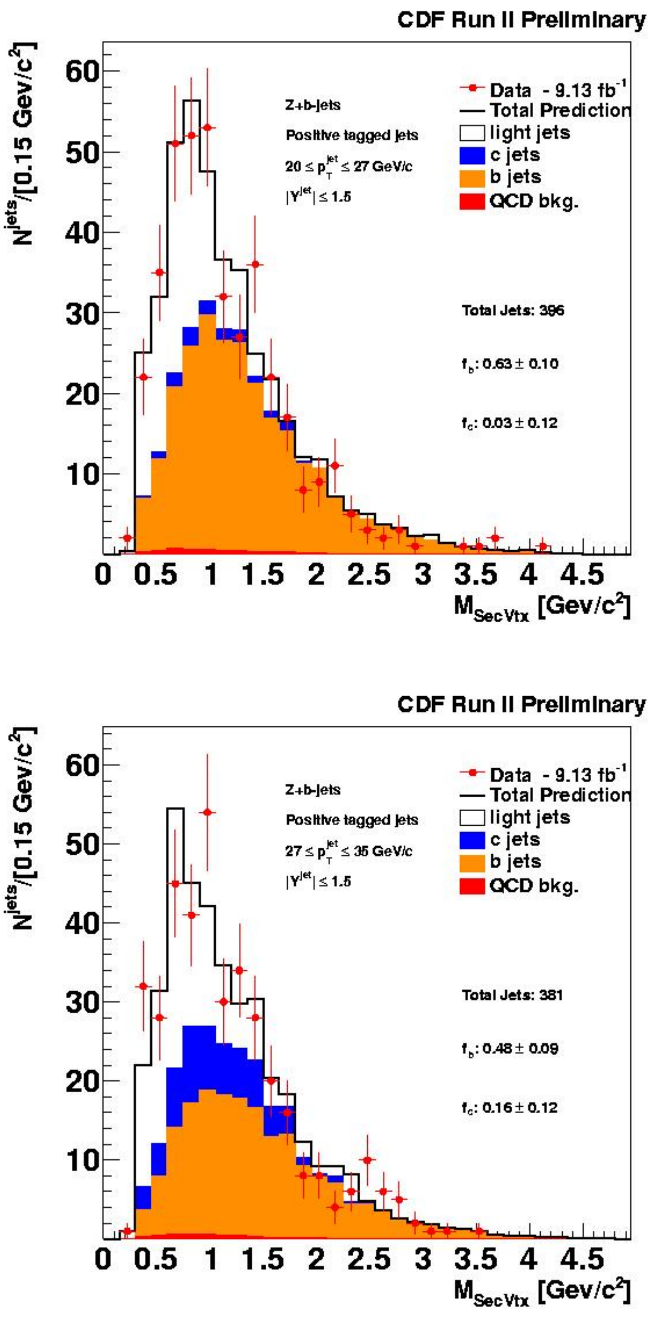

Figure 7.1: Secondary vertex mass fit results for first two p_T bins.

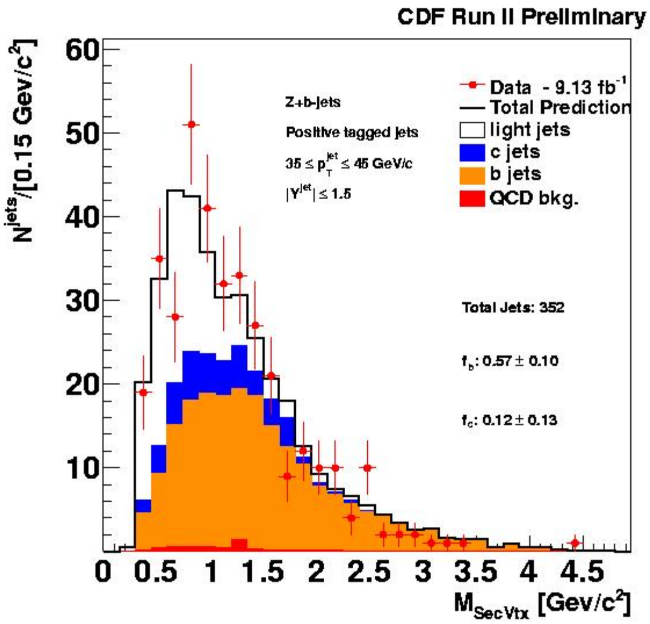

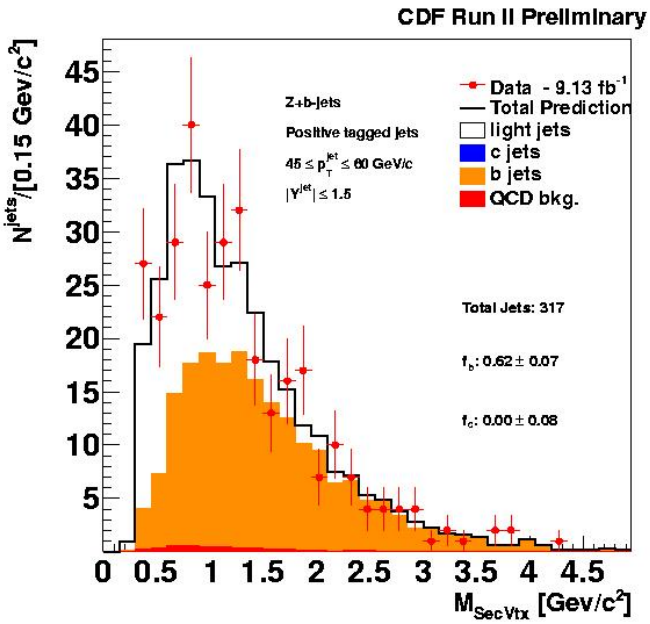

Figure 7.2: Secondary vertex mass fit results for third and fourth p_T bins.

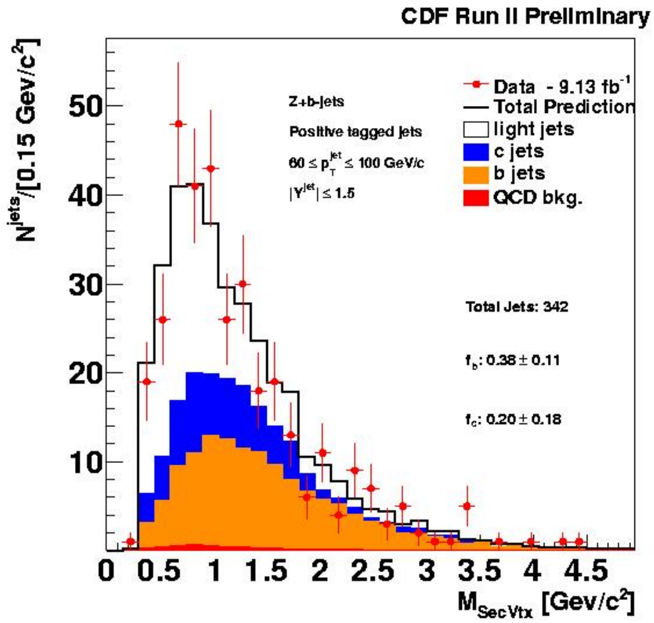

Figure 7.3: Secondary vertex mass fit results for the fifth p_T bin.

7.3 Unfolding

Once the fit is performed and background jets subtracted, the results are unfolded back to hadron level. Corrections factors are estimated from Monte Carlo using the Alpgen+Pythia samples and are defined as follows:

$$U^{cal}_{had}(\alpha) = \frac{N\left[Z/\gamma^{*}[particle\ \ level] + b - jet[particle\ \ level]\right]}{N\left[Z/\gamma^{*}[reconstructed] + b - tagged - jet[calorimeter]\right]}|_{MC} \tag{7.2}$$

Distributions for each variable α are obtained at detector and hadron level and the ratio performed bin-by-bin. The Z/γ^* selection kinematic cuts are the same for both levels and are described in Chapter 5. Jets are matched to b hadrons and divided in p_T ($|Y|$) bins, following the thresholds in Table 7.1. The same jet p_T (Y) cuts are applied to detector and hadron level. Therefore, unfolding factor corrects for the small migration between bins due to experimental resolution and for the detector acceptance.
Figure 7.6 shows the inverse of the unfolding factors as function of jet p_T and jet rapidity.

7.4 Systematic Uncertainties

As explained previously the main systematic uncertainty is due to M_{SecVtx} template shape mismodeling in MC. Also here the PE technique is used to evaluate these effects. Pseudodata is built using templates modified to include each systematic effect and the fraction of $b-$ jets

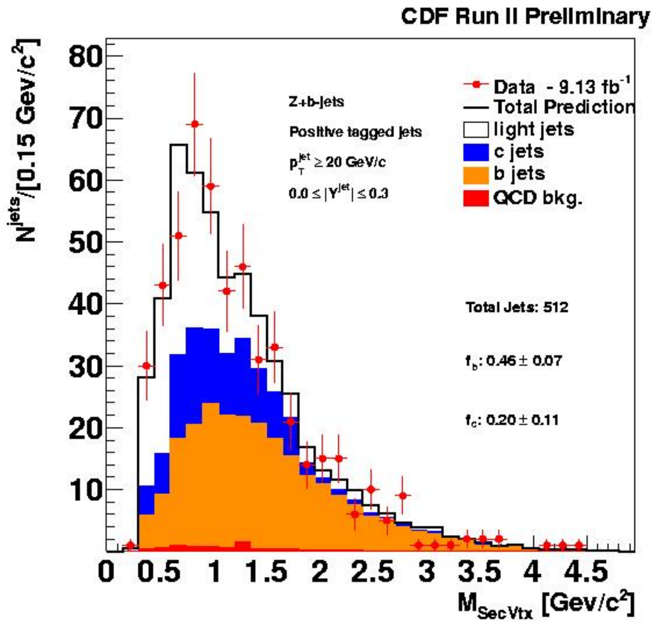

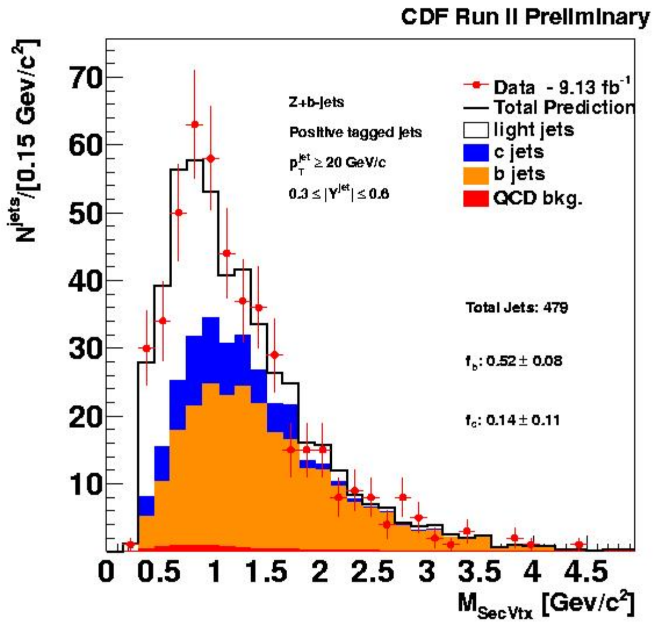

Figure 7.4: Secondary vertex mass fit results for first and second jet rapidity bins.

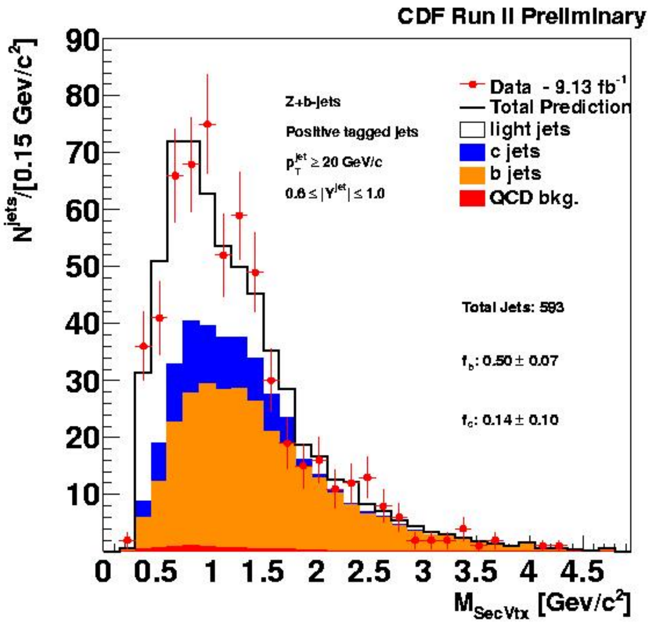

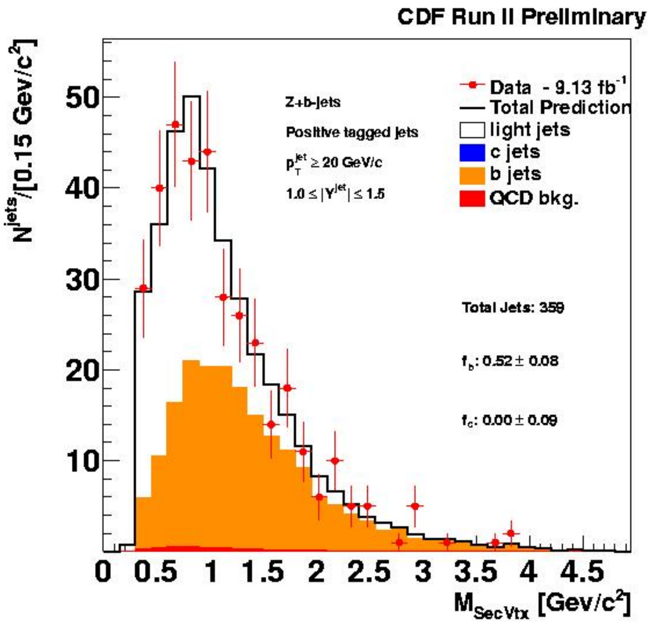

Figure 7.5: Secondary vertex mass fit results for third and fourth jet rapidity bins.

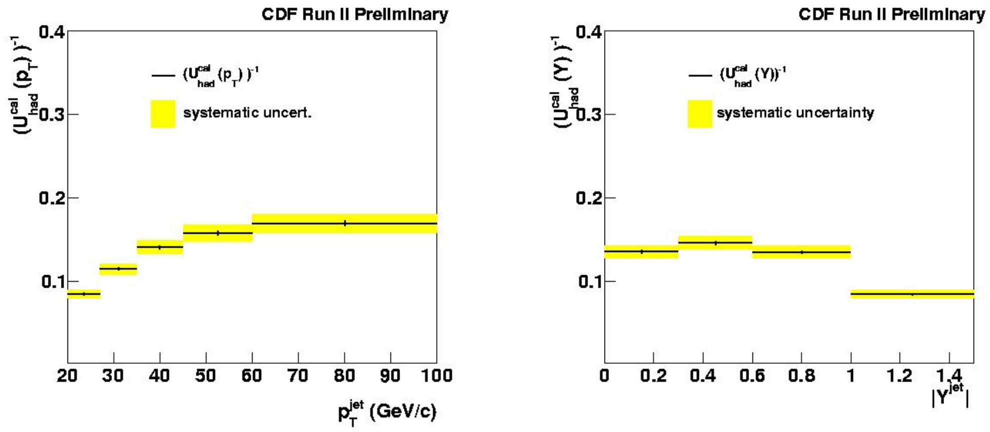

Figure 7.6: Inverse Unfolding factor as function of jet transverse momentum and jet rapidity.

is obtained by fitting it with the nominal templates. The uncertainty is estimated by the shift with respect to the mean obtained using pseudodata simulated with nominal templates. These measurements greatly benefit by the development of the ANNs to identify leptons, since the gain in statistics allows to perform a sensible fit per jet p_T and jet rapidity bin. Tables 7.3 and 7.4 summarized the systematic uncertainties while in Figure 7.7 the fitted b jets fraction with the total systematics for jet $\mathrm{p_T}$ and rapidity, is presented.

	1b/2b - 1c/2c syst (%)	trk ϵ syst (%)	lneg syst (%)	tot syst (%)
20 - 27 GeV/c	3.2	5.1	7.3	9.5
27 - 35 GeV/c	1.0	6.1	8.3	10.3
35 - 45 GeV/c	1.4	4.5	8.4	9.6
45 - 60 GeV/c	4.3	4.5	6.9	9.3
60 - 100 GeV/c	6.3	8.1	7.7	12.3

Table 7.3: Systematics uncertainties due to the templates shape mismodeling for each $\mathrm{p_T}$ bin

The systematics uncertainties due to jet energy scale and $b-$tagging uncertainty affect the unfolding factors. They are evaluated varying the uncertainty for each source of errors by $\pm 1\sigma$ and quoting half of the difference as systematic. Their contributions for each bin are summarized in Table 7.5.

	1b/2b - 1c/2c syst (%)	trk ϵ syst (%)	lneg syst (%)	tot syst (%)
0.0 - 0.3	4.0	5.0	12.3	13.9
0.3 - 0.6	3.0	6.3	8.6	11.1
0.6 - 1.0	4.3	9.3	6.7	12.2
0.0 - 1.5	3.5	6.3	11.9	13.9

Table 7.4: Systematic uncertainties due to the templates shape mismodeling for each jet rapidity bin.

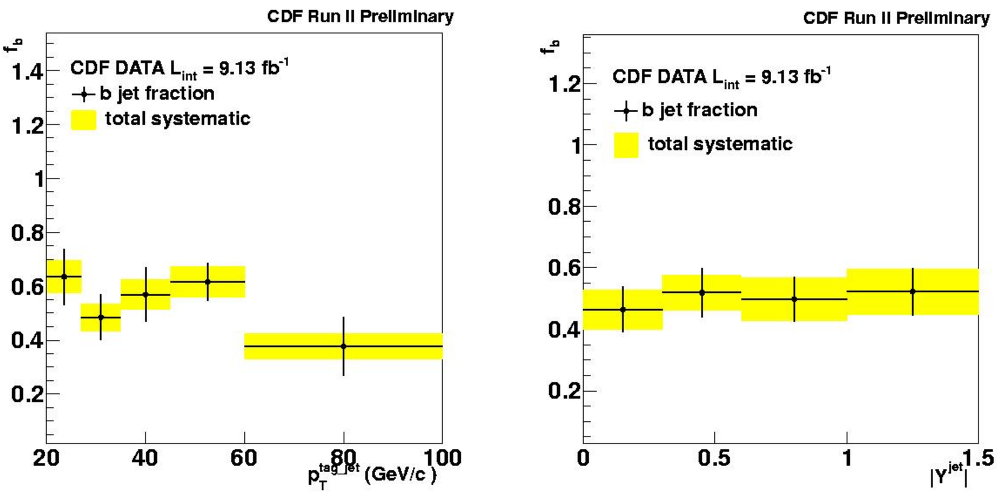

Figure 7.7: Secondary vertex mass fit results as function of jet transverse momentum and jet rapidity.

	abs syst. (%)	mi syst. (%)	eta syst. (%)	tag syst. (%)	tot syst. (%)
20 - 27 GeV/c	2.0	0.2	1.4	5.2	5.8
27 - 35 GeV/c	1.2	1.1	1.5	5.2	5.6
35 - 45 GeV/c	1.8	2.4	0.6	5.2	6.1
45 - 60 GeV/c	2.5	1.8	0.7	5.2	6.1
60 - 100 GeV/c	3.4	1.7	1.5	5.2	6.7
0.0 - 0.3	0.9	1.2	0.5	5.2	5.4
0.3 - 0.6	1.0	1.5	0.3	5.2	5.6
0.6 - 1.0	1.1	1.5	0.7	5.2	5.7
1.0 - 1.5	1.2	1.5	1.0	5.2	5.7

Table 7.5: Systematic uncertainties (%) for each component of the JES and $b-$tagging efficiency as function of jet p_T and jet rapidity.

8 Results

In this chapter differential cross sections and the ratio of the integrated $Z/\gamma^* + b-$jet cross section with respect to the inclusive Z/γ^* and Z/γ^*+jets cross sections are presented. The measurements are compared to next-to-leading order predictions corrected for non perturbative QCD effects and to leading-order ME+PS Monte Carlo.

8.1 Theoretical predictions

8.1.1 pQCD calculation

The NLO pQCD predictions are performed with the MCFM program according to the calculation explained in Chapter 3, i.e. using the prediction for Z and one $b-$jet in the 5FNS scheme. As seen the main contribution is coming from $gb \to Zb$. Other processes, that contribute at the same order in α_s, are those having Zbg and $Zb\bar{b}$ in the final states. $Zb\bar{b}$ can be evaluated by MCFM only at leading order and therefore is more sensitive to scale variations. b quark is treated as massless except for $Zb\bar{b}$ processes where the quark mass is required to rend the calculation finite.
The pQCD theoretical calculation is performed setting the PDF to MSTW2008 NLO and using several factorization and renormalization scales such as $\mu_0 = \mu_F = \mu_R = \sqrt{M_Z^2 + p_T^Z}$, $\mu_0 = \mu_F = \mu_R = \frac{1}{2}\hat{H}_T$[1] or $\mu_0 = \mu_F = \mu_R = \sqrt{\sum_i p_{T,i}^{2\,jet}/N_{jet}}$. Jets are reconstructed with the MidPoint algorithm with a cone size of $R = 0.7$ and $R_{sep} = 1.3$. The calculation is performed in the same phase space as for the measurement, i.e. Z/γ^* mass range of $[66, 116]$ GeV/c^2 with a central ($|Y^{jet}| \leq 1.5$) high-p_T ($p_T \geq 20$ GeV/c) jet.

8.1.2 Non pQCD corrections

Measurements are presented at hadron level to remove detector effects, thus to compare with theory, pQCD predictions have to be corrected for non perturbative effects such as underlying event (UE) and the fragmentation of the partons into hadrons (hadronization).

The underlying event is expected to add extra energy inside the cone of the jet due to the soft interaction between the $p\bar{p}$ remnants, while the fragmentation could cause that some particles originated from the same parton end up out of the jet cone.
The correction factors are obtained from MC and applied bin-by-bin for each distribution. Alpgen+Pythia samples with MSTW2008 NLO PDFs and Tune Perugia 2011 are used to derived the corrections as it has been shown to describe well observables sensitive to the UE

[1] $\hat{H}_T = \sum_i^n p_T^j + p_T^{l^+} + p_T^{l^-}$, j= partons

and hadronization such as jet shapes[36] and jet distributions in Z+jets data [75]. Corrections are estimated by comparing the hadron level cross section with UE on and the parton level cross section with UE off:

$$C_{HAD}(\alpha) = \frac{\frac{d\sigma^{UE}_{HAD}}{d\alpha}}{\frac{d\sigma^{noUE}_{parton}}{d\alpha}}, \qquad \alpha = p_T^{jet}, Y^{jet} \tag{8.1}$$

Figures 8.1 and 8.2 show the C_{HAD} factors as function of jet p_T and rapidity. Though they do not factorize, corrections due only to UE or to the hadronization are also presented for comparison. As expected, the underlying event correction is greater than one (extra energy added to jet cones), while the hadronization is less than one. The effects are greater at low jet p_T since the more energetic is a jet, the more collimated is and so less sensitive to soft radiation. The corrections are almost flat as function of jet rapidity.

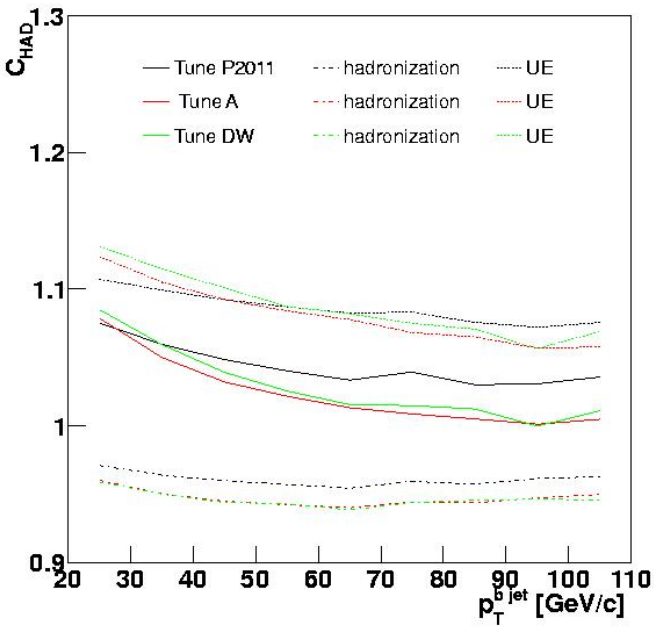

Figure 8.1: Non pQCD correction as function of jet p_T evaluated with Alpgen+Pythia MC samples. Contributions from underlying event and hadronization are also shown. Results using different Pythia tunes are presented.

8.1.3 Theoretical Uncertainties

Theoretical uncertainties include the renormalization and factorization scale variation and PDF errors.
The scale uncertainties are obtained by varying up and down the nominal renormalization

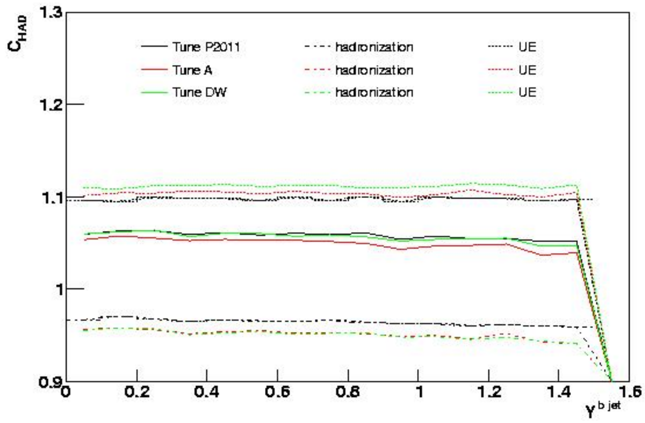

Figure 8.2: Non pQCD correction in function of jet rapidity evaluated with ALPGEN+PYTHIA. Here is possible to see the two contributions coming from underling events and from hadronization. Different tunes for PYTHIA are shown.

and factorization scale (μ_0) by a factor of 2, so evaluating the prediction at $\mu_0/2$ and at $2\mu_0$. This represents the main uncertainty, that is approximately 20 % due to the LO nature of the calculation of the $Zb\bar{b}$ term.
The PDF uncertainty is of the order of 2 % and it is evaluated using the Hessian method (Chapter 2), performing up and down variations along the 20 eigenvectors of MSTW2008. Asymmetric uncertainties are obtained by summing in quadrature the maximal deviations in each direction associate to each of the 20 eigenvectors. The dependence of the prediction on the PDF set (MSTW2008, CTEQ6.6, NNPDF) was studied and found to be negligible.
Other uncertainties could come from the modelling used for non pQCD corrections. Since UE is the main component, corrections were obtained using different Pythia Tunes such as Tune A and Tune DW. Differences are found to be small and between 2-3% (Figure 8.1).

8.2 Comparison with theoretical predictions

Results on the ratios of the $b-$jet cross section with respect to the inclusive Z/γ^* and Z/γ^*+jets cross sections are presented. These measurements are defined for events with a Z/γ^* boson (in the mass range $66 \leq M_{l^+l^-} \leq 116\ GeV/c^2$) and jets of $p_T \geq 20$ GeV/c and $|Y| \leq 1.5$.

8.2.1 Integrated $Z/\gamma^* + b-$jet production cross section

The ratio of the integrated $Z/\gamma^* + b-$jet cross section with respect to the Z/γ^* inclusive cross section is measured as:

$$\frac{\sigma_{Z/\gamma^*+b-jet}}{\sigma_{Z/\gamma^*}} = 0.263 \pm 0.023(stat) \pm 0.035(syst)\%$$

	NLO $Q^2 = m^2_{Z/\gamma^*} + p^2_{T,Z}$	NLO $Q^2 = \sqrt{\sum_i p^2_{T,i}{}^{jet}/N_{jet}}$
$\frac{\sigma(Z/\gamma^*+\mathrm{b})}{\sigma(Z)}$	2.3×10^{-3}	2.9×10^{-3}
$\frac{\sigma(Z/\gamma^*+\mathrm{b})}{\sigma(Z+\mathrm{jet})}$	1.8×10^{-2}	2.2×10^{-2}

Table 8.1: NLO MCFM theoretical predictions corrected for non pQCD effects.

and with respect to the Z+jets inclusive cross section :

$$\frac{\sigma_{Z/\gamma^*+b-jet}}{\sigma_{Z/\gamma^*+jet}} = 2.14 \pm 0.18(stat) \pm 0.32(syst)\%$$

Theory predictions calculated using MCFM and corrected by non perturbative effects are shown in Table 8.1.

Predictions are found in agreement with data. However there is a large dependence on the scale suggesting high-order terms are needed.

8.2.2 Muon and electron channels measurement

As a cross-check the measurements have been performed in each channel separately. The ratio of the integrated $Z/\gamma^* + b-$jet cross section with respect to the Z/γ^* inclusive cross section was found to be for the muon decay channel:

$$\frac{\sigma^{muon}_{Z/\gamma^*+b-jet}}{\sigma_{Z/\gamma^*}} = 0.308 \pm 0.036(stat)\%$$

while for the electron:

$$\frac{\sigma^{elec}_{Z/\gamma^*+b-jet}}{\sigma_{Z/\gamma^*}} = 0.2523 \pm 0.036(stat)\%$$

The ratio with respect to the Z+jets inclusive cross section for the muons is:

$$\frac{\sigma^{muon}_{Z/\gamma^*+b-jet}}{\sigma_{Z/\gamma^*+jet}} = 2.55 \pm 0.30(stat)\%$$

while for the electron decay channel:

$$\frac{\sigma^{elec}_{Z/\gamma^*+b-jet}}{\sigma_{Z/\gamma^*+jet}} = 2.02 \pm 0.29(stat)\%$$

The measurements are found in agreement within the statistical uncertainties.

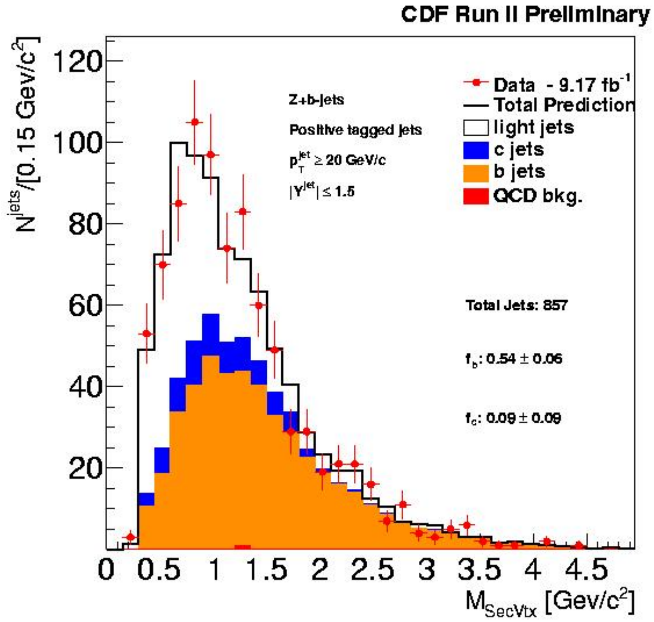

Figure 8.3: Fit for muon channel only.

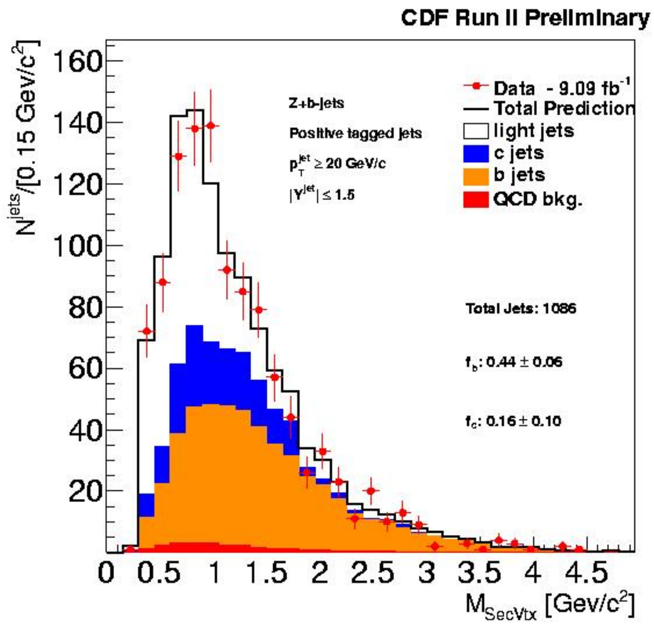

Figure 8.4: Fit for electron channel only.

8.2.3 Differential cross section

Differential cross section as function of jet p_T and rapidity are normalized to the measured Z/γ^* inclusive cross section and shown in Figures 8.5 and 8.6 where data are compared with NLO pQCD corrected by non perturbative effects. Theory predictions are obtained for different renormalization and factorization scales. A general good agreement is obtained between data and theory. Experimental uncertainties are comparable to those of the theory.

8.3 Comparison with LO ME+PS predictions

We have also performed the calculation with Alpgen v2.10+Pythia 6.325 tune BW with CTEQQ5L PDF at $\mu_F = \mu_R = \sqrt{M_Z^2 + p_{T,Z}^2}$. This comparison is relevant given how widely this program is used for generation of physics events at the Tevatron and LHC. In order to evaluate the MC prediction at hadron level, $b-$jets are defined as jets that match within $\Delta R \leq 0.4$ an outgoing b hadron. The $b-$jet cross section is therefore defined as:

$$\sigma_{Z/\gamma^*+b-jet}^{Alpgen+Pythia} = \frac{\sigma_{event}}{N^{gen}} \cdot N^{bhad}$$

where:

- σ_{event} is the generator cross section times leptonic Z/γ^* branching ratio in Alpgen for a given sample
- N^{gen} is the number of generated events that have passed $|z - vertex| < 60\ cm$ requirements
- N^{bhad} is the number of $b-$matched hadronic jets with $p_T \geq 20$ GeV/c and $|Y^{jet}| \leq 1.5$.

The prediction for each process in Alpgen+Pythia MC is reported in Table 8.2.

Summing over all processes we obtained the overall prediction that is:

$$\sigma = \sum_i^{process} \frac{\sigma_i \cdot N_i^{bhad}}{N_i^{gen}}$$

$$\sigma_{Z/\gamma^*_{\rightarrow\mu^+\mu}+b-jet} = 0.294\ pb \qquad \sigma_{Z/\gamma^*_{\rightarrow e^+e}+b-jet} = 0.295\ pb$$

As expected, the predictions from electron and muon channels are in agreement.
In the same way the Z/γ^*+jet cross section is calculated; thus is possible to estimate the

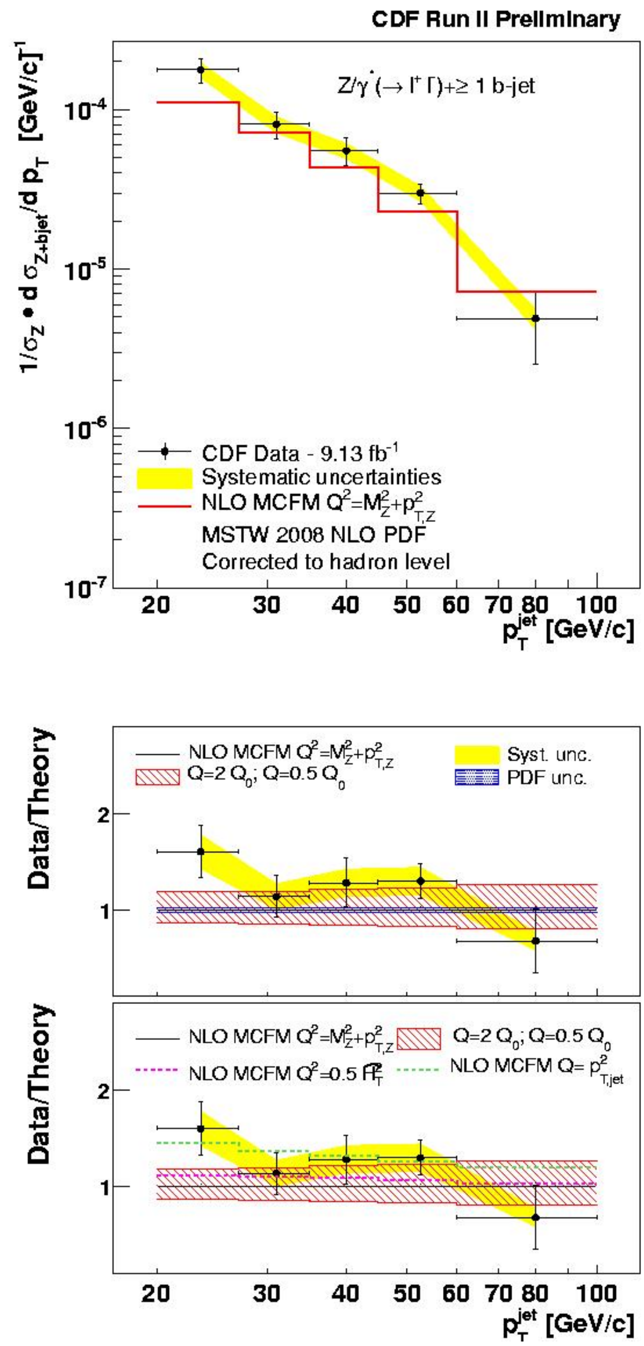

Figure 8.5: Differential cross section as function of jet p_T. The prediction is obtained with NLO MCFM at $Q^2 = M_Z^2 + p_{T,Z}^2$. The dependence on different PDF sets has been also studied but the effect is negligible compared with the uncertainties.

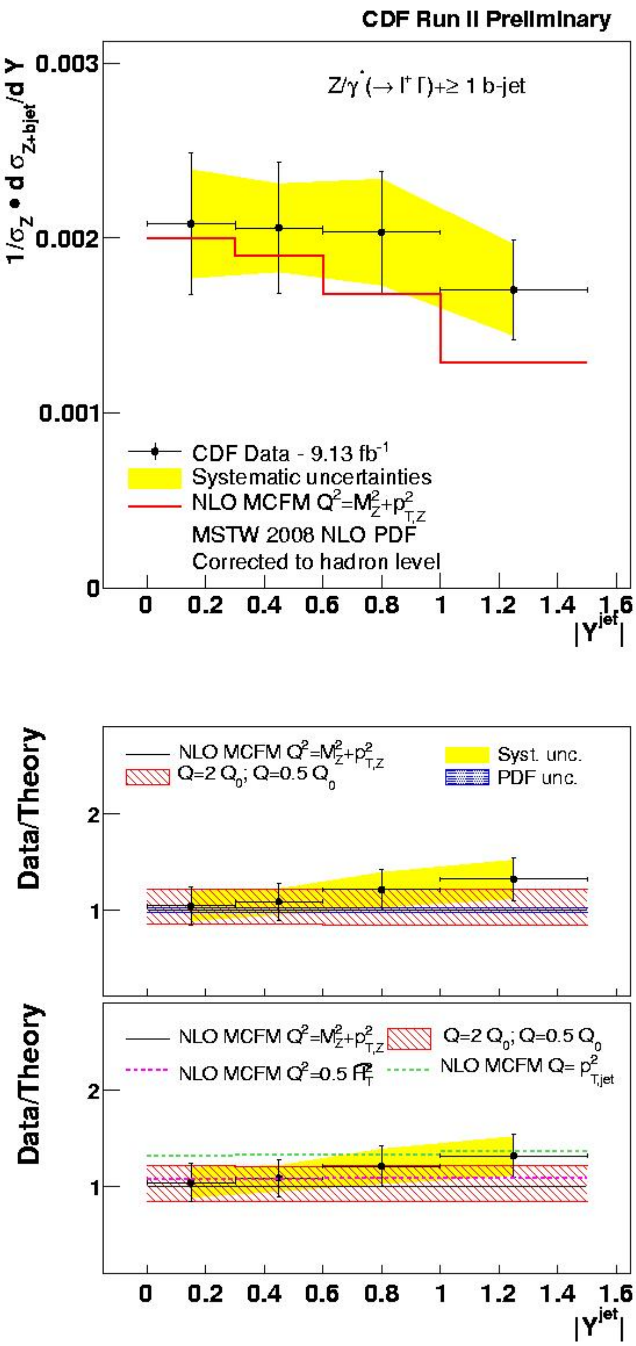

Figure 8.6: Differential cross section as function of jet rapidity. The prediction is calculated with NLO MCFM at $Q^2 = M_Z^2 + p_{T,Z}^2$. The dependence on different PDF sets has been also studied but the effect is negligible compared with the uncertainties.

Process	Predictions (pb)	
	$Z/\gamma^* \to e^+e$	$Z/\gamma^* \to \mu^+\mu$
z+bb+0p	0.1565	0.1566
z+bb+1p	0.0499	0.0500
z+bb+2p	0.0145	0.0145
z+0p	0.0043	0.0047
z+1p	0.0453	0.0437
z+2p	0.0158	0.0165
z+3p	0.0043	0.0044
z+4p	0.0014	0.0014
z+cc+0p	0.0001	0.0001
z+cc+1p	0.0016	0.0016
z+cc+2p	0.0015	0.0015

Table 8.2: Alpgen+Pythia prediction for $Z/\gamma^* \to \mu^+\mu^-$ and for $Z/\gamma^* \to e^+e^-$

prediction for $Z/\gamma^* + b$–jet cross section ratio respect to σ_{Z/γ^*+jet}:

$$R^{Alpgen+Pythia}_{electron} = \frac{\sigma(Z/\gamma^* + \mathrm{b})}{\sigma(Z + \mathrm{jet})} = 0.0143 \quad R^{Alpgen+Pythia}_{muon} = \frac{\sigma(Z/\gamma^* + \mathrm{b})}{\sigma(Z + \mathrm{jet})} = 0.0142$$

The measured value, as shown in previous section is

$$R = 0.0214 \pm 0.0018(stat) \pm 0.0032(syst)$$

This result is quite different to that from Alpgen+Pythia, larger by a factor of ~ 1.5 (and in agreement to the factor measured by CDF for the W+jets sample). This can be used as input for background estimation for analysis such as the search for the Higgs boson produced in association with a Z boson.

9 Conclusions

Processes involving bottom quarks have a key role in hadron colliders. Being among the heaviest quarks they are expected to interact strongly with the electroweak symmetry breaking sector in the Standard Model (SM) and in many models beyond the SM. For example, a light Higgs boson decaying into a pair of bottom and antibottom quarks constitutes one of the main channels for the search of associated production (WH/ZH) at the Tevatron. Recent results [2] have excluded at 95% of C.L. the high mass range for the SM Higgs. The low mass region is preferred and the ZH channel is one of the principal contributor in this case. Therefore the understanding of the $Z + b-$jet process is crucial. Accurate theoretical predictions are needed and the measurements described in this thesis provide a testing ground for Standard Model perturbative QCD predictions and the simulation tools developed for the description of this process.

In this thesis I present a new measurement of the production cross section for b jets in events with a Z/γ^* boson decaying into a pair of electrons or muons. The data corresponds to the complete dataset collected at CDF II from $p\bar{p}$ collisions at $\sqrt{s} = 1.96$ TeV. The per jet cross section measurement is done for a phase space characterized by a Z/γ^* within $66 \leq M_{ll} \leq 116\ GeV/c^2$ ($l = e, \mu$) and high-p_T central jets ($p_T \geq 20$ GeV/c $|Y| \leq 1.5$). Jets are reconstructed using the MidPoint algorithm in a cone size of R=0.7. The measurement is defined at hadron level and compared to a LO event generator matched to parton showers (ME+PS) and to NLO pQCD predictions computed with the MCFM program and corrected for non perturbative effects such as underlying event and hadronization. The comparison is performed for different values of renormalization and factorization scales and using several PDF sets.

The ratio of the integrated $Z/\gamma^* + b-$jet cross section with respect to the Z/γ^* inclusive cross section is measured to be:

$$\frac{\sigma_{Z/\gamma^*+b-jet}}{\sigma_{Z/\gamma^*}} = 0.263 \pm 0.023(stat) \pm 0.035(syst)\%$$

and with respect to the Z/γ^*+jets inclusive cross section :

$$\frac{\sigma_{Z/\gamma^*+b-jet}}{\sigma_{Z/\gamma^*+jet}} = 2.14 \pm 0.18(stat) \pm 0.32(syst)\%$$

The latter is found to be a factor 1.5 larger than the LO ME+PS prediction but it is in agreement with MCFM. In fact, MCFM predictions are consistent with differential and integrated cross section measurements, though large variations are seen for different scales. New theoretical developments with improved accuracy, merging NLO with parton showers, have been recently released which can be tested against the measurements presented in this thesis.

List of Figures

List of Tables

Bibliography

[1] P. Higgs, *Broken Symmatries, Massless Particles and Gauge Fieldes*, Phys. Lett. 12, (1964) 132;
F. Englert and R. Brout, *Broken Symmetry and the Mass of Gauge Vactor Mesons*, Phys. Rev. Lett. 13 (1964) 321;

[2] Atlas collaboration, *An update to the combined search for the Standard Model Higgs boson with the ATLAS detector at the LHC using up to 4.9 fb1 of pp collision data at s = 7 TeV*, ATLAS-CONF-2012-019, (20112);
CMS collaboration , *Combined results of searches for the standard model Higgs boson in pp collisions at* $\sqrt(s) = 7$ *TeV*, CMS-HIG-11-032, CERN-PH-EP-2012-023, (2011), arXiv:1202.1488 [hep-ex] ;

[3] M. Drees, R Godbole and P. Roy, *Theory and Phenomenology of Sparticles*, World Scientific, (2004);

[4] D. Acosta (CDF collaboration), *Measurement of the b jet cross section in events with a Z boson in* $p\bar{p}$ *collisions at* $\sqrt{s} = 1.96 TeV$, Phys.Rev.D79:052008, (2009);

[5] V. M. Abazov et al. (D0 coll.), *Measurement of the ratio of inclusive cross sections* $\sigma(p\bar{p} \to Z + b-quark\ jet)/\sigma(p\bar{p} \to Z+jet)$ *at* $\sqrt{s} = 1.96 TeV$ Phys Rev D 83, 031105, (2011)

[6] Atlas Collaboration, *Measurement of the cross-section for b-jets produced in association with a Z boson at* $\sqrt(s) = 7$ *TeV with the ATLAS detector* Phys Lett. B 706, 295-313, (2012), arXiv:1109.1403 [hep-ex];

[7] CMS collaboration, *Measurement of the* $Z/\gamma^* + bb-$*jets cross section in pp collisions at* $\sqrt(s)=$ *7 TeV with the CMS detector*, CMS-PAS-SMP-12-003, (2012);

[8] R.K. Ellis, W. J. Stirling and B.R. Webber, *QCD and Collider Physics* Cambridge Monographs on Particle Physics, Nuclear Physics and Cosmology, vol. 8, (1996);
G. Dissertori, I. G. Knowles and M. Schmelling, *High Energy Experiments and Theory*, Clarendon, Oxford, (2003);

[9] J. Smit, *Introduction to quantum field on a lattice, A robust mate*, Cambridege Lect. Notes Phys. 15 (2002) 1.;
Perspectives in Lattice QCD, Proceeding of the Workshop, Nara International Seminar House, Nara, Japan, 2005, Ed.Y. Kurumashi, World Scientific, Singapore, (2007);

[10] R. Brock et al. [CTEQ Collaboration], *Handbook of perturbative QCD*, Rev. Mod. Phys. 67 157, (1995);

x Field R D, *Application of Perturbative QCD*, Redwood City, Calif. Addison-Wesley, (1989);
Dokshitzer Yu L et al., *Basics of Perturbative QCD*, Ed J Tran Tranh Van, (1991);

[11] D.J. Gross and F. Wilizec, *Asymptotically Free Gauge Theories*, Phys. Rev. D 8, 3633 (1973);

[12] G. Salam, *Elements of QCD for hadron colliders*, CERN Yellow Report CERN-2010-002, pp. 45-100, (2011), arXiv:1011.5131 [hep-ph];

[13] Collins, Soper, Sterman, *Perturbative QCD*, ed A. H. Mueller, World Scientific Singapore, (1989);

[14] R. Devenish A. Cooper-Sarkar, *Deep Inelastic Scattering*, Oxford University Press, (2004);

[15] J.D. Bjorken, *Asymptotic Sum Rules at Infinite Momentum*, Phys Rev 179, 1547 (1969);
E. D. Bloom et al (SLAC-MIT Collaboration) , *High Energy Inelastic e-p Scattering at* 6° *and* 10°, Phys Rev Lett 23, 930 (1969);

[16] V. N. Gribov and L. N. Lipatov, e^+e^- *Pair Annihilation and Deep Inealastic ep Scattering in Perturbation Theory*, Sov J Nucl Phys 15, 438, 1972;
G. Altarelli and G. Parisi, *Asymptotic Freedom in Parton Language*, Nucl. Phys. B 126, 298 (1977);
Y. L. Dokshitzer, *Calculation of the Structure Functions for Deep Inealstic Scattering and* e^+e^- *Annihilation by Perturbation Theory in Quantum Chromodynamics*, Sov, Phys, JETP 46, 641 (1977);

[17] Pumplin et al, *A new generation of Parton distribution functions with uncertainties from global QCD analysis*, JHEP 0207:012, (2002), hep-ph/0201195v3;

[18] G. Watt, *MSTW PDFs and impact of PDFs on cross sections at TeVatron and LHC*, Nucl.Phys.Proc.Suppl. 222-224 61-80, (2012), arXiv:1201.1295 [hep-ph];

[19] NNPDF Coll., *A determination of parton distribution with faithful uncertainty estimation*, Nucl. Phys B, 809, 1-63 (2009), arXiv:0808.1231 [hep-ph];

[20] J. Pumplin et al, *Uncertainties of Predictions from Parton Distributions Functions II. The Hessian Method*, Phys. Rev D 65, 01413 (2001), hep-ph/0101032v3;

[21] Dokshitzer, Khoze, Troyan, *On the concept of Local Paton-Hadron Duality*, J Phys G Nucl. Part Phys 17 1585 (1991);

[22] B Andersson, *The Lund Model*, Cambridge Monogr. Part. Phys, Nucl, Phys. Cosmol., (1997);

[23] Winter, Krauss, Soff, *A modified cluster-hadronization model*, Eur. Phys JC36:391-395, (2004), hep-ph/0311085v1;

[24] J.E. Hutcj et al, *Toward a Standardization of Jet Definitions*, in Snowmass Summer study, p 134, World Scientific (1992), FERMILAB-CONF-90-249-E;

[25] Blazey,Dittman,Ellis et alt. *Run II Jet Physics*,(2010) hep-ex/0005012v2);
J. Huston and M. Toennesmann, *On Building Better Cone Jet Algotrithms*, eConf C010630 P513 (2001),hep-ph/0111434;

[26] Gavin P Salam, *Towards Jetography*, (2010) arXiv:0906.1833v2 [hep-ph];

[27] M.L. Mangano, M. Moretti, F. Piccinini, R. Pittau, A.D. Polosa, *ALPGEN, a generator for hard multiparton processes in hadronic collisions*, *J. High Energy Phys.* **0307** (2003) 001, hep-ph/0206293.

[28] F. Caravaglios, M.L. Mangano, M. Moretti, R. Pittau, *A New approach to multijet calculations in hadron collisions*, *Nucl. Phys.* **B 539** (1999) 215, hep-ph/9807570.

[29] T Sjostrand et al, *High energy Physics event Generation with Pythia 6.1*, Comput. Phys Commun. 135, 238 (2001) hep-ph/0603175;

[30] J. Campbell, R. K. Ellis, F. Maltoni, S. Willenbrock, *Associated Production of a Z Boson and a Single Heavy-Quark Jet* Phys.Rev.D69:074021, (2004), hep-ph/0312024v2

[31] C. F. Berger, Z. Bern, L. J. Dixon, F. Febres Cordero, D. Forde, T. Gleisberg, H. Ita, D. A. Kosower, D. Maitre *Next-to-Leading Order QCD Predictions for W+3-Jet Distributions at Hadron Colliders*, *Phys. Rev.* **D 80**, 074036 (2009), arXiv:0907.1984 [hep-ph].
C. F. Berger, Z. Bern, L. J. Dixon, F. Febres Cordero, D. Forde, T. Gleisberg, H. Ita, D. A. Kosower, D. Maitre, *Next-to-Leading Order QCD Predictions for Z,γ^*+3-Jet Distributions at the Tevatron*, *Phys. Rev.* **D 82**, 074002 (2010), arXiv:1004.1659 [hep-ph].
H. Ita, Z. Bern, L. J. Dixon, F. Febres Cordero, D. A. Kosower, D. Maitre, *Precise Predictions for Z + 4 Jets at Hadron Colliders*, arXiv:1108.2229 [hep-ph].
Z. Bern, L. Dixon, D.C. Dunbar, D.A. Kosower, *One-Loop n-Point Gauge Theory Amplitudes, Unitarity and Collinear Limits*, *Nucl. Phys.* **B 425** (1994) 217, [hep-ph/9403226].

[32] T Sjostrand, *Monte Carlo Generators*, CERN-CLGAPP-2006-66, (2006), hep-ph/0611247v1;

[33] J.C. Collins, *The Sudokov Form factors*, Ad.Ser Direct High Energy Physics, I:537-614, (1989);

[34] T. Sjöstrand, P. Skands, *Transverse-Momentum-Ordered Showers and Interleaved Multiple Interactions*, *Eur. Phys. J.* **C 39** (2005) 129, hep-ph/0408302.

[35] Rick Field, R. Craig Group, *Pythia Tune A, Herwig, and Jimmy in Run 2 at CDF*, hep-ph/0510198.

[36] P. Z. Skands, *Tuning Monte Carlo Generators: The Perugia Tunes*, *Phys. Rev.* **D 82**, 074018 (2010), arXiv:1005.3457 [hep-ph].
B.Cooper, J.Katzy, M.L.Mangano, A.Messina, L.Mijovic, P.Skands, *Monte Carlo tuning in the presence of Matching*, CERN-PH-TH/2011-228, DESY 11-124, arXiv:1109.5295 [hep-ph].

[37] R. Field, *CDF Run 2 Monte-Carlo Tunes*, FERMILAB-PUB-06-408-E.

[38] J. Alwall et al., *Comparative study of various algorithms for the merging of parton showers and matrix elements in hadronic collisions*, *Eur. Phys. J.* **C 53** (2008) 473, arXiv:0706.2569 [hep-ph].

[39] S. Frixione and B.R. Webber, *Matching NLO QCD computations and parton shower simulations*, JHEP 0206 (2002) 029 hep-ph/0204244

[40] S. Frixione, P. Nason and C. Oleari, *Matching NLO QCD computations with Parton Shower simulations: the POWHEG method*, *J. High Energy Phys.* **0711** (2007) 070, arXiv:0709.2092 [hep-ph].
S. Alioli, P. Nason, C. Oleari and E. Re, *Vector boson plus one jet production in POWHEG*, *J. High Energy Phys.* **1101** (011) 095, arXiv:1009.5594 [hep-ph].

[41] Aivazis, Collins, Olness, Tung, *Leptoproduction of heavy quarks. II. A unified QCD formulation of charged and neutral current processes from fixed-target to collider energies* Phys. rev. D 50, 3102 (1994);
J. Collins, *Hard-scattering factorization with heavy quarks: A general treatment*, Phys. Rev. D 58 094002 (1998)

[42] J. Campbell, Ellis, Maltoni, Willenbrock, *Associated Production of a Z Boson and a Single Heavy-Quark Jet*, FERMILAB-Pub-03/378-T (2003), hep-ph/0312024v2;

[43] J. Campbell, Ellis, Maltoni, Willenbrock, *Production of a Z boson and two Jets with One Heavy-Quark Tag*, Phys.Rev.D73:054007,(2006),hep-ph/0510362;

[44] J. Campbell and Ellis, *Radiative corrections to* $Zb\bar{b}$ *production*, Phys.Rev.D62:114012, (2000), hep-ph/0006304;

[45] Cordero, Reina, Wackeroth, *NLO QCD corrections to* $Zb\bar{b}$ *production with massive bottom quarks at the Fermilab TeVatron*, Phys.Rev.D78:074014, (2008), arXiv:0806.0808v2 [hep-ph];
Cordero, Reina, Wackeroth, *Associated production of a W or a Z boson with bottom quarks at the TeVatron and the LHC*, PoS(RADCOR2009)055, (2010), arXiv:001.3362v1 [hep-ph];

[46] Frederix, Frixione, Hirschi, Maltoni, Pittau, Torrielli, *W ans* Z/γ^* *boson production in association with a bottom-antibottom pair*, JHEP 1109:061, (2011), arXiv:1106.6019v2 [hep-ph];

[47] D.P. McGinnis, *Fermilab Tevatron operational status.* In C. Horak, editor, proceedingd pf the Particle Accelerator conference (PAC 05), 2005. In addition, detailed and updated information on the Tevatron is available in the following websites: http://www-bd.fnal.gov/runII/index.html, http://www-bdnew.fnal.gov/operations/rookiebooks/rbooks.html;

[48] D. Mohl et al., *Physics and Techniques of Stochastic Cooling*, Phys. Rept., 58, (1980);

[49] S. Nagaitsev et al., *Experimental Demonstration of Relativistic Electron Cooling*, Phys. Rev. Lett., 96, (2006);

[50] R. Blair and others (CDF II Collaboration), *The CDF II Detector*, Technical Design Report, FERMILAB-Pub-96390-E CDF, (1996);

[51] T. K. Nelson (for the CDF II Collaboration), *The CDF Layer 00 Detector*, FERMILAB-CONF-01/357-E; (2001), CDF Note 5780;

[52] C. S. Hill, *Initial experience with the CDF layer 00 silicon detector*, Nucl. Instr. Methods Phys. Revs. sect A, 511, 118-120, (2004);

[53] A. Sill, *CDF Run II silicon tracking projects.*, Nucl. Instrum. Methods, A447, (2000);

[54] A. Affolder et al., *Status report of the intermediate silicon layers detector at CDF II* , Nucl. Instrum, Methods, A485, (2002);
A. Affolder et al., Nucl. Instrum. Methods Phys, Rev Sect A, 461 (2001), 216-218;

[55] A. Affolder et al., *CDF Central Outer Tracker*, Nucl. Instrum, Methods, A526, (2004);

[56] S. Menzemer, *TrackingCal - A tracking and alignment software package of the CDF II silicon detector* Master thesis, University of Karlsruhe, (2002), CDF Internal Note 5968, unpublished;

[57] C. S. Hill et all, *Operational experience and performance of the CDF II silicon detector*, Nucl. Instrum. Methods, A530, (2004);

[58] D. Acosta et al. (CDF collaboration), *A time of flight detector in CDF II*, Nucl. Instrum. Methods, A518, (2004);

[59] L. Balka et al., *The CDF central electromagnetic calorimeter*, Nucl. Instr. Methods, A267, (1988);

[60] R.S.Hahn et al., *Calibration systen for the CDF central electromagnetic calorimeter*, Nucl. Instrum. Methods, A267, (1988);

[61] M. Gallinaro, *A new Scintillator Tile/Fiber Preshower Detector for the CDF Central Calorimeter*, IEEE Trans. Nucl. Sci., 52, (2005);

[62] S. Bertolucci et al., *The CDF central and endwall hadron calorimeter*, Nucl. Instrum. Methods, A267,(1988);

[63] M. Albrow et al., *The CDF plug upgrade electromagnetic calorimeter: test beam results.*, Nucl. Instrum. Methods, A480, (2002);
M. Albrow et al., *A preshower detector for the CDF Plug Upgrade: test beam results*, Nucl. Instrum. Methods, A412, (1998);
G. Apollinari et al, *Shower Maximum detector for the CDF plug upgrade calorimeter*,Nucl. Instrum. Methods, A412, (1998);

[64] G. Ascoli et al., *CDF central muon detector*, Nucl Instrum. Methods, A268, (1988);
C. M. Ginsburg et al., *CDF un 2 Muon System*,Eur. Phys. J., 33 (S1002), (2004);

[65] F. Abe et al. *Measurement of the antiproton-proton total cross section at* $\sqrt{s} = 546$ *and 1800 GeV*, *Phys. Rev.* **D 50**, 5550 (1993).
S. Klimenko, J. Konigsberg and T. Liss, *Averaging of the Inelastic Cross Sections Measured by the CDF and the E811 Experiments*, FERMILAB-FN-0741 (2003).
D. Acosta et al. (CDF collaboration), *The performance of the CDF luminosity monitor*, Nucl. Instrum. Methods, A494, (2002);

[66] E. J. Thomson et al, *Online Track Processor for the CDF Upgrade*, IEEE Trans Nucl. Sci, 49, (2002);

[67] B. Ashmanskas et al., *The CDF Silicon Vertex Trigger*, Nucl. Instrum. Methods, A518, (2004);
M. Dell'Orso , *The CDF Silicon Vertex Trigger*, Nucl. Phys. (Proc. Suppl), B156, (2006);
S. Belforte et al, *Silicon Vertex Tracker*, Technical Design Report, Public CDF Note 3108 (1995), CDF Note 3108;
J. Adelman et al., *The Silicon Vertex Trigger upgrade at CDF*, Nucl. Instr. Methods, Phys Res Sect A 572,361-364, (2007) ;

[68] G. Gomez-Caballlos et al., *Event Builder and Level 3 at the CDF experiment*, Nucl. Instrum. Methods, A518, (2004);

[69] G.C. Blazey et al., *Run II Jet Physics: Proceedings of the Run II QCD and Weak Boson Physics Workshop*, [hep-ex/0005012].
S.D. Ellis, J. Huston, M. Toennesmann, *On Building Better Cone Jet Algorithms*, eConf C010630 (2001) P513, [hep-ph/0111434].

[70] Bhatti et al, *Determination of the Jet Energy Scale at the collider Detector at Fermilab*, Nucl.Instrum.Meth.A566:375-412, (2006), hep-ex/0510047v1;

[71] CDF collaboration, *Measurement of the Cross Section for* $t\bar{t}$ *Production in* $p\bar{p}$ *Collisions using the Kinematics of Lepton+Jets Events*, Phys. Rev. D 71, 052003, (2005), hep-ex/0504053v2;

[72] CDF II b tag webpage;

[73] R. Brun, et al., *GEANT: Simulation program for particle physics experiments. User guide and reference manual*, CERN-DD-78-2-REV (1978);
GEANT: Detector description and simulation tool, Cern Program Library Long Writeup W5013, (1993);

[74] H.L. Lai et al, *Global QCD Analysis of Parton Structure of the Nucleon: CTEQ5 Parton Distributions*, *Eur. Phys. J.* **C 12** (2000) 375, [hep-ph/9903282];

[75] Stefano Camarda, Monica D'Onofrio, Sebastian Grinstein, Mario Martinez, Lorenzo Ortolan, Veronica Sorin *Measurement of* $Z/\gamma^* \to e^+e^-$*+jets Production Cross Section with 6* fb^{-1} CDF Note 101342;
Stefano Camarda, Monica D'Onofrio, Sebastian Grinstein, Mario Martinez, Lorenzo Ortolan, Veronica Sorin *Measurement of* $Z/\gamma^* \to \mu^+\mu^-$*+jets Production Cross Section with 6* fb^{-1} CDF Note 10155;

CDF Collaboration, *W/Z+Jets and W/Z+HF Production at the Tevatron* CDF Public Note 10536, (2010) ,CDF Note 10536;